TECHNISCHE UNIVERSITÄT WIEN

IKP

Diploma thesis

Combined propeller blade geometrical modifications to reduce noise emissions of urban air mobility vehicles

carried out for the purpose of obtaining the degree of Diplom-Ingenieur (Dipl.-Ing.),
submitted at TU Wien, Faculty of Mechanical and Industrial Engineering, by

Dominik Skrna

Mat. Nr.: 11771228

Advisors:

Univ.Prof. Dipl.-Ing. Dr.-Ing. Martin Berens MSc

Univ.Ass. Dipl.-Ing. Marcos Vitor De Rosa Jacinto da Silva

Research Group for Aircraft Systems

Institute of Engineering Design and Product Development

Lehargasse 6, 1060 Vienna, Austria

Vienna, 12.09.2023

Signature

Abstract

Urban air mobility (UAM) is a long-term concept of the transportation development in cities including electrical vertical take-off and landing (eVTOL) vehicles for the transport of people and goods. The first concepts are expected to go into operation already within this decade. One aspect of major relevance in this respect is the noise generation, as the social acceptance of these aerial vehicles in densely populated areas strongly depends on it. The propulsion system of such aircraft, in most cases propellers, are the main source of noise emissions. The objective of this diploma thesis is accordingly to study the reduction of noise generation in all phases of vertical flight by geometrical modifications of the propeller blades. In this regard numerous concepts have been developed in recent years, but no tailored combination of noise reduction geometrical modifications of the propeller blades, which is the main focus of the present work. Aerodynamic and aeroacoustic simulations in the far field are carried out for the purpose of validation and analysis of the effects of individual geometrical modifications using the CFD software OpenFOAM with an externally implemented aeroacoustics library. The combination of trailing edge serration, leading edge tubercles and tip modifications results in reductions of the broadband noise in comparison to the reference propeller geometry. While this is true for many configurations producing the same propeller thrust by means of RPM adjustments, it must be realized that the broadband noise magnitude still primarily depends on the rotational velocity. A reduction of the tonal noise can also be achieved due to the geometric adjustments that allow a reduction of the revolutions per minute while maintaining the generated thrust and mechanical power. Special attention has been paid to the combination of features regarding radial positioning and aerodynamic as well as aeroacoustic effect strength according to the results of a literature research. The simulation results are compared for different phases of vertical flight and at numerous rotational velocities within the framework of a parametric study. It emphasises the importance of considering numerous parameters in the optimisation process as well as the targeted design for specific operating conditions, as it is not possible to achieve an improvement for every service condition simultaneously. For the climb case, reductions in broadband noise of up to 8 dB in the narrow band random range as well as for frequencies above 5000 Hz can be observed by the combined application of geometric modifications in comparison to an unmodified propeller blade. The promising numerical results shall be experimentally verified in future research work.

Kurzfassung

Urban Air Mobility (UAM) ist ein langfristiges Konzept für die Verkehrsentwicklung in Städten, das elektrisch betriebene Senkrechtstarter und -landefahrzeuge (eVTOL) für die Beförderung von Personen und Gütern vorsieht. Es wird erwartet, dass die ersten Konzepte bereits in diesem Jahrzehnt in Betrieb genommen werden. Ein wichtiger Aspekt ist die Lärmentwicklung, denn davon hängt die soziale Akzeptanz dieser Luftfahrzeuge in dicht besiedelten Gebieten ab. Das Antriebssystem solcher Flugzeuge, in den meisten Fällen die Propeller, sind die Hauptquelle der Lärmemissionen. Ziel dieser Diplomarbeit ist es daher, die Reduzierung der Lärmentwicklung in allen Phasen des Vertikalfluges durch geometrische Veränderungen der Propellerblätter zu untersuchen. Hierzu wurden in den letzten Jahren zahlreiche Konzepte entwickelt, jedoch ohne eine abgestimmte Kombination, die im Mittelpunkt der vorliegenden Arbeit steht. Zur Validierung und Analyse der Auswirkungen einzelner geometrischer Modifikationen werden aerodynamische und aeroakustische Simulationen im Fernfeld unter Verwendung der CFD-Software OpenFOAM mit einer extern implementierten Aeroakustik-Bibliothek durchgeführt. Die Kombination von Hinterkantenverzahnung, Vorderkantentuberkel und Modifikationen an der Blattspitze führt zu einer Reduzierung des Breitbandgeräusches im Vergleich zur Referenzpropellergeometrie, wobei deren Ausmaß von der angewendeten Drehgeschwindigkeit abhängt. Eine Verringerung des tonalen Geräusches kann auch durch geometrische Anpassungen erreicht werden, die eine Verringerung der Drehzahl bei gleichzeitiger Beibehaltung des erzeugten Schubs und der mechanischen Leistung ermöglichen. Besonderes Augenmerk wurde dabei auf die Kombination von Merkmalen hinsichtlich der radialen Positionierung und der aerodynamischen sowie aeroakustischen Effektstärke gemäß den Ergebnissen einer Literaturrecherche gelegt. Die Optimierungsergebnisse werden im Rahmen einer Parameterstudie für verschiedene Phasen des Vertikalfluges und bei zahlreichen Rotationsgeschwindigkeiten verglichen. Dies zeigt, wie wichtig die Berücksichtigung zahlreicher Parameter im Optimierungsprozess sowie die gezielte Auslegung für bestimmte Betriebsbedingungen ist, da eine Verbesserung für jeden einzelnen Betriebszustand nicht möglich ist. Für den Steigflug kann durch die kombinierte Anwendung geometrischer Modifikationen im Vergleich zu einem nicht modifizierten Propellerblatt eine Verringerung des Breitbandlärms um bis zu 8 dB bei Frequenzen unterhalb von 1000 Hz sowie oberhalb von 5000 Hz festgestellt werden. Die vielversprechenden numerischen Ergebnisse sollen in zukünftigen Forschungsarbeiten experimentell verifiziert werden.

Statement of authorship

I declare in lieu of oath, that I wrote this thesis and performed the associated research myself, using only literature cited in this volume. If text passages from sources are used literally, they are marked as such.

I confirm that this work is original and has not been submitted elsewhere for any examination, nor is it currently under consideration for a thesis elsewhere.

I acknowledge that the submitted work will be checked electronically-technically using suitable and state-of-the-art means (plagiarism detection software). On the one hand, this ensures that the submitted work was prepared according to the high-quality standards within the applicable rules to ensure good scientific practice "Code of Conduct" at the TU Wien. On the other hand, a comparison with other student theses avoids violations of my personal copyright.

Wien am 12.09.2023 .....

City and Date

.....

Signature

Acknowledgements

Zuerst möchte ich mich bei dem Team der Forschungsgruppe Luftfahrzeugsysteme, bei dem ich nicht nur als studentischer Mitarbeiter angestellt bin, sondern auch als Student einige Lehrveranstaltungen besucht habe, herzlichst bedanken. Insbesondere bei meinen Betreuern Univ.Prof. Dr.-Ing. Martin Berens MSc und Univ.Ass. Marcos Vitor De Rosa Jacinto da Silva, die mir jederzeit hilfreich und mit passenden Tipps zur Seite gestanden sind. Eine derartig einwandfreie Zusammenarbeit ist nicht selbstverständlich, weshalb ich nicht nur sehr dankbar für die hervorragende Betreuung meiner Diplomarbeit bin, sondern auch für die zahlreichen Erfahrungen und Kompetenzen, die ich während meiner ca. 18-monatigen Zeit als studentischer Mitarbeiter gesammelt und erworben habe.

Außerdem möchte ich meinen Eltern Isabella und Richard herzlichst danken, die meine Brüder und mich über die Jahre mit viel Geduld und Einsatz unterstützt haben. Ihre Erfahrungen und Ermutigungen haben dazu beigetragen, die richtigen Entscheidungen zu treffen und unsere Ziele zu erreichen. Meiner Großmutter Maria Jakl, die die österreichische zivile Luftfahrt als erste Stewardess Österreichs bei Austrian Airlines mitgeprägt hat und durch zahlreiche Geschichten die Faszination fürs Fliegen bei meinen Brüdern und mir geweckt hat, möchte ich ebenfalls meinen herzlichen Dank aussprechen. Natürlich möchte ich auch meine Brüder Florentin und Sebastian erwähnen, wobei besonderer Dank letzterem gilt, da er ein Vorreiter im Maschinenbaustudium war und seine Tipps und Erfahrungen dazu beigetragen haben, dass ich mir viel Zeit erspart habe.

Besonderer Dank gilt auch Matthias, der mich von der ersten Klasse Volksschule durchgehend bis zum Ende des Studiums nicht nur als Klassen- bzw. Studienkollege, sondern vor allem als Freund begleitet hat („Never change a winning team!“).

Abschließend bedanke ich mich auch bei meiner Freundin Adriana, die mich fast mein ganzes Studium begleitet und durchgehend unterstützt hat. Ihr motivierender Beistand und ermutigender Zuspruch haben die anspruchsvollsten Phasen der universitären Ausbildung deutlich erleichtert.

Nomenclature

Λ	Blade sweep angle
Λ_{Tip}	Blade tip sweep angle
Γ_{Tip}	Blade tip anhedral angle
α	Serration angle
β	Pitch angle
δ_{ij}	Kronecker Delta
ε	Turbulence kinetic energy dissipation rate
η_{P}	Propeller propulsive efficiency
θ	Radiation angle (Observer angle)
λ	Wavelength
ν	Kinematic viscosity
ν_{t}	Turbulent viscosity
ρ	Density
ρ'	Density at the far field
τ	Retarded time
ϕ	Radiation angle
∇	Nabla operator
Δh	Mesh size
Δt	Time step
A	Tubercle amplitude
B	Number of blades
C	Courant number
D	Propeller diameter
J	Advance ratio
M	Mach number
P_{b}	Pitch value
Q	Generated torque
R	Radius
S	Source strength
S_0	Surface area
T	Generated thrust

U	Flow velocity
V	Inflow velocity
c	Chord length
c_0	Speed of sound
c_l	Lift coefficient
c_T	Thrust coefficient
$\bar{c}$	Local chord length
d	Distance between two sources
d_h	Horizontal distance
d_v	Vertical distance
f	Frequency
h	Serration amplitude
k	Turbulence kinetic energy
k_w	Wavenumber
l	Characteristic length
n	Propeller rotational velocity
p	Thermodynamic pressure
p_{acoustic}	Acoustic pressure
p_{ref}	Reference pressure
t	Time
u_*	Friction velocity
x	Distance from source
y^+	Dimensionless wall distance
$\boldsymbol{\sigma}$	Viscous stress tensor
$\boldsymbol{T}$	Lighthill stress tensor
$\boldsymbol{n}$	Unit normal vector
$\boldsymbol{p}$	Surface loading tensor
$\boldsymbol{v}$	Velocity vector

Abbreviations

BERP	British Experimental Rotor Programme
BPF	Blade Passing Frequency
BVI	Blade Vortex Interaction
CFD	Computational Fluid Dynamics
DES	Detached Eddy Simulation
EPNL	Effective Perceived Noise Level
eVTOL	Electric Vertical Take-Off and Landing
FAA	Federal Aviation Administration
FFT	Fast Fourier Transformation
FWH	Ffowcs Williams Hawkings
LAA	Lighthill's Acoustic Analogy
LE	Leading Edge
LES	Large Eddy Simulation
MCA	Mid-chord Alignment
NASA	National Aeronautics and Space Administration
OASPL	Overall Sound Pressure Level
PNL	Perceived Noise Level
RANS	Reynolds Averaged Navier-Stokes
RAS	Reynolds Averaged Simulation
RPM	Revolutions Per Minute
SI	International System of Units
SPL	Sound Pressure Level
TE	Trailing Edge
UAV	Unmanned Aerial Vehicles
UIUC	University of Illinois at Urbana-Champaign
VSC	Vienna Scientific Cluster

Table of contents

1. Introduction 1
   1.1 Motivation 1
   1.2 Current research projects 2
   1.3 Outline of thesis 3
2. Fundamental principles 5
   2.1 Fundamentals of technical acoustics 5
   2.2 Aeroacoustic analogies 9
      2.2.1 Lighthill´s governing equations 10
      2.2.2 Curle analogy 10
      2.2.3 Ffowcs-Williams-Hawkings analogy 11
   2.3 Sources of propeller noise 12
      2.3.1 Thickness noise 13
      2.3.2 Loading noise 14
      2.3.3 Broadband noise 14
      2.3.4 Quadrupole noise 14
   2.4 Turbulence modelling 15
3. Propeller design parameters and geometrical modifications 16
   3.1 Fundamental parameters 16
      3.1.1 Pitch angle 17
      3.1.2 Thickness ratio 18
      3.1.3 Blade sweep 19
      3.1.4 Chord length 20
   3.2 Additional geometrical modifications 21
      3.2.1 Trailing edge serration 21
      3.2.2 Propeller tip modifications 22
      3.2.3 Leading edge tubercles 24
4. Computational Fluid Dynamics using OpenFOAM 25
   4.1 Basic structure of OpenFOAM 25
      4.1.1 “0” directory 26
      4.1.2 “constant” directory 26
      4.1.3 “system” directory 27
   4.2 Implementation of acoustic library - libAcoustics 29
   4.3 Simulation process 30
5. Propeller geometry modelling and meshing process 31
   5.1 Input conversion in Phyton 31

5.2 Geometry creation in CATIA 32
5.3 Meshing in OpenFOAM 32
6. Validation of the OpenFOAM model 36
6.1 Validation case 1 37
6.1.1 Geometry and simulation input data 37
6.1.2 Aerodynamic validation 38
6.1.3 Aeroacoustic validation 39
6.2 Validation case 2 41
6.2.1 Geometry and simulation input data 41
6.2.2 Aerodynamic validation 43
6.2.3 Aeroacoustic validation 43
6.3 Validation case 3 46
6.3.1 Geometry and simulation input data 46
6.3.2 Aerodynamic validation 47
6.3.3 Aeroacoustic validation 48
7. Advanced simulations of the climb phase 49
7.1 Reference propeller APC 27x13E 49
7.1.1 Model geometry and performance data 49
7.1.2 Mesh quality study 53
7.1.3 Aerodynamic results 55
7.1.4 Aeroacoustic results 58
7.2 Individual geometrical modifications 60
7.2.1 Case 1: Leading edge tubercles 61
7.2.2 Case 2: Trailing edge serration 64
7.2.3 Case 3: Tip modifications 68
7.3 Combination of geometrical modifications 72
8. Advanced simulations of hovering and descent phases 77
8.1 Hovering flight 77
8.2 Descent flight 80
9. Parameter study 84
9.1 Aerodynamic results 84
9.2 Aeroacoustic results 86
10. Conclusion and outlook 90
11. References 92
12. List of figures 97
13. List of tables 104
Appendix A 105

1. Introduction

Individual urban mobility in terms of transportation of people and goods in densely populated areas is currently bound to the ground level. The utilization of several levels at various altitudes in the airspace volume with air vehicles would significantly improve the traffic situation on the existing infrastructure. Nowadays, it is only possible to use helicopters, to a limited extent, in urban areas to be able to move at heights other than ground level. In the future, this is supposed to be more accessible by the introduction of electrical vertical take-off and landing (eVTOL) air vehicles. However, the safety aspects of operating these aircraft must be accepted by the public just as much as the noise level they produce. This requires overcoming major preconceptions, namely the fact that most aircraft, whether civilian airliners or helicopters, are clearly audible when flying overhead. This diploma thesis therefore investigates the possibilities of noise reduction of propellers used for urban air mobility vehicles. Special focus is placed on the combination of geometrical modifications of propeller blades. The computational aero-acoustic simulations focus on the vertical operational phases, namely climb and hovering as well as descent, of such aircraft.

The area of application of the investigated propeller modifications is only the civil aviation sector for the transportation of people and cargo primarily in urban areas. Military applications are explicitly excluded and a misappropriation with the intention of causing damage or bodily harm is by no means supported.

1.1 Motivation

Already some years after the first motor powered flight with propellers by the Wright brothers in 1903, the first experiments were conducted to reduce the noise produced by propellers of aircraft in 1919. The reason for this emerged in the first World War, as unnoticed overflight of enemy territory with propeller-driven aircraft was not possible. Although there is a difference between the propellers used for motor powered aircraft in the 1920s and the ones used for civil drones in the scope of this diploma thesis, the subject of reducing the resulting noise is still relevant over 100 years later [1]. Noise reduction is not only necessary for the human well-being, in general nature and the environment must be protected from excessive noise pollution. Therefore, regulations and guidelines have been created to limit these emissions. In addition, developments in this field of application can not only have a major influence on other areas of research in aeronautics, but also in other sectors such as marine propulsion technology or energy generation by wind power plants. As with many other discoveries in aviation, nature serves as the main source of inspiration, which is why it is particularly important that the improved technology also benefits the environment.

1.2 Current research projects

There are several ongoing research projects with the goal to reduce the noise produced by propellers of eVTOL air vehicles; unmanned aerial vehicles (UAV) and autonomously piloted aircraft with the purpose of transporting passengers and cargo. In the course of this thesis, several reports, papers and theses are presented, which focused mainly on isolated propellers. Therefore, a perspective on the overall output with interesting and promising results from recent reports is presented in the introduction.

The company behind the eVTOL seen in the upper section of figure 1.1 is Joby Aviation, a California based aviation corporation that started a collaboration with NASA in 2012. The completely electrically powered aircraft can change between hover and cruise configuration by tilting the rotational axes of the six propellers. In contrast to conventional helicopters, Joby Aviation`s eVTOL is meant to offer commercial air taxi operations with zero emissions and significantly reduced noise during all phases of flight [2]. A recent experimental study conducted by NASA to investigate the aeroacoustic properties of this aircraft confirmed the promising computational output for all phases of flight [3].

Figure 1.1: Joby Aviation S4 prototype [3] (top) and visualisation of the City Airbus NextGen concept [4] (bottom)

Airbus also currently runs a research programme in which a UAM vehicle is developed. The City Airbus NextGen, which is a similar concept to the one of Joby, uses eight smaller propellers, which can be seen in the bottom section of figure 1.1. Unlike its Californian competitor, the propellers are fixed and cannot be adjusted for cruise flight. Instead, two propellers are mounted on the tail plane whose rotational axes are not perpendicular to the ground. As no official test flight has taken place yet, the acoustic data have not yet been verified, but they are also expected to be low [4].

In contrast to the two concepts mentioned above, there are other designs with smaller propellers from several companies, of which two representative visualisations are shown in figure 1.2. In terms of the scale of the propeller, these fit better with the ones studied in this thesis. Their fields of application are also flexible. On the one side, there is the cargo drone of the company Phoenix Wings. The Munich based manufacturer develops simple and safe air vehicles for the transport of goods without a human pilot. The PW ORCA model (see figure 1.2 on the left side) has six vertically oriented propeller axes and two horizontal ones, which provide enough thrust to transport payloads of up to 15 kg in a 96-liter cargo space [5].

Figure 1.2: Phoenix wings ORCA cargo drone (left) [5] and Jetson One eVTOL (right) [6]

On the other side, the one person eVTOL by Jetson with four pairs of counter-rotating propellers, is about the size of a small car. Due to the achievable top speed of 102 km/h and the sleek appearance, which can be seen in figure 1.2 on the right side, it is praised as a racing car of the sky for good reason. The only limitation is the restricted flight time due to the size of the battery. Because of its low weight and relatively low speed compared to other aircraft, no pilot licence is required by the Federal Aviation Administration (FAA) in the United States. The maximum payload of 95 kg is mainly claimed by the mass of the pilot. The first models are already in delivery starting in 2023 [6].

1.3 Outline of thesis

There are several studies in literature about the influence of individual geometric modifications of the propeller blade on aerodynamic as well as aeroacoustic properties. Most of them are applied to smaller propellers with diameters of 0,3 m or less. The objective of this thesis therefore on the one hand is to implement larger propellers, that are able to propel UAM vehicles, into computational fluid dynamics (CFD) simulations. The effects of geometrical modifications of the propeller blade are also to be demonstrated for this order of magnitude. On the other hand, the optimisation of the combination of numerous geometrical features has to be investigated. The focus is placed on maintaining aerodynamic and performance properties, in particular the constant thrust while reducing the noise output.

Accordingly, the fundamentals of technical acoustics, the aeroacoustic analogies and the sources of propeller noise need to be introduced first, which is done in chapter 2. This is followed by a literature review of the influence of design parameters and geometrical modifications of the propeller blade on the aerodynamics and aeroacoustics of propellers. Some of the concepts are later applied in the validation and in the advanced simulations. The fundamentals of the computational fluid dynamics software OpenFOAM are explained in chapter 4. The implemented acoustic library is also described in more detail in this chapter.

After the theoretical section, the practical part starts in chapter 5 with the description of the geometry generation in CATIA and the subsequent meshing process in OpenFOAM. The validation of the OpenFOAM models is carried out in chapter 6. For this purpose, different propeller geometries and modifications are tested for various simulation parameters and then are compared with data from literature. The main subject of this thesis, the combination of the individual geometric modifications and the measurement of individual adjustments for larger diameters, is described in chapter 7. Since the simulation setup was initially designed for the climb case only, the results for the hovering and descent case are discussed in chapter 8. This thesis is complemented by a parameter study for different rotational velocities in chapter 9 and a conclusion in chapter 10, which summarizes the most important results. Furthermore, recommendations for more in-depth studies are given as well as an outlook on future research work.

2. Fundamental principles

The noise that is induced by an aerodynamic flow passing a solid obstacle along a surface is associated with aeroacoustics [7]. This definition of noise creation and the principles on which it is based on are explained in more detail in this chapter, starting with relevant fundamentals of technical acoustics which are applied in this diploma thesis. Furthermore, the acoustic analogies on which the OpenFOAM simulation is based on as well as the common sources of noise are characterised. This allows an evaluation and analysis of the simulation output. In addition, the applied turbulence model is presented.

2.1 Fundamentals of technical acoustics

This chapter is intended to provide a brief overview of important aspects in technical acoustics that are necessary for understanding the computational simulation processes and results of this diploma thesis. For not explained terms and principles as well as for more detailed information, please refer to corresponding literature.

Near and far field

The near field is characterised as the area directly around the sound source in which interference effects are relevant to consider. The sound waves are circulating and propagating, leading to deviating, fluctuating and non-reproducible measurement results, especially when using only one microphone. At a distance of about one wavelength away from the sound source, a spherical propagation with a plane wave front can be assumed (see Fig. 2.1). This defines the far field, in which sound pressure and acoustic particle velocity are in phase. Acoustic measurements should ideally be carried out in the far field [8].

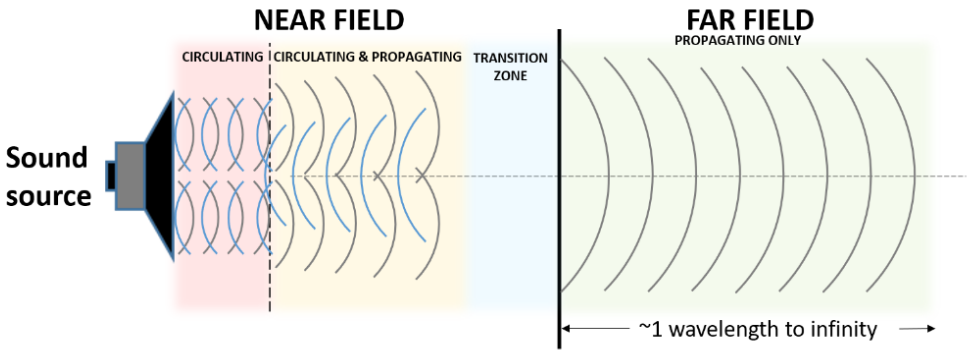

Figure 2.1: Definition of near and far field with corresponding wave propagation [8]

To determine if the acoustic observer is located in the far field, the criteria of equation 2.1 need to be considered. The distance R from the receiver position to the source, the characteristic size l of the source as well as the wavelength λ are put into relation for this purpose [9].

$$\frac{R}{\lambda} \gg 1 \qquad \frac{R}{l} \gg 1 \qquad \frac{R}{l} \gg \frac{l}{\lambda} \qquad \text{(Eq. 2.1)}$$

Sound pressure level and weighting

The conversion of the acoustic pressure p_{acoustic} to the sound pressure level (SPL) with the unit decibel (dB) can be conducted by using equation 2.2. The reference pressure value p_{ref} is set to $2 \cdot 10^{-5}$ MPa , which represent the threshold of human hearing [7].

$$SPL = 20 \cdot log\left(\frac{p_{\text{acoustic}}}{p_{\text{ref}}}\right) \qquad \text{(Eq. 2.2)}$$

The acoustic data obtained by measurement instruments are augmented according to a specific weighting for improved correlation with the sensitivity of the human ear. The weighted SPL better corresponds to perceived loudness. The most common correction scale is the A-weighting, which reduces the SPL values for low frequencies. As many experimental data are given in dB(A), the letter in parentheses corresponds to the weighting function, it is important to know how to adapt the results in order to validate computational simulations with practical experiments. Figure 2.2 shows the correction curves for several weightings [10].

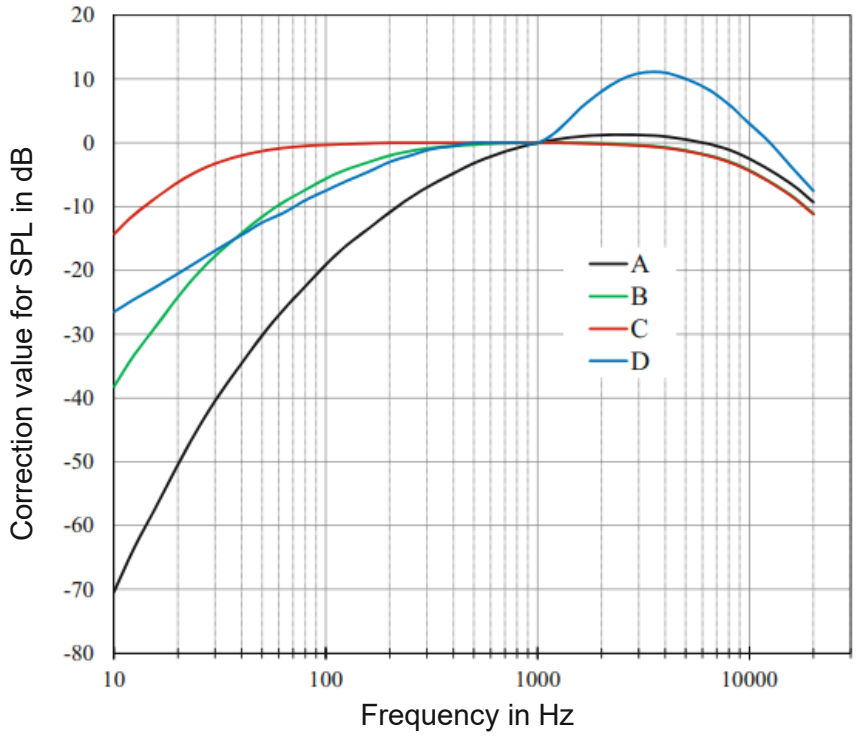

Figure 2.2: Correction of SPL values due to ratings (A, B, C and D) [10] (modified)

Further subjective units, which are used in aviation for the assessment of noise, are the perceived noise level (PNL) and the effective perceived noise level (EPNL), which are both essentially sound power levels [7]. The results of the simulations carried out for this diploma thesis are defined in the objective physical unit SPL.

Frequency bands

The human ability to hear extends over a frequency range from about 20 Hz to 20 kHz. The hearing organ does not split sounds into single frequencies, but groups them into frequency bands. The filtering of the frequency spectrum for the common logarithmic scaled octave and third-octave bands is realised with the help of band-pass filters. Frequencies within a certain band width are allowed to pass, the others are filtered out [10]. An overview of the band centre frequencies of octave filters and third octave filters in the audible frequency range according to the standard DIN 61260 [11] can be seen in table 1.

Table 1: Octave band and corresponding third octave band centre frequency values in the audible range [11]

Octave band frequency	Third-octave band frequencies	Octave band frequency	Third-octave band frequencies
16	12.5, 16, 20	1000	800, 1000, 1250
31,5	25, 31.5, 40	2000	1600, 2000, 2500
63	50, 63, 80	4000	3150, 4000, 5000
125	100, 125, 160	8000	6300, 8000, 10000
250	200, 250, 315	16000	12500, 16000, 20000
500	400, 500, 630		

In some literature the acoustic results are given at the third-octave frequency values. The calculation for this kind of data presentation is based on formula 2.3 [12] and formula 2.4, where $f_{\mathrm{m,i}}$ represents the respective third-octave band frequency. All SPL values of the frequencies f_{j} between the lower ($f_{\mathrm{l,i}}$) and upper limit ($f_{\mathrm{u,i}}$) must be included [9].

$$SPL_{\mathrm{i}} = 10 \cdot log\left(\sum_{f_{\mathrm{l,i}}}^{f_{\mathrm{u,i}}} 10^{\frac{SPL_{\mathrm{i,j}}(f_{\mathrm{j}})}{10}}\right) \qquad \text{(Eq. 2.3)}$$

$$f_{\mathrm{l,i}} = f_{\mathrm{m,i}} \cdot 2^{-1/6} \qquad f_{\mathrm{u,i}} = f_{\mathrm{m,i}} \cdot 2^{1/6} \qquad \text{(Eq. 2.4)}$$

Similar to the third octave band frequencies, there are also possibilities for an even more detailed breakdown. The 1/12 octave filter, which is also applied in this thesis, returns four times as many SPL outputs at predefined frequency values. This can be achieved by applying equation 2.3 and changing the exponent number from 1/6 to 1/24 in equation 2.4. Furthermore, a parameter for the comparison of acoustic simulations must be introduced, namely the overall sound pressure level (OASPL), which is given by equation 2.5 [12].

$$OASPL = 10 \cdot \log\left(\sum_{i}^{N} 10^{\frac{SPL_{\mathrm{i}}}{10}}\right) \qquad \text{(Eq. 2.5)}$$

Fast Fourier transformation (FFT)

The acoustic results obtained by the performed simulations are given by the parameters p_{acoustic} and time. The transformation of the acoustic pressure to the SPL has already been explained in equation 2.2, however, the conversion from the time domain to the frequency domain has not yet been stated (see Fig. 2.3). This is achieved by the fast Fourier transformation (FFT) algorithm. The two decisive parameters are the sampling frequency, which is defined as the reciprocal value of the selected time step, and the block length of a signal that represents the selected number of samples [13]. The frequency resolution, which indicates the increment size of the output, is the result of the division of those two parameters.

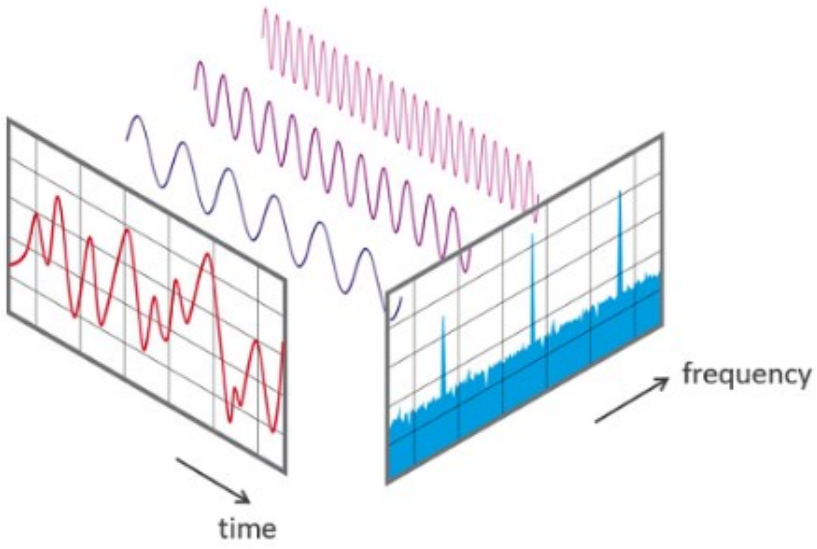

Figure 2.3: Schematic representation of the basic principle of the FFT [13]

In this context, the terms Nyquist theorem and aliasing also have to be mentioned. The first states that the sampling frequency must be at least twice as high as the highest frequency of the continuous signal, so that an exact representation of the discrete signal is possible. The effect of aliasing occurs if the frequency is higher than the highest maximum value of the continuous signal. As a result, errors known as artefacts can occur, which influence the output. This can be avoided by increasing the sampling rate or by using a special low-pass filter [13].

Sources of sound

The sources and the propagation of sound can be of different character. For monopole sources (see Fig. 2.4, left), a time-varying volume flow is responsible for sound generation. This is the basis for the other sources of sound, but it does not show any directional dependency so that it emits the sound equally in all directions. The size of a monopole source is usually smaller than the wavelength of the emitted sound. The radiated pressure amplitude can be defined as seen in equation 2.6 [14].

It depends on the distance x from the source to the observer, the radiation angle ϕ, which is zero in this case, and the time t. The other variables are the source strength S, the density ρ, the wavenumber k_w as well as the speed of sound c_0.

$$|p(x,\phi,t)| = \frac{S \cdot \rho \cdot c_0 \cdot k_w}{4 \cdot \pi \cdot x} \qquad \text{(Eq. 2.6)}$$

In the case of dipole sources (see Fig. 2.4, middle), there is no change of the volume flow but alternating forces are present. It consists of two symmetrically balanced monopole sources, which are oriented in opposite directions and show a specific directivity. The direction-dependent varying sound power is also visible in the pressure amplitude of equation 2.7, with d defined as the distance between the two monopole sources [15].

$$|p(x,\phi,t)| = \frac{S \cdot \rho \cdot c_0 \cdot k_w}{4 \cdot \pi \cdot x} \cdot k_w \cdot d \cdot cos(\phi) \qquad \text{(Eq. 2.7)}$$

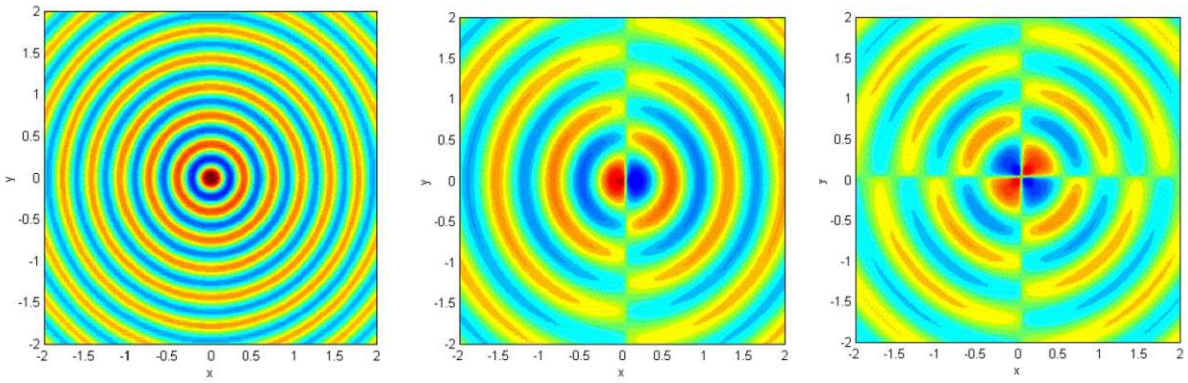

Figure 2.4: Acoustic sources and propagation: monopole (left), dipole (middle) and quadrupole (right) [16]

If all alternating forces can be compensated, the sound source shows a quadrupole character (see Fig. 2.4, right). As already mentioned for the dipole source, several monopole sources, in this case four, can form a quadrupole one. Such sources are arranged in alternating phases and are characterised by horizontal (d_h) and vertical (d_v) distances between each other, see equation 2.8. In addition, two oppositely oriented dipole sources can also be considered as a quadrupole source [14]. The difference to the dipole source, however, is visible in the additional sine term besides the already existing cosine one.

$$|p(x,\phi,t)| = \frac{S \cdot \rho \cdot c_0 \cdot k_w}{4 \cdot \pi \cdot x} \cdot 4 \cdot {k_w}^2 \cdot d_h \cdot d_v \cdot cos(\phi) \cdot sin(\phi) \qquad \text{(Eq. 2.8)}$$

2.2 Aeroacoustic analogies

As mentioned in the introduction chapter, the first experimental approaches to reduce the noise emitted by propellers were already carried out in the 1920s. To the present day, there is no complete scientific theory of how noise is generated by aerodynamic flows.

However, prediction methods have been developed starting with Gutin in 1936 [17] and Lighthill in 1952 [18]. With the rise of the processing power of computers, further noise prediction models were established based on the governing equations of Lighthill. In the following subchapters, the most important aeroacoustic analogies are described in more detail.

2.2.1 Lighthill´s governing equations

Sir James Lighthill compared the equation for fluid motion with the equation of sound propagation and applied specific limitations. The starting point for his considerations were the Navier-Stokes equations for the conservation of mass (Eq. 2.9) and the conservation of momentum (Eq. 2.10) [19].

$$\frac{\partial \rho}{\partial t} + \nabla \cdot (\rho \boldsymbol{v}) = \frac{D\rho}{Dt} + \rho \nabla \cdot \boldsymbol{v} = 0 \qquad \text{(Eq. 2.9)}$$

$$\rho \frac{\partial \boldsymbol{v}}{\partial t} + \rho(\boldsymbol{v} \cdot \nabla)\boldsymbol{v} = -\nabla p + \nabla \cdot \boldsymbol{\sigma} \qquad \text{(Eq. 2.10)}$$

The fluid is given by its density ρ and velocity vector $\boldsymbol{v}$, which are both time dependent variables. The thermodynamic pressure p and the viscous part of the stress tensor $\boldsymbol{\sigma}$ are also given in the equations. After some reformulation steps and notation conventions, the transformation into an inhomogeneous wave formula is completed and the Lighthill equation can be written as followed (Eq. 2.11 -2.12): [18]

$$\frac{\partial^2 \rho}{\partial t^2} - c_0^2 \nabla^2 \rho = \frac{\partial^2 T_{\mathrm{ij}}}{\partial x_{\mathrm{i}} \partial x_{\mathrm{j}}} \qquad \text{(Eq. 2.11)}$$

$$T_{\mathrm{ij}} = \rho v_{\mathrm{i}} v_{\mathrm{j}} - \sigma_{\mathrm{ij}} + (p - c_0^2 \rho)\delta_{\mathrm{ij}} \qquad \text{(Eq. 2.12)}$$

The Lighthill stress tensor $\boldsymbol{T}$ consists of several sections, which are controlled by various factors. The first term $\rho v_{\mathrm{i}} v_{\mathrm{j}}$, which is also known as the Reynolds stress tensor, represents the unsteady convection of a flow. The tensor $\boldsymbol{\sigma}$ describes the sound generated by viscosity, which is very low for high Reynolds number flows. The last expression $(p - c_0^2 \rho)\delta_{\mathrm{ij}}$ indicates the excess momentum transfer due to pressure, which can be neglected for an incompressible flow [7].

2.2.2 Curle analogy

The Curle analogy can be applied to determine acoustic noise generated by a flow in near and far field [20]. It is based on Lighthill`s general theory of aerodynamic sound but extends it to include solid surfaces. Curle describes the sound field as the sum of the volume propagation of quadrupoles and the two-dimensional distribution of dipoles on the surface of a solid [21]. One limitation of this analogy is that it only applies to flows with low velocities.

If the Mach number is too high, the sound field from the quadrupoles will completely dominate, which influences the accuracy of the results. Furthermore, this analogy is only suitable for non-deformable static surfaces, which do not meet the requirements for the simulation conditions of this thesis [16].

2.2.3 Ffowcs-Williams-Hawkings analogy

The Ffowcs-Williams-Hawkings (FWH) analogy is also based on Lighthill`s general theory of aerodynamic sound and it is applicable to aeroacoustic sources with relative motion to a solid surface. In comparison to the Curle analogy, the equations also consist of a monopole term [22]. This is the most relevant analogy because of the moving impenetrable blade surfaces of the propeller during the simulation. Equation 2.13 is only one possible variant of expressing this analogy [7].

$$\rho'(\boldsymbol{x},t)c_0^2 = \frac{\partial^2}{\partial x_\mathrm{i}\partial x_\mathrm{j}}\int_{V_0}\left[\frac{T_{\mathbf{ij}}}{4\pi r|1-M_\mathrm{r}|}\right]_{\tau=\tau*} dV(\boldsymbol{z}) - \frac{\partial}{\partial x_\mathrm{i}}\int_{S_0}\left[\frac{p_{\mathrm{ij}}\cdot n_\mathrm{j}}{4\pi r|1-M_\mathrm{r}|}\right]_{\tau=\tau*} dS(\boldsymbol{z}) + \frac{\partial}{\partial t}\int_{S_0}\left[\frac{\rho_0\cdot V_\mathrm{j}\cdot n_\mathrm{j}}{4\pi r|1-M_\mathrm{r}|}\right]_{\tau=\tau*} dS(\boldsymbol{z}) \qquad \text{(Eq. 2.13)}$$

The defined integrals and variables for density (ρ', ρ_0), time (t), velocity (V), speed of sound (c_0) and Mach number (M) at a certain retarded time τ as well as the unit normal vector $\boldsymbol{n}$ are part of this formulation. Without explaining each individual parameter in detail, the above representation of the formula shows that monopole, dipole and quadrupole sources are all present in this analogy. The first term which contains the Lighthill stress tensor $\boldsymbol{T}$ represents again the quadrupole volume source. The surface loading tensor $\boldsymbol{p}$ in the second expression correspond to a dipole surface source and the last term defines a volume displacement source as an integral over a surface, which has a monopole character [23].

Due to the enormous computational effort that requires a detailed mesh all the way to the observer positions in the far field, this analogy has the capability to implement a control surface. Thus, a hybrid approach can be chosen, which separates the computation of the flow field from the acoustic solution. The data collected on the FWH surface are further processed to calculate the propagation of acoustic waves to the predefined microphone positions. The quadrupole source term can be neglected for these calculations, since the simulations of this thesis do not take place in the transonic domain. This is taken into account in the Farassat 1A formulation, which is an integral representation of the FWH equation. Thus, a time-consuming volume integration can be avoided [24].

2.3 Sources of propeller noise

The noise generated by a propeller during motion has several sources. In order to improve the aeroacoustic behaviour of propellers, it is important to know where the noise is emitted and what specific part of the propeller is responsible for it. Moreover, the shares of the different sources of total noise and the interaction between each other need to be comprehensible. The corresponding fundamentals are explained in more detail in this subchapter.

According to a NASA report [25] the propeller noise can be categorised into three sections (harmonic, broadband and narrow band random noise) as well as three types of sources (steady, unsteady and random source). Fig. 2.5 shows an overview of the most common noise sources for propellers and a classification with respect to the previously mentioned categories [25].

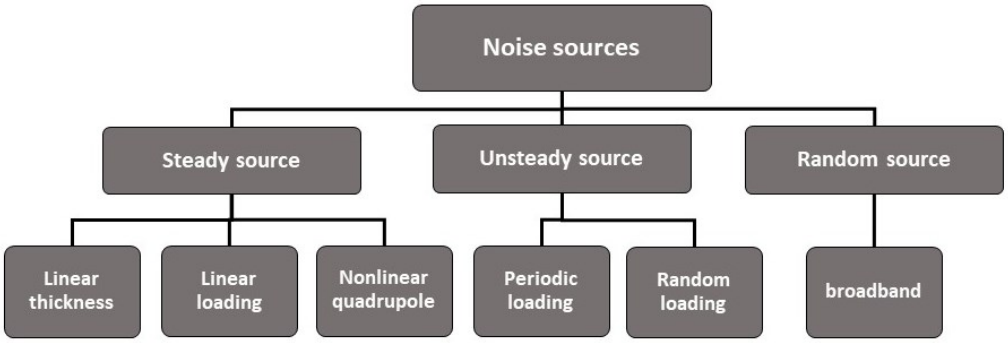

Figure 2.5: Propeller noise sources categorised according to the source type [25]

The harmonic noise is generated by a signal at discrete frequencies as a function of the passing frequency of the blade. This periodic fundamental blade passing frequency (BPF) depends on the number of blades *B* as well as the constant rotational speed *n* in rotations per minute (RPM) and can be calculated using the following equation 2.14 [24].

$$BPF = n \cdot {}^{B}/_{60} \qquad \text{(Eq. 2.14)}$$

It is limited to a certain number of frequencies as well as their multiples, and the major contributors are thickness and loading noise which can be seen in figure 2.6 (a) [26]. Broadband noise on the other hand shows a continuous frequency spectrum with random small amplitude peaks at different points of time (see Fig. 2.6 (b)). Vortex noise and turbulence induced noise are the most relevant sources for broadband noise [27]. The narrow band random noise, which is displayed in figure 2.6 (c), shows periodic character, although the amplitudes are not always equally developed. This almost continuous spectrum forms the transition between the discrete harmonic noise peaks and the largely unchanged broadband noise [25]. In the following subchapters, the thickness, loading as well as broadband noise are described in more detail.

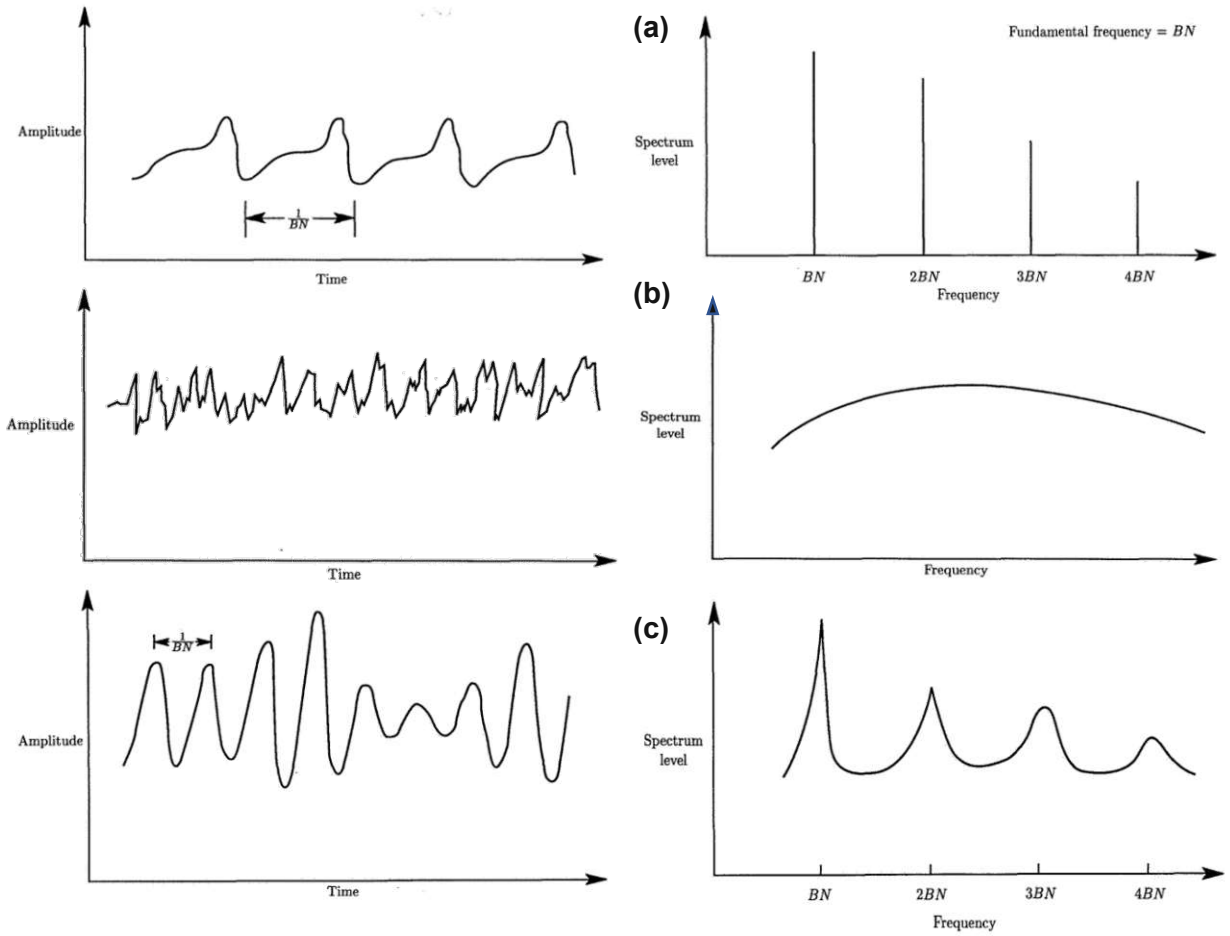

Figure 2.6: Schematic representation of harmonic noise (a), broadband noise (b) and narrow band random noise (c) amplitudes displayed over time (left) and the corresponding frequency spectrum(right) (BN = BPF) [25]

2.3.1 Thickness noise

The thickness noise is caused by the periodic displacement of air as a result of the rotating propeller blades. The term originates from the blade's thickness, which displaces a corresponding amount of air volume and thus controls the amplitude magnitude. Furthermore, the cross section of the blade as well as the rotational velocity determine the frequency output of this noise source. In general, it can be stated, that a greater flow deflection as well as a higher rotational velocity increase the thickness effect [25].

As already mentioned in chapter 2.2, the source of thickness noise shows a monopole character, because a time-varying volume flow is responsible for the sound generation. The angle of attack of the blades as well as the camber do not influence the strength of the source as much as the thickness. The propagation of the thickness noise is particularly noticeable in the plane of rotation [26].

2.3.2 Loading noise

The pressure distribution of a rotating propeller blade relative to a surrounding medium consists of a thrust and a torque component depending on their orientation towards the plane of rotation (thrust - normal to plane, torque - in plane). The disturbance of the pressure field by steady as well as unsteady lift and drag forces is responsible for the noise [27]. There are different types of loading noise depending on the source, which can be steady or unsteady (see Fig. 2.5). Linear loading sounds, which are constant in time to an observer, generate periodic noise. Periodic and random loading noise originate from an unsteady source, which makes them time dependent. Moreover, the propagation of the loading noise, which shows a dipole character, is primarily in the aft direction but also to a certain extent to the front of the rotating propeller. The thickness and loading noise are the major contributors to propeller noise [26].

2.3.3 Broadband noise

As already mentioned in the introduction of chapter 2.3, broadband noise is characterized by similar spectrum level values over a large frequency range. The reason for that are the multiple vortices which are formed and shed in a flow past a blade. This defines the term vortex noise, which is the major source for broadband noise. Due to the different cross-sections and velocities of the flow along the span of the blade, it is not a constant value [27].

Both, leading and trailing edge of the blade, contribute to the noise creation. The turbulent inflow, which leads to the characterization as a random source, forms a turbulent boundary layer on the blade surface [25]. The interaction of this flow with the trailing edge or the blade tips can lead to relevant noise sources at large angles of attack. The broadband noise source and propagation show dipole character and its propagation is similar to the one of the loading noise [26].

2.3.4 Quadrupole noise

The non-linear steady noise source with quadrupole character does not cover many fields of application in propeller acoustics. However, at high rotational velocities and corresponding transonic or subsonic blade tip Mach numbers, it has an influence on the noise output [28]. On the one hand, this can be seen by the increase in linear thicknesses as well as loading source noise. The propagation therefore is both in the direction of the axis of rotation and within the plane of rotation. On the other hand, the noise increases for propellers with no sweep and high tip speeds. Moreover, the blade vortex interaction (BVI) noise also accounts for this type of acoustic emission [25].

2.4 Turbulence modelling

There are many approaches for modelling the turbulence properties of the associated simulation. In OpenFOAM it is possible to choose between three turbulence models. These are the Reynolds Averaged Simulation (RAS bzw. RANS - Reynolds Averaged Navier-Stokes), the Detached Eddy Simulation (DES) and the Large Eddy Simulation (LES) model [29].

A RANS turbulence model for incompressible flow is selected because it is not as computational expensive as the DES or LES model. Furthermore, the RANS model allows to use more geometrically and mathematically complex models than the other ones. The reason for that lies in the time averaging process of the Reynolds average Navier-Stokes equations which is based on the fact that there is only one length scale that covers the entire turbulent spectrum and thus saves calculations for several different scales, especially with regard to the mesh sizes. This offers the possibility to implement a hybrid approach. However, a specific representation of detached eddies due to turbulence at a certain scale is not possible with the RANS approach. Nevertheless, since the acoustic measurements take place far away from these local phenomena, the time averaging process related to several orders of magnitude is the better choice [30].

Additional closure models were implemented in OpenFOAM to adapt the calculation process of turbulence problems and remove fluctuating components. The $k - \varepsilon$ turbulence model, which is based on the turbulence kinetic energy *k* and the turbulent kinetic energy dissipation rate *ε,* is used for the present work. These parameters redefine the eddy viscosity relationship. Additionally, by applying this turbulence model, good aerodynamic results can be achieved in the near wall region, which corresponds to the propeller blade. Since this is the source of the turbulence induced noise, high accuracy is essential. The relevant equations with the corresponding model coefficients can be found in literature [31].

Special attention also needs to be paid to the boundary layer transition computation of CFD solvers. According to [30], there are two types of transition models which differ by the reference to the stability theory. As the transition point depends mainly on the Reynolds number, surface parameters, freestream flow conditions as well as the pressure gradient and pressure fluctuations, determining its exact location is computationally expensive. Accordingly, a distinction can be made between models that have a specified transition onset and those that can predict the transition point. For most airfoils and operating conditions in this field of application, the transition takes place near the leading edge. Therefore, no interference or complications are to be expected regarding the selection of the appropriate model.

3. Propeller design parameters and geometrical modifications

In this chapter, the influence of the design parameters and geometrical modifications on the aerodynamic and aeroacoustic behaviour of propellers is summarised. The associated literature research shows which features have a positive effect and are thus part of the optimised propeller geometry concept presented in chapter 7. In the validation process in chapter 6, a few of these features are also included, but due to the limited data available, it is not possible to validate the simulation model regarding all adaptations.

3.1 Fundamental parameters

The selection of certain design parameters, such as blade sweep, thickness ratio, pitch angle, number and shape of the blades as well as propeller diameter and airfoil selection can already have a significant influence on the aerodynamic and aeroacoustic behaviour [25]. Some of these, namely the number of blades and the diameter, are predefined in the upcoming simulations and are therefore constant, which is why the effect of changing them is not investigated. Other fundamental propeller parameters that serve as reference values are explained briefly. These include the advance ratio J, which expresses forward motion as a function of rotational velocity and propeller diameter, and the propeller propulsive efficiency η_p. The correlation of these two variables, as a function of the pitch angle β, is shown in figure 3.1. Furthermore, they depend on the inflow velocity V, the propeller rotational velocity n, the propeller diameter D as well as the generated thrust T and torque Q. The multiplication of torque and rotational velocity results in the mechanical power P (see formula 3.1 – 3.2) [32].

$$J = \frac{V}{n \cdot D} \qquad \text{(Eq. 3.1)}$$

$$\eta_p = \frac{T \cdot V}{2 \cdot \pi \cdot P} = \frac{T \cdot V}{2 \cdot \pi \cdot n \cdot Q} \qquad \text{(Eq. 3.2)}$$

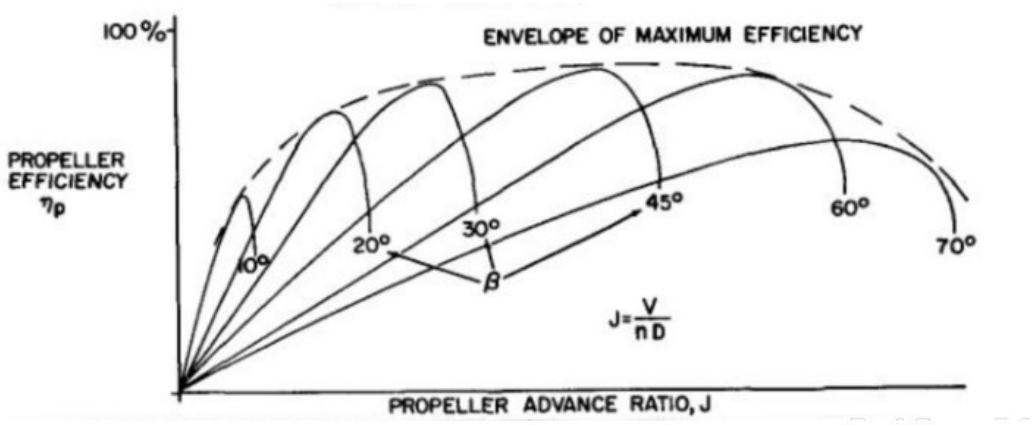

Figure 3.1: Propeller efficiency as a function of the advance ratio J and pitch angle β [32]

3.1.1 Pitch angle

On the one hand, the angle between the plane of rotation of the propeller and the chord line of the corresponding airfoil section is defined as pitch angle *β*. The twist angle, on the other hand, is specified as the total angle difference between profile root chord line and profile tip chord line. For modern efficient propellers the pitch angle varies along the radial position of the blade, which can be seen in figure 3.2. The reason for this adaptation is to distribute the loading evenly along the blade span as the velocities on the blade surface increase with the radius. To do so, the angle of attack of the airfoils is adjusted depending on the radial position on the propeller to control the thrust generation. This leads to large pitch angles at the root and smaller ones at the tip [12].

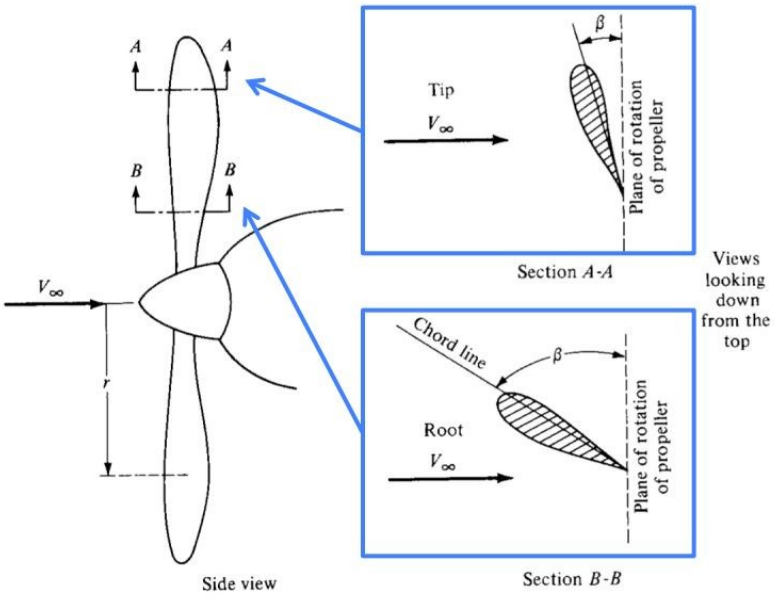

Figure 3.2: Pitch angle β at two different propeller blade cross sections [33]

The usual notation of propellers of different size is with two numerical values, where the first number represents the diameter *D* and the second number stands for the pitch value P_b usually in inch. The latter one corresponds to the characteristic pitch value at 75% of the radius and is calculated from the given pitch angle using the following formula 3.3 [34].

$$P_b = 0{,}75 \cdot D \cdot \pi \cdot tan\beta_{r/R=0{,}75} \qquad \text{(Eq. 3.3)}$$

This pitch value is defined as the displacement a propeller produces along the rotational axis within one revolution. Accordingly, high pitch values are associated with increased thrust. A thrust compensation can be achieved by reducing the rotational speed. In terms of aeroacoustics, an increased pitch angle therefore results in higher SPL output. This can be seen in figure 3.3 for propellers with different pitch values P_b operating at the same rotational velocity. Especially at lower frequencies the SPL increase is clearly visible [12].

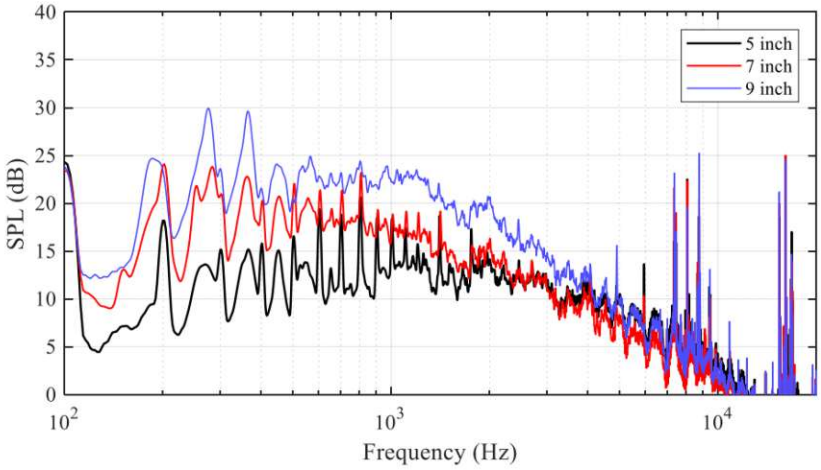

Figure 3.3: SPL output for several propellers with different pitch values P_b [35]

In principle, the pitch angle of a propeller is optimised for the corresponding application condition. However, it is possible to focus on aerodynamic performance by keeping the pitch low in order to maintain a high propeller efficiency. On the other hand, an aeroacoustic performance optimisation is possible by choosing a propeller with high pitch and low rotational velocity to reduce noise emissions. Local adjustments at specific radial positions are a promising approach to achieve optimisation without forcing a large shift towards one of the described optima [36].

3.1.2 Thickness ratio

As already mentioned in chapter 2.3, the thickness ratio can contribute to the harmonic noise as thickness noise source, which is proportional to the volume of air that is displaced by the rotating propeller blade. Therefore, it is recommended to keep the thickness value low, however, this is not always possible. Especially at the propeller blade root, a structural connection with the hub requires a certain height. The thickness ratio is normally not controlled manually by setting a value, but by selecting the appropriate airfoil at the corresponding radial position. The chord length is important here, as the thickness of the airfoil is determined as a function of the length of the chord.

A typical airfoil for drone applications, in this case a NACA 4412, can be seen in figure 3.4. Besides the thickness, the camber is another important parameter to describe an airfoil. It is defined as the maximum distance between the chord line and the mean camber line, measured perpendicular to the chord line. The mean camber line always keeps the same distance to the upper and lower surface of the profile. Furthermore, the relative position of the camber referring to the chord of the profile starting from the leading edge is usually given [37]. Propellers which are typically used for drone applications show a high camber value at a relative chord position between 40% - 50%. Furthermore, a smaller thickness to chord ratio at the propeller tip is used to increase the critical tip Mach number [38].

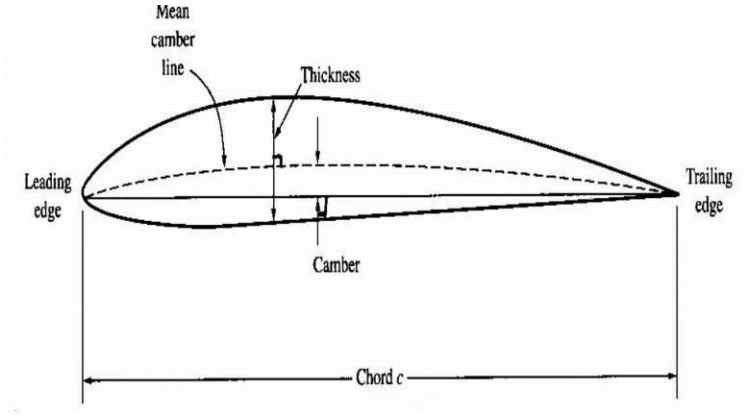

Figure 3.4: NACA 4412 airfoil with indicated parameters (not scaled correctly) [37]

3.1.3 Blade sweep

The blade sweep angle Λ is defined as the angle between the pitch axis of the blade and the line which connects the root of the blade and the centre of the corresponding chord. It depends on the radial position of the blade section and is measured within the rotational plane (see Fig. 3.5). The mid-chord alignment (MCA) can be calculated using the right-angled triangle including the current radius and blade sweep angle. It represents the offset of the current middle chord of the airfoil to the pitch axis of the propeller blade [36].

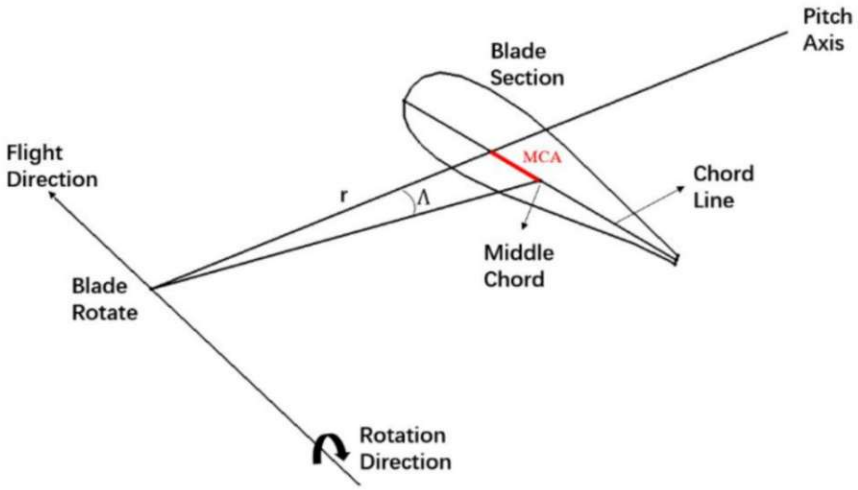

Figure 3.5: Definition of blade sweep angle Λ and mid-chord alignment as a function of the radius r [36]

The master thesis of [39] came to the conclusion that the aerodynamic efficiency is not affected by the blade sweep angle, even for very high sweep values. The thrust loss caused by the sweep is compensated by an adjusted pitch and chord value. Accordingly, a modification of the propeller geometry in terms of sweep to improve the aeroacoustic behaviour is possible without serious concerns. However, the structural integrity and manufacturability are negatively affected by too high sweep [39].

In terms of aeroacoustics, sweep can reduce monopole noise sources for specific directivity angles, which can be seen in figure 3.6 [40]. The blade sweep causes a shift of the loading noise to radial positions closer to the hub, where lower Mach numbers occur. Accordingly, a small noise reduction is noticeable. Once again, the profile Mach numbers need to be considered, which means that the effect is not valid to the same extent for all rotational velocities. According to [36], there is a relation between the mid-chord alignment and the sound wavelength, which is especially important for higher freestream Mach numbers, as the thickness noise dominates and is determined by this ratio.

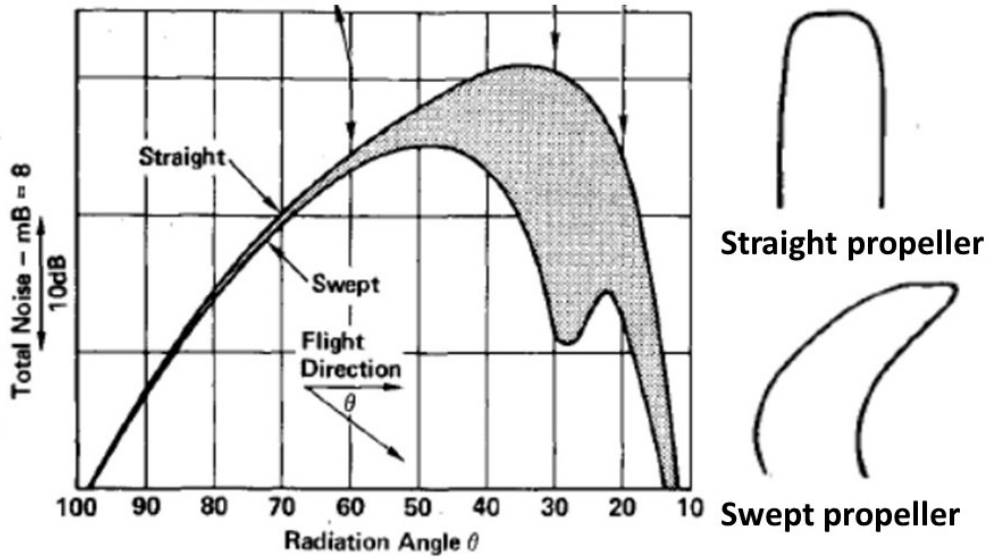

Figure 3.6: Schematic comparison of directivity noise of straight and swept propeller blades [40] (modified)

3.1.4 Chord length

As already mentioned in the section about the thickness ratio, the chord *c* is defined as the length of the straight line which is perpendicular to the pitch axis and connects leading and trailing edge. Due to the fact that the given airfoil is scaled according to the chord length, this value determines the thickness of the corresponding profile section. In terms of aerodynamics, an increase of the chord length enlarges the generated lift and drag of the profile as the blade surface area is increased. It shows a similar effect as the pitch angle, which is why a combined dimensioning of these two parameters has to be considered. It is not surprising that due to the increased chord length, a higher thickness and loading noise occurs, which is why a spanwise increase of the chord length is not recommended. However, local adjustments of the chord length can be seen as an optimisation step, both aerodynamically and aeroacoustically [12].

3.2 Additional geometrical modifications

In recent years, several additional geometrical features have been implemented that differ from the conventional propeller design. Some of them are explained in more detail in this chapter. Furthermore, these are critically reviewed, not only in terms of aeroacoustics, but also regarding aerodynamics. It is worth to mention that only adaptations that are in the same dimension as the propeller blade are reviewed. Modifications in the micro or nano range are therefore not part of this thesis. Moreover, only static geometric adjustments are considered, accordingly deformable propeller blades which help to overcome the performance changes between vertical flight and horizontal forward flight, are not taken into account.

3.2.1 Trailing edge serration

This bio-inspired adaptation of the trailing edge, which can be seen primarily by looking at the wings of birds, is a recently intensively researched topic. The modification options range from the radial positioning to the geometric shape, number and depth of the serrations. In most studies, the jags are cut out of or additionally added to the original propeller blade geometry with sharp edges, which can be seen in figure 3.7 [41].

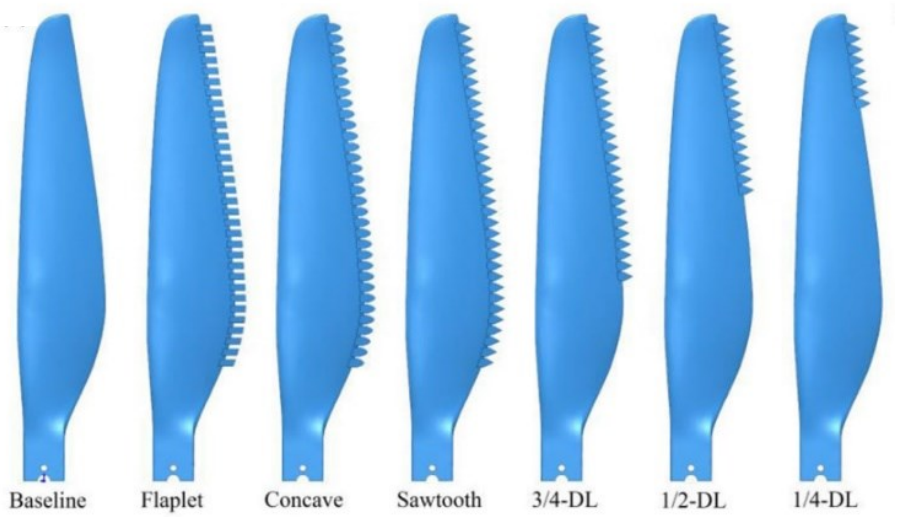

Figure 3.7: Different trailing edge serration shapes and arrangements [41]

The parameters which characterize the geometry of an individual serration are presented in figure 3.8. for a propeller blade which is serrated over half of its trailing edge. The specification is either based on a constant angle α or on a constant wavelength λ, which defines the width of a single jag. The amplitude $2h$, which characterizes the depth of the serration, also changes accordingly.

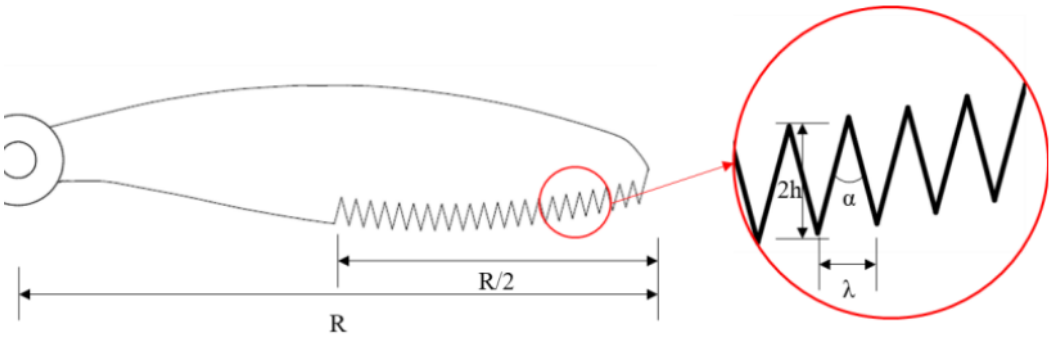

Figure 3.8: Propeller geometry with detailed view of serrated trailing edge [35]

Regarding the aerodynamic properties, in principle there are no changes due to the serration of the trailing edge for hovering flight at low Reynolds numbers. However, if the cut-outs or the additions are too large, a reduction or increase of the generated thrust can be seen, which results from the change in the blade surface area. The weakening of the structural properties of the propeller blade due to serration must also be considered and re-analysed if necessary [42].

The main effect of the serration of the trailing edge is the change of the flow structure that passes the airfoil. Due to the different chord lengths depending on the radial position, the resulting pressure distribution leads to a reorientation of the vortices which, together with the turbulent boundary layer, improves the mixing process of the upper and lower flow alongside the airfoil. The resulting redistribution of momentum and turbulent shear stress close to the serration edges leads to improved aeroacoustic behaviour [43].

In general, a reduction of the broadband noise in the high frequency range can be determined when comparing untreated trailing edges with serrated ones. This effect is most clearly recognisable at low rotational velocities and large serration amplitude values. The geometry of the individual serrations should blend into each other, meaning that removed triangles produce better results than removed rectangles. Furthermore, serrations over the entire span have not proven to be useful because modifications in the tip region have a greater influence than at the root of the blade. Once again, local adjustments are a reasonable solution [42].

3.2.2 Propeller tip modifications

The tip vortices also contribute to a large extent to the noise generated by the propeller and are therefore part of the optimisation process. But not all modifications are beneficial, a good balance must be achieved between aerodynamic and aeroacoustic output changes. Five different blade tip modifications can be seen in figure 3.9, which are briefly discussed.

Starting with the winglets (see Fig. 3.9 a), the first conflict between aerodynamic efficiency and noise is already noticeable. Both anhedral and dihedral winglets lead to higher SPL values in the medium to high frequency range. On the other hand, the thrust fluctuations are smaller and more thrust can be generated with the same rotational velocities. However, it must also be noted that the structure of the entire blade requires strengthening, as high loads act on the additional surface of the winglets at the tip. In addition, due to the numerous RPM changes, the fatigue behaviour must be analysed in detail [12]. Nevertheless, it can be stated that an adjustment of the incidence angle and thus a local swept back tip can certainly achieve a favorable result. The other two modifications of [12] shown in this thesis, namely the Ogee and Oval tip (see Fig. 3.9 b - c), show only very limited aerodynamic and aeroacoustic changes. This demonstrates that not every adjustment achieves a clear change of the output.

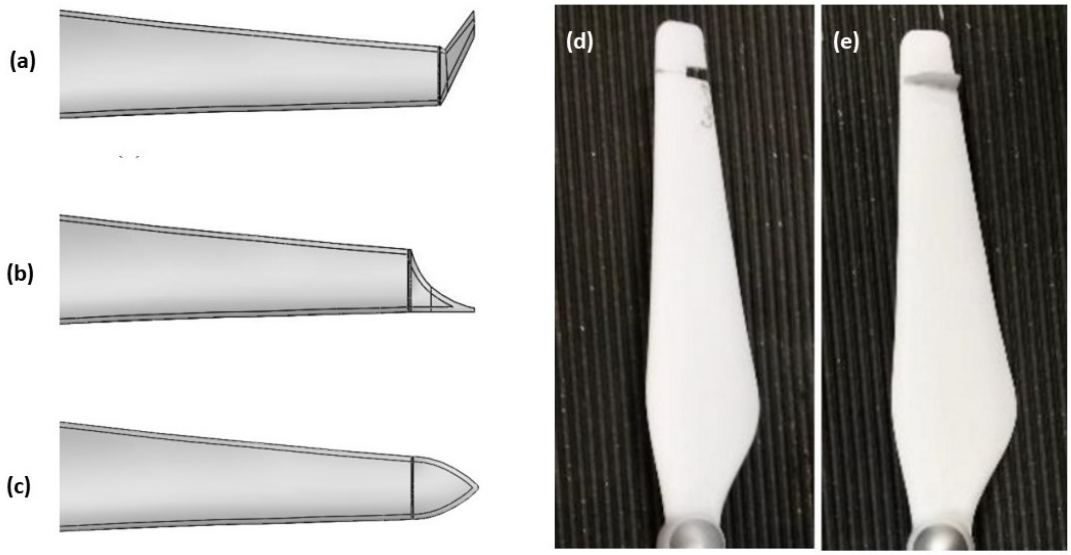

Figure 3.9: Propeller blade tip modifications: 60° dihedral winglet (a), Ogee tip (b), Oval tip (c), TE notch (d) and vortex generators (e) (a-c [12], d-e [44])

The rectangular notch at the trailing edge close to the tip (see Fig. 3.9 d) can significantly decrease sound pressure peak values that origin close to the tip of the blade. Moreover, the additional power input of the motor to maintain the same thrust is low. However, an optimal adaptation of the size and shape of this notch to the given operating conditions is necessary. Leading edge notches also result in a noise reduction, but they are not recommended from an aerodynamic point of view [44].

The final tip modification presented here is the addition of a vortex generator, known from aircraft wings, which influences the boundary layer creation of the blade locally and thus changes the wake vortex structure (see Fig. 3.9 e). This is intended to shift the tip's edge vortices away from the tip area, in order to weaken them.

The resulting reduction in the surface area that generates lift is clearly visible in the thrust comparison. Therefore, the exact positioning and shaping of this additional plate is important to achieve a decrease in noise level with minimal thrust reduction [44].

3.2.3 Leading edge tubercles

Protuberances of the leading edge, also called tubercles, are another geometric adaptation whose origin can be found in nature, for instance on the fins of whales. Their influence is visible in the delay and the reduction of the effects of boundary layer separation. Like for the serrated trailing edge, the radial position as well as the size and depth of the tubercles play a decisive role for the aerodynamic and aeroacoustic output. Several different tubercle modifications of the propeller trailing edges are displayed in figure 3.10 on the left side [45].

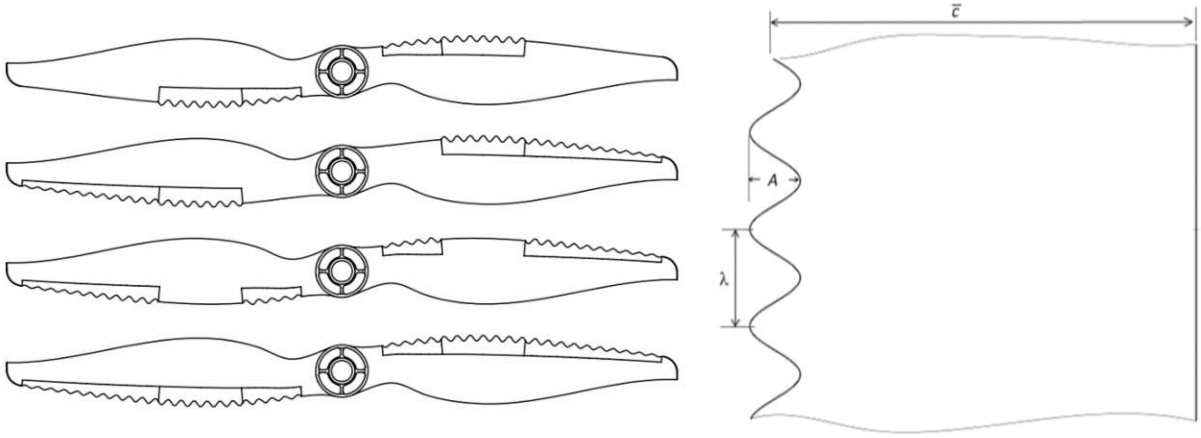

Figure 3.10: Propeller leading edge tubercles at different radial positions (left) and the tubercle control parameters: wavelength λ, amplitude A and local chord length $\bar{c}$ (right) [45]

Similar to the serration, the control parameters wavelength λ and amplitude A are also used here to describe the changes of the geometry (see figure 3.10 on the right side). Another relevant factor for referencing is the local chord length $\bar{c}$. The study conducted by [45] shows that the influence of tubercles near the root is negligible for the aerodynamic properties. The outer half of the propeller is more important, also for aeroacoustics. A constant distance between the individual protuberances is also beneficial for increasing aerodynamic performance, but local adjustments are also possible. The study concluded that certain tonal peaks can be reduced as a result of the tubercles, but a simultaneous increase in broadband noise is the consequence. Furthermore, there is a noticeable redistribution of the directivity pattern of the noise spectrum [45].

4. Computational Fluid Dynamics using OpenFOAM

The open-source Computational Fluid Dynamics (CFD) software which is used in this diploma thesis is OpenFOAM ®, which was developed by OpenCFD [29]. Although there are already newer versions of the software, the one which was released in December 2021, namely OpenFOAM v2112, is applied in order to use the externally implemented acoustic library. To perform large scale simulations in OpenFOAM, a connection to the Vienna Scientific Cluster (VSC) supercomputer VSC-4 is established. For post-processing, the software Paraview is used. In this chapter the basic structural setup of OpenFOAM is described and the main directories with the corresponding assigned files are introduced in more detail. Furthermore, the external acoustic library as well as the simulation process steps are explained.

4.1 Basic structure of OpenFOAM

At least three directories (“0”, “system” and “constant”) must be defined in order to be able to start a simulation in OpenFOAM. All the important files (bright grey) and directories (dark grey) that are relevant for this diploma thesis are shown in figure 4.1. [31]. The specifications of each directory are explained in detail in the following subchapters. A tutorial database for OpenFOAM is available online [29], which helps to understand this open source CFD software better. Additionally, well elaborated documentation is provided in the online tutorial guide [31].

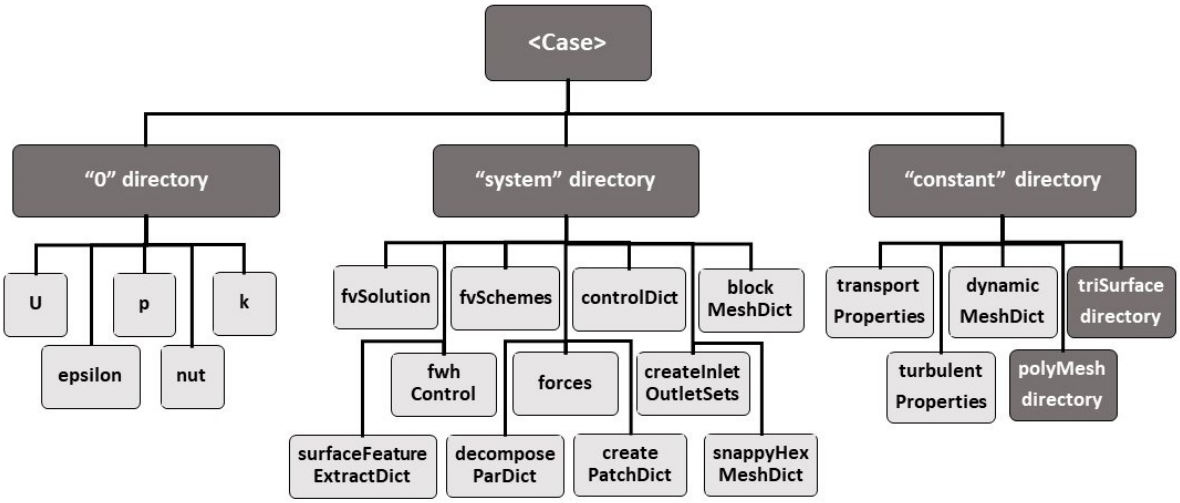

Figure 4.1: Directory and file structure of a OpenFOAM case (directories in dark grey, files in bright grey)

4.1.1 “0” directory

This directory is named after the starting time of the simulation. It contains the initial settings and boundary conditions for all primitive variables. For this diploma thesis the important initial values are velocity (*U*), pressure (*p*) and turbulent viscosity (ν_t). Furthermore, the factor for kinematic energy (*k*) as well as the one for dissipation (ε) can be found in this directory due to the chosen turbulence model which is described in more detail in chapter 2.4.
In each file the rank (scalar, vector or tensor) of the object parameter as well as the dimension of the parameter have to be defined. The dimensions of each file are described by the seven SI (International System of Units) base units, which are specified with positive and negative numbers according to the exponent of this quantity in a vector where each position refers to a certain base unit. The description of each position, quantity, unit and symbol can be seen in table 2 [31].

Table 2: Position and unit of each SI base value which is specified in OpenFOAM [31]

Position	Quantity	Unit	Symbol
1	Mass	Kilogram	kg
2	Length	Meters	m
3	Time	Second	s
4	Temperature	Kelvin	K
5	Quantity	Moles	mol
6	Current	Ampere	A
7	Luminuous intensity	Candela	cd

Furthermore, the internal field, which describes how the parameter is initialized, and the boundary field, which links the wanted boundary conditions to the predefined physical areas, must be defined for each patch in the whole domain [46]. Detailed information about the numerical boundary conditions and the specified physical areas are given in corresponding simulation chapters.

4.1.2 “constant” directory

This directory contains information about the provided mesh as well as definitions of properties for transportation and turbulence. The meshing process in OpenFOAM is described in detail in chapter 5.3. All relevant information about the mesh, including boundary, surface and point characterisations are saved in the “polyMesh” subdirectory. This directory is created automatically during the meshing process. The dictionary file of the dynamic mesh describes the motion process in terms of origin, axis, rotational velocity and involved cells.

All the geometrical surfaces which help to specify the mesh and the aeroacoustic analysis are saved in the subdirectory “triSurfaces”. The features of these surfaces are extracted during meshing in order to simplify the mesh generation process.

The transport properties file provides the solver with information about the transport model. For this diploma thesis the Newtonian model is selected, which assumes that the kinetic viscosity ν is constant. The parameter ν is defined by its unit which is m^2/s. The kinetic viscosity of air at room temperature amounts to $1.5 \cdot 10^{-5}$ m^2/s [46]. The turbulence property file is specified by the simulation type. For this diploma thesis the RAS turbulence model is chosen, as described in chapter 2.4, with the parameters kinematic energy (k) and dissipation (ε).

4.1.3 “system” directory

This directory consists of several files as shown in figure 4.1. Three of them are compulsory for all simulations, these are “controlDict”, “fvSchemes” and “fvSolutions”. The others are on the one hand needed for specifying the mesh process, on the other hand some of them represent output data functions as separate files. The control dictionary references them in the function section in order to ensure clarity of the information.

4.1.3.1 Mandatory files

The control dictionary (“controlDict”) file describes the main parameters of the simulation process as well as the functions that create output files for post processing. The simulation settings regarding the start time, end time, time step size, output interval, output format and precisions as well as time format are defined in this file. A fixed step size is especially important for comparable results regarding aeroacoustics. The function segment can have several inputs depending on the desired output. This is described in detail in chapter 4.1.3.3. In addition, the used transient solver, namely “pimpleFoam”, is defined in this file. It has been established to solve cases, in which turbulent incompressible flows of Newtonian fluids are present. Moreover, it was selected because it is also applicable to moving mesh [29].

In the “fvSchemes” file, the numerical discretization scheme, which is applied for each term of the governing equations, is specified. This gives the user the opportunity to set the desired scheme for time, gradient, divergence, Laplacian and interpolation. It is even possible to adjust individual parameters within these schemes [31]. The “fvSolutions” file defines by which solver each discretized linear equation system should be handled. Furthermore, the corresponding tolerances as well as algorithms are specified in this dictionary file [29].

4.1.3.2 Mesh and process files

For the mesh process several files are needed. The procedure and the necessary commands to access these files are explained in more detail in chapter 5.3. In this subchapter, only the contents as well as the relevance and effects of them on the simulation are explained in more detail. The task of the “blockMeshDict” file is to create a certain amount of block cells that constrain the simulation environment. This coarse hexahedron mesh is the basis for the following refinement. Furthermore, the outer boundary patches are listed in this file according to the corner points of the defined space. The “surfaceFeatureExtractDict” is needed to extract the geometrical features from the given surfaces of the propeller and the inner boundary region, which are all stored within the “triSurface” directory.

The “snappyHexMesh” file serves as a setting basis for iteration refinement of the mesh according to the extracted surface features. There are several parameters that can be adjusted to optimize the generated mesh and to fit the desired specifications. The basic procedure consists of cell splitting, cell removal and snapping according to the predefined surfaces. Furthermore, boundary layers and their respective thickness can be defined which is important for the propeller blade surface. The cell limit for the simulation geometry in this file ultimately determines the order of magnitude of the existing cells [29].

In addition, there is a file regarding the creation of patches. It is used to assign the cells to the predefined physical areas and to transfer boundary conditions. The inlet-outlet set file is necessary to assign the surfaces of the created cells to the corresponding boundary fields. In order to obtain results faster, the computational effort can be split between several processors. To do this, the “decomposeParDict” file is required which defines the number of subdomains.

4.1.3.3 Output files

For this diploma thesis, two function objects are used to obtain post processing data of forces and acoustic pressure. The forces file accesses the already implemented library “libforces”. The specification of the related patches is necessary, in addition, certain quantities such as the pressure, the velocity and the density can also be adjusted individually in this file. The output consists of separate files for the calculated forces and moments, which each provide detailed information about the pressure, viscous and porous contributions to the total value [31]. In order to obtain momentum results, the center of rotation has to be specified as well. Furthermore, since the results are given with regard to the coordinate system axes, the force results of the rotation axis correspond to the generated thrust.

The definition of the output for aeroacoustic results is saved in the “fwhControl” file. It accesses the acoustic library “libAcoustic” which is not part of the standard OpenFOAM software, therefore it has to be compiled first.

Moreover, this file contains information about the positions of the observer point and the FWH control surface. More details regarding the acoustic implementation can be found in the following chapter.

4.2 Implementation of acoustic library - libAcoustics

This is a library for near and far-field noise computation in OpenFOAM. The source code was written by Chalmers university [24] and validation for near and far field was performed by Epikhin [47]. It contains three prediction models for acoustic noise, of which the Ffowcs-Williams-Hawkings analogy is useful for the given simulation setup [20]. The frequencies and corresponding SPL values are calculated at the specified observer positions. Due to the given analogy with the corresponding control surface, a larger computational effort can be avoided, since the observers do not have to be located within the mesh. The conversion of the acoustic pressure to the sound pressure level can be carried out by OpenFOAM using the “writeFft” output option. However, an external Python script is applied for the FFT to obtain the desired frequency resolution and to simplify the post processing of the data.

The frequency range of the results depends on the time step, which is set in the “controlDict” file. With a small step size, SPL values at high frequencies can be obtained. The reciprocal of the step size corresponds to the maximum frequency at which results are calculated. The sampling rate of the acoustic library defines after how many timesteps a FFT is carried out. Consequently, the frequency increments get smaller after each transformation. Therefore, the end time has to be set according to the final desired frequency increment size [24]. Moreover, to avoid influences of the initial simulation inaccuracies, it is necessary to set the starting point of the acoustic analysis time-delayed in relation to the actual starting time of the simulation. This time shift depends on the selected time step as well as the block length of the given signal. The control surface, which is required for the Ffowcs-Williams-Hawkings analogy is saved in the “triSurface” directory. It has the shape of a cylinder which is opened on the downstream end, which corresponds to the wake region of the propeller, in order to obtain good results for the receiver microphones. A study conducted by [48] revealed that this type of control surface is the best for far field acoustic measurements because the interference with the propeller wake can be avoided. Additionally, the quadrupole noise term can be affected by a closed cylinder control surface. The dashed line in figure 4.2 represents the open end of the cylinder, which is responsible for the irregular distribution of the control surface, in reference to the propeller origin.

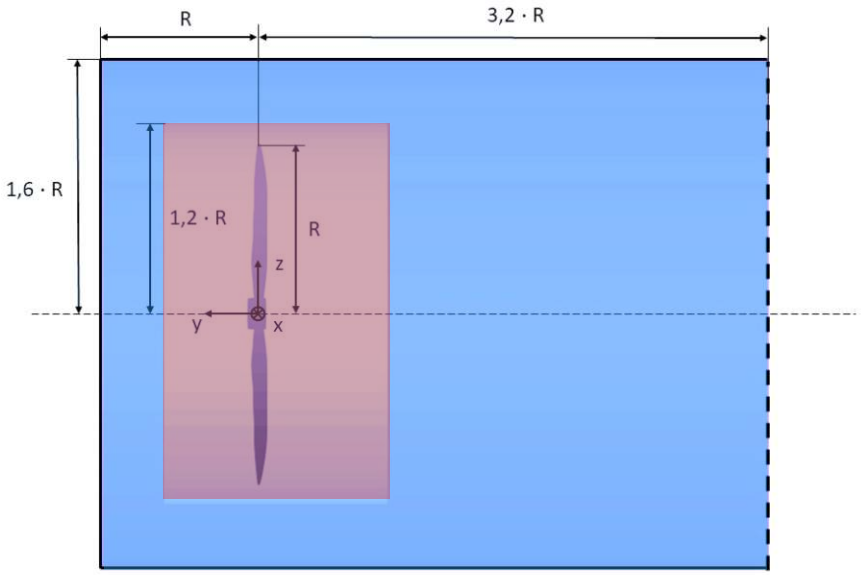

Figure 4.2: Geometric measurements of the FWH analogy control surface (light blue) and the rotating cylinder (red) in relation to the radius R of the propeller

The difference in the results due to a change of the size of the FWH control surface is negligible. However, the control surface should not be part of the rotating mesh [20]. Therefore, the diameter of the control cylinder (light blue) is chosen one third larger than the one of the rotating cylinder (red) which can be seen in figure. 4.2. Furthermore, the axial extend of the control surface cylinder is large enough so that the FWH surface is always between the observer and the propeller. There are no microphones located in the wake behind the propeller.

4.3 Simulation process

To obtain information about the accuracy of a CFD simulation, the Courant number must be checked. It is a non-dimensional quantity that connects the flow velocity (U) with the time step (Δt) and mesh size (Δh) as stated in the following equation 4.1 [49]:

$$C = \frac{U \cdot \Delta t}{\Delta h} \qquad \text{(Eq. 4.1)}$$

This parameter reflects how far the information travels through a computational grid cell in a certain amount of time. The Courant number should be below the value of one, otherwise the solution gets inaccurate, which can lead to divergence or unrealistic results depending on the integration scheme. Small time steps and a large inflow velocity help to keep this number low. The maximum Courant numbers is set in the “controlDict” file, the threshold value amounts to 0,9 for all simulations in this thesis.

5. Propeller geometry modelling and meshing process

This chapter explains on the one hand the principles of propeller blade geometry creation starting from the input parameters to the final CATIA V5 model. On the other hand, a step-by-step description of the meshing process is presented and important aspects are pointed out.

5.1 Input conversion in Phyton

The propeller blade geometry can be characterised by several parameters at multiple radial positions. These are the relative chord length, the pitch angle and the offset to the reference line. By knowing those quantities as well as the applied airfoils at several radial positions, the geometry of the propeller blade can be determined. The following table 3 shows the initial input parameters and their descriptions.

Table 3: Initial input parameters for the propeller geometry creation using a Python script

Parameter	Definition
r/R	Radial position of the cross-section
c/R	Relative chord length of the cross section
β	Pitch angle
offset	Offset to reference line

By running a Python script provided by [50], the points and connection lines (splines) of these blade cross sections as well as the trailing and leading edge guidance lines can be obtained from the input parameters and the airfoil datasets. This simplifies the import in CATIA. The Python script also offers the opportunity to interpolate between several airfoils at different radial positions. The number of cross sections is not limited but usually around 18 since most geometry data set, which are available in literature, start at a radial position *r/R* = 0,15 and end at *r/R* = 1 with a step size of 0,05. The sources for the standard propeller data in this diploma thesis are the University of Illinois at Urbana-Champaign (UIUC) Propeller Data Site [51], as well as the company Advanced Precision Composites (APC) Propellers [52].

The offset parameter is not always part of the database. This factor is needed to add the blade sweep for the geometry creation process of the Python script. It is defined as the distances from the reference center chord line to the trailing edge of the blade and can be calculated using the MCA values [50]. The number of cross sections, the corresponding profile geometry as well as the distance between those profiles can vary. Therefore, an arrangement of several cross sections in close proximity to each other offers the possibility to integrate a specific detail feature in the overall geometry of the blade.

5.2 Geometry creation in CATIA

The output of this initial Python conversion consists of multiple data points at the specified radial positions. These can be imported into CATIA V5 by running a macro in Excel which is provided by Dassault Systems and part of the installation package. In CATIA, the command “Surface with multiple sections” creates a surface which is based on the imported splines. In order to create a volume element based on this surface, the “close” feature is used. By copying and rotating the generated blade, the desired number and position of the propeller blades can be created. Adding and trimming a hub with the blades leads to the final propeller geometry, which is displayed in figure 5.1 with the reference cross section splines.

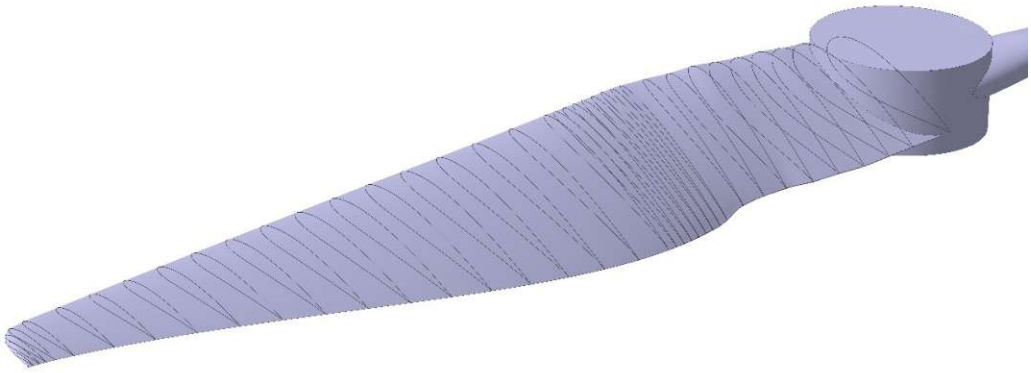

Figure 5.1: Airfoil sections along the propeller geometry modelled in CATIA V5

The created geometry has to be exported from CATIA as a "Standard Triangle Language" (STL) file and afterwards added to the “triSurface” directory for further use in OpenFOAM [29]. Furthermore, as the geometry still has the dimension of millimetres, it needs to be scaled to metres before the mesh can be created. It is important to apply the scaling after exporting to maintain a high quality of the geometry and its features as well as a high number and density of points, which are scaled.

5.3 Meshing in OpenFOAM

The meshing process takes place in OpenFOAM by using the software integrated meshing tools. Although there is no graphical user interface in OpenFOAM itself, the user can run Paraview in parallel to check the quality of the mesh. The basic structure of the simulation environment has already been outlined in the introduction of the FWH control surface in chapter 4.2, in the following paragraphs it is continued in more detail. Figure 5.2 shows the simulation setup and the most important input geometries. In principle, the propeller blade geometry is cut out of a small cylinder (red in Fig. 5.2), which rotates within a fixed environment (grey in Fig. 5.2). The boundary layer of the rotating geometry is given special consideration

during the meshing process. Another cylinder, which has the same diameter as the FWH control surface cylinder, but a larger axial extend is used as an additional boundary surface for the refinement during the mesh process (dark blue in Fig. 5.2).

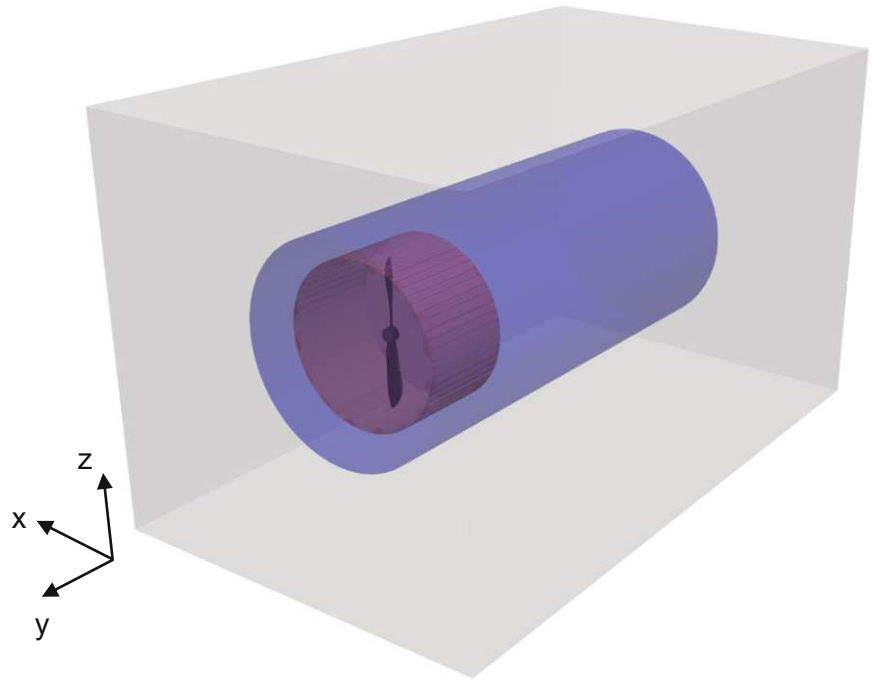

Figure 5.2: Schematic representation of the simulation setup in OpenFOAM: cylinder with cut out propeller geometry (red), simulation domain (grey) and additional cylinder for refinement (dark blue)

As already briefly described in chapter 4.1.3.2, there are certain steps that must be completed during the mesh process. First, a basis for the following refinement has to be created by filling the defined simulation domain with coarse hexahedron mesh according to the specified numbers along each axis. The outlines of these mesh blocks can still be seen in the final mesh at the external borders (see Fig. 5.3) [29]. In the next step the features of the surfaces, which are created in CATIA V5 and saved as STL files, are imported and then extracted. These surfaces, namely both cylinders, which can be seen in figure 5.2 and the propeller itself, define the boundaries at which the transition between different levels of refinement takes place. Those regions of various mesh density can clearly be seen in figure 5.3. This illustration is only a schematic representation of the mesh regions, the actual refinement depends on the simulation and geometry parameters.

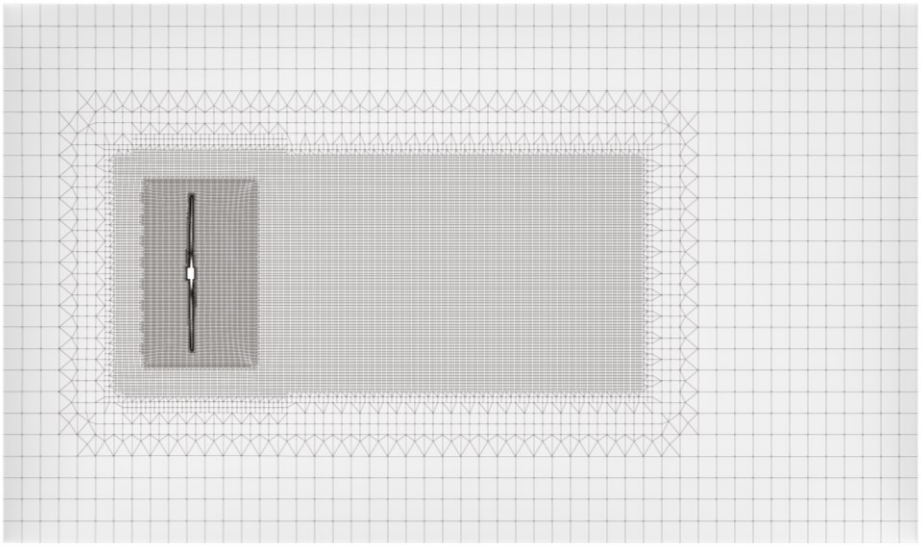

Figure 5.3: Visualisation of the mesh density in different sections of the simulation setup

The third step is the actual refinement iteration process that is performed by using the already implemented “snappyHexMesh” utility. Special attention must be paid to the transition from the rotating to the static mesh. An exact overlapping of the individual corresponding elements at any given time must be guaranteed. Otherwise, the simulation crashes due to an error regarding the dynamic mesh part. To ensure this precise superposition, boundary layers with specially sized elements are established, which can be seen in figure 5.4 on the left side. Furthermore, the first layers of the mesh on the propeller surface are shown in detail in Figure 5.4 on the right side.

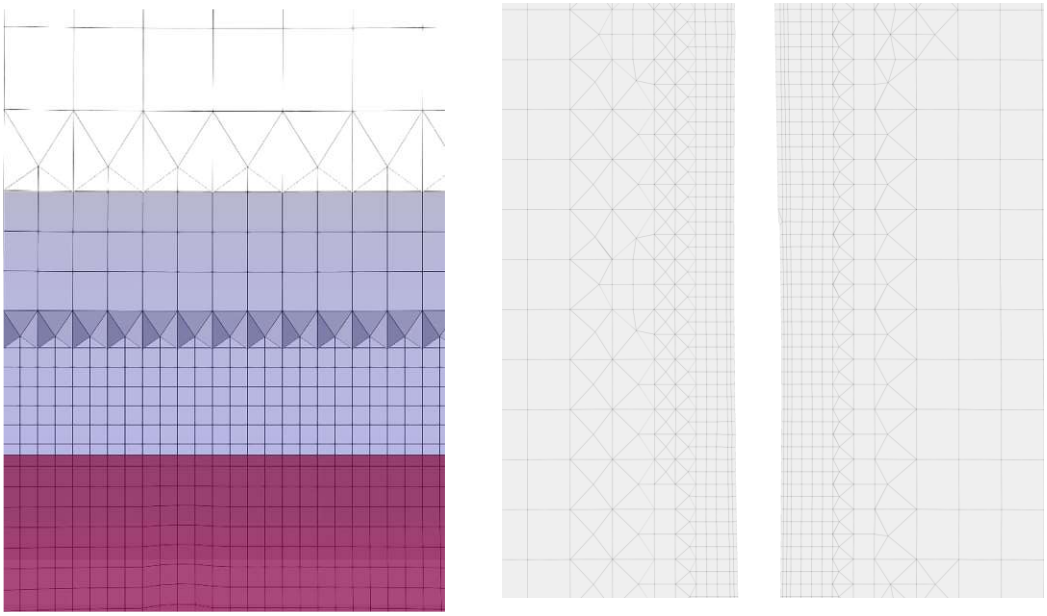

Figure 5.4: Mesh at the boundary zones between the rotating cylinder in red and the stationary region in blue(left), the first mesh layers on the propeller surface according to the y^+ value (right)

It is very important to resolve the boundary layer close to the propeller surface, which has the property of a wall, with a high enough accuracy. The size as well as number of layers of the mesh on the wall can be defined in the “snappyhex” mesh dictionary. The dimensionless wall distance (y^+) has to be selected as a value smaller than 1, in order to ensure high accuracy. Using the following equation 5.1, the thickness y of the layers close to the wall can be calculated [53]. The friction velocity u_* as a function of the wall shear stress and the kinematic viscosity ν must be known in advance.

$$y = \frac{y^+ \cdot \nu}{u_*} \qquad \text{(Eq. 5.1)}$$

Although OpenFOAM can calculate the corresponding values close to the defined wall by using implemented wall functions as boundary conditions, a fine resolution close to the surface helps to increase the quality of the results. The boundary layers are based on the mesh on the surface of the propeller, which is extruded (see Fig. 5.5).

Figure 5.5: Mesh quality on the propeller surface created by using the “snappyHexMesh” tool

In order to find out whether the specified input parameters generate the desired output and to determine the quality of the mesh, a check is initiated after the refinement is finished. After the inspection is successfully completed, the generated mesh faces have to be assigned to the corresponding boundary fields. In addition, the defined patches need to be created, updated and allocated. To decrease the computational time, the simulation is performed in 16 processors. This parallel run must be configured as the last step before the simulation can start.

6. Validation of the OpenFOAM model

Three different validation cases are considered to evaluate the simulation model regarding multiple features, which are listed in table 4. A variation of simulation setup parameters, such as rotational velocity and microphone positions, as well as multiple propeller blade geometrical modifications are investigated. These include varying airfoil shapes, pitch angles, propeller diameters and chord lengths. Furthermore, in validation case two and three, specific geometric adaptations are studied, in particular a serration of the trailing edge and a blade tip adaptation. Table 4 lists some details of each validation case, further information can be found in the corresponding subchapters. Only data for propellers with small diameters are available from open literature for model validation.

Table 4: Overview of some geometry and simulation characteristics of the validation cases

Case	Velocity (RPM)	Comment	Diameter	Reference
1	5400	-	0,23 m	[54]
2	3000	Serrated TE	0,2 m	[35]
3	4000	Tapered tip	0,37 m	[12]

For each validation case, there is a short description of the geometry and the simulation settings. The process of validating is separated in two parts, at first the aerodynamic parameters are compared to the reference. If the thrust values match the expected ones, then the aeroacoustic analysis can be implemented.

It is important to mention that there are just 2D acoustic measurements for validation, because the reproducibility is limited due to display opportunities of the data in the reference papers. To compare simulation data with experimental ones, the boundary conditions in the simulation have to be similar to the experimental setup. Since the reference experiments and simulations were all conducted under the same basic boundary conditions, they are summarized in the introduction of this chapter. The environment in which the simulations take place is air with a density of $\rho = 1{,}18\ \mathrm{kg/m^3}$, a speed of sound of $c_0 = 343\ \mathrm{m/s}$ and a temperature of 20° C.

As only the hovering flight case is considered in all three validation cases, the inflow velocity is reduced to 0 m/s to avoid influencing the resulting thrust. The coordinate system is the same for all validation cases with the y axis as the rotational axis. The propeller geometry is located in the origin of the coordinate system. The time step size is fixed to $1 \cdot 10^{-5}$ seconds for all simulations in this chapter and variations are not tolerated in order to provide comparable frequency increments. This small value is necessary to guarantee a maximum Courant number lower than 0,9. The resulting frequency resolution is set to 1 Hz for all validation cases.

6.1 Validation case 1

In the first validation case, the primary objective is to validate the OpenFOAM model using a simple, small drone propeller without any special geometry modifications. The reference article by [54] was published in 2022 and contains both experimental and simulation data.

6.1.1 Geometry and simulation input data

The most important input data of this reference paper are summarised in table 5 [54]. The geometry, in terms of pitch angle and chord length ratio of the propeller is based on a commercial APC 9 x 5 propeller but was optimised. The specified data for the pitch angle as well as the chord length ratio are displayed in figure 6.1.

Table 5: Overview of the characteristics of validation case 1

Diameter	0,23 m
Number of blades	2
Profile	$0 \leq {}^{r}/_{R} < 1$: NACA 4412
Angular velocity	565 rad/s (5400 RPM)
Frequency resolution	5 Hz (simulation) 5 Hz (experiment)

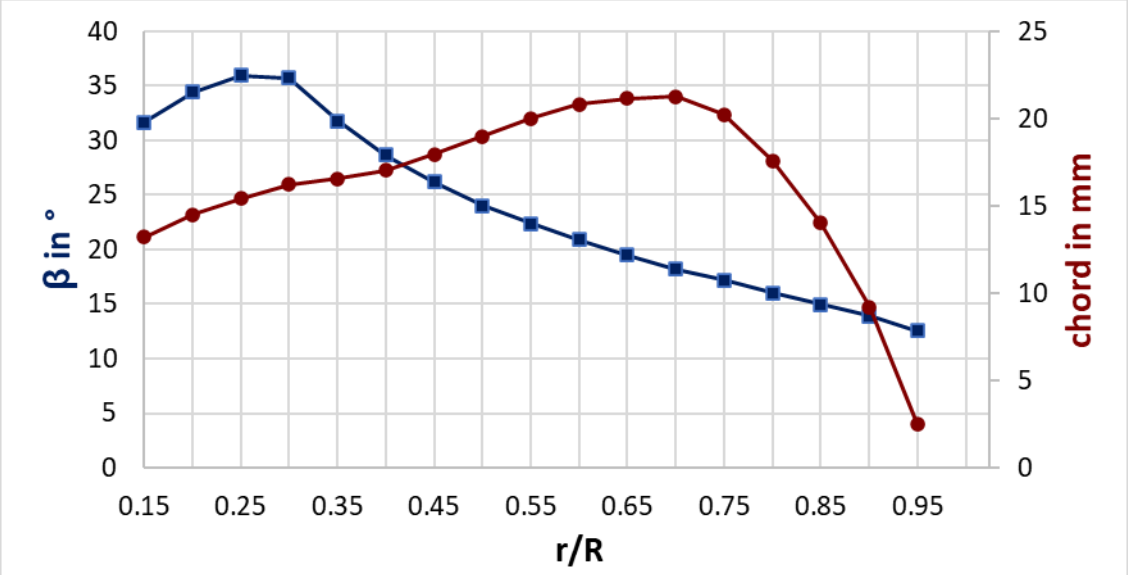

Figure 6.1: Pitch angle and chord length at multiple radial positions for validation case 1 [54]

The diameter of this adaption of the initial geometry is only 95% of the given value, as seen in figure 6.1, while the hub diameter amounts to 0,02 m. A NACA 4412 airfoil is installed for all radial positions of the cross section. The rotational velocity is the highest one for all the validation cases with a value of 5400 RPM. The top and front view of the propeller geometry used in validation case 1 are displayed in figure 6.2.

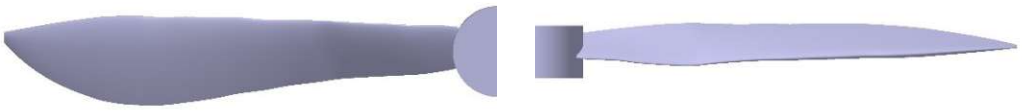

Figure 6.2: Top view (left) and front view (right) of recreated validation case 1 propeller geometry

In this paper, ten microphones are positioned at a distance of 1,5 m from the rotational axis, which means that the measurement takes place in the far field. The observer angle , referenced to the propeller center point and the rotational axis, therefore varies between 56° and 118° (see Fig. 6.3). The letter O stands for observer and the value next to it for the receiver angle θ. The rotation of the propeller is in the direction of the negative y axis.

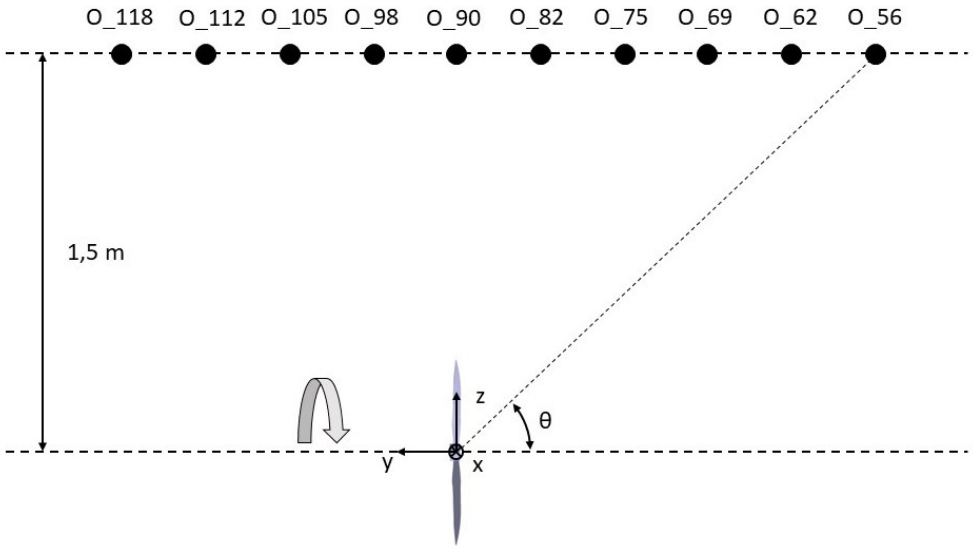

Figure 6.3: Schematic representation of observer positions for validation case 1 [54]

6.1.2 Aerodynamic validation

The thrust of the propeller is the total force in the direction of the rotational axis. It consists of a pressure component and viscous friction, the latter being the smaller part. According to the reference paper [54], the thrust produced by the propeller at 5400 RPM amounts to 2,7 N for both experimental and simulation results. The thrust obtained by the simulation setup of this diploma thesis oscillates around 2,6 N for several timesteps of the simulation. This force value is only comparable after a certain period of time, due to the fact that the initial wake is influencing the outcome in the beginning of the simulation. Therefore, the deviation to the reference article of around 4% can be explained by small differences in the geometry as well as computational effort variations.

6.1.3 Aeroacoustic validation

In terms of aeroacoustic validation, the blade passing frequency (BPF) values regarding the corresponding frequency and the associated SPL values are decisive for comparison. Furthermore, the broadband noise should remain within the given range despite fluctuations. There is already a difference between the computational and experimental reference results, which is not only due to the motor or background noise. The tonal noise varies as well and there is also a small mismatch of the BPF values, which can be seen in the figures 6.4 and 6.5 for several observer positions (red and black lines).

In general, the BPF for this validation case amounts to 180 Hz, according to equation 2.14. The peaks at this frequency and the corresponding harmonics can be reproduced with the OpenFOAM simulation. Due to the smaller frequency increment size and the different FWH control surface in the executed simulation, an increase of the SPL value of approximately 10 dB at the first BPF can be seen as displayed in figure 6.4. The harmonics of the BPF resulting from the OpenFOAM simulation are still clearly recognisable up to a frequency of 1260 Hz (see Fig. 6.4 blue line). The broadband noise fluctuates significantly at higher frequency values between 10 dB and 30 dB for the receiver at an observer angle of θ = 90°. The broadband noise shows a maximum at 3000 Hz with an averaged SPL value of 20 dB. A subsequent decrease to 15 dB at 10000 Hz can be identified.

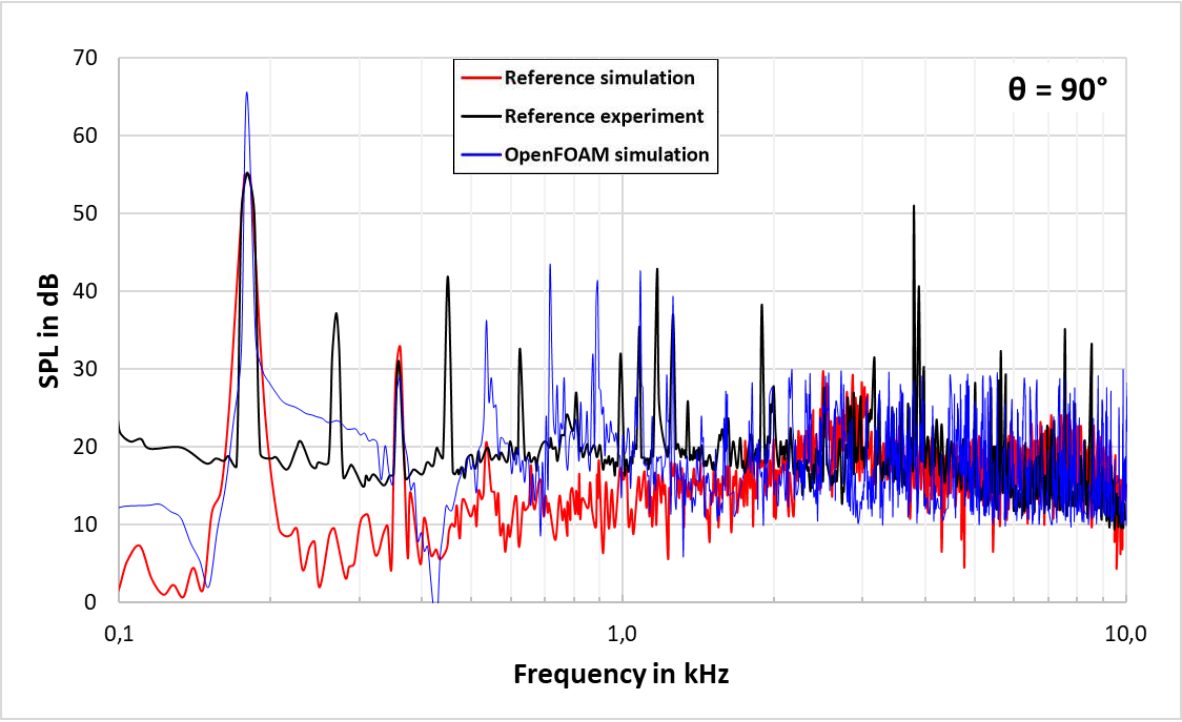

Figure 6.4: SPL results of the reference computational and experimental simulations as well as the OpenFOAM simulation plotted over the frequency for an observer at θ = 90°

The reference article [54] also provides accurate frequency spectra for additional observer positions. Four further ones, those at observer angles of 56°, 75°, 105° and 118°, can be seen in figure 6.5. As already mentioned for the microphone positioned at 90°, the BPF and the corresponding harmonics also match for the other observer locations, however, there is once again a deviation between the reference experiment and the reference simulation. Furthermore, the broadband noise values at higher frequencies are lower than the one of the references. Since the FWH control surface defined in the article is located directly at the propeller surface, a deviation from the broadband noise is not unusual, especially for the above-mentioned observers.

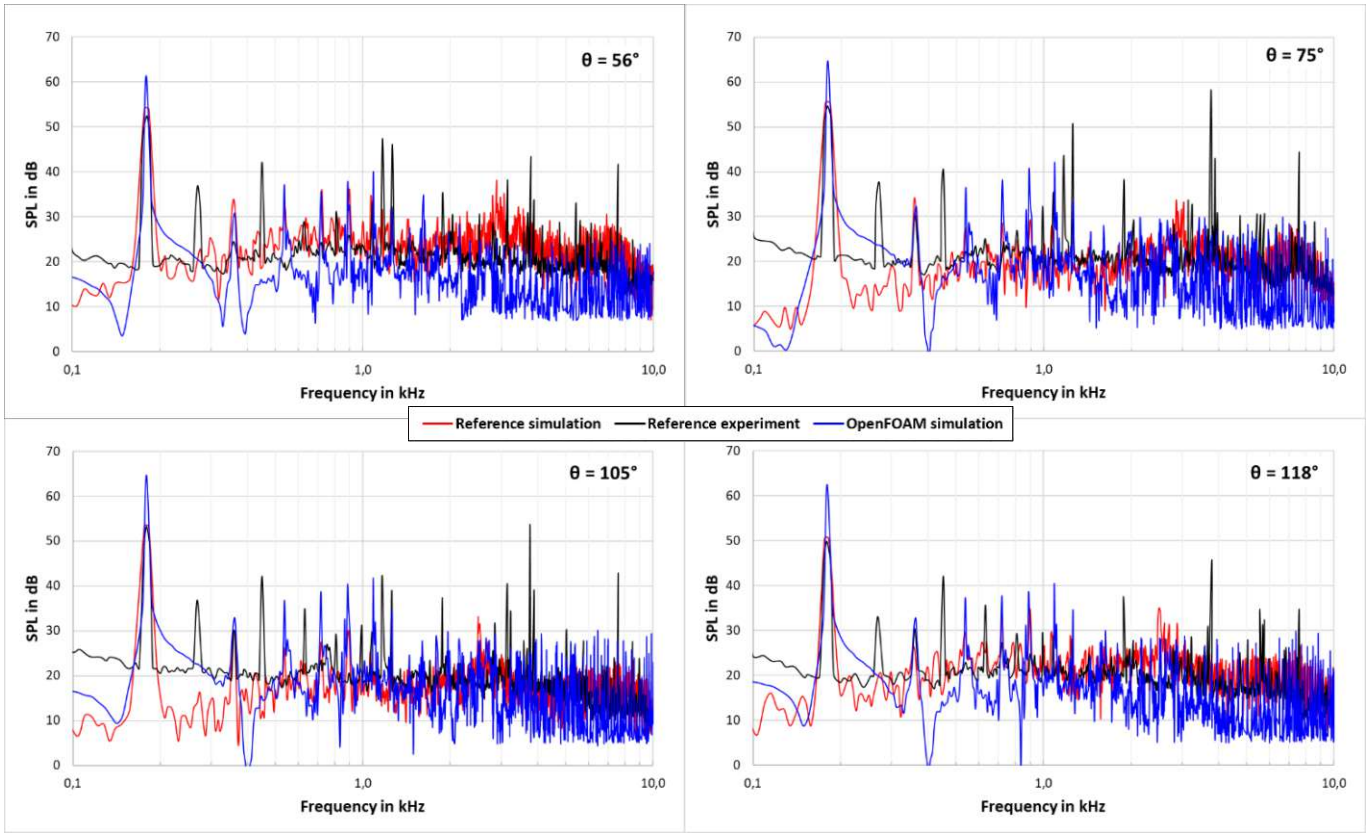

Figure 6.5: SPL plotted over frequency for observers at θ = 56° (top left), θ = 75° (top right), θ = 105° (bottom left) and θ = 118° (bottom right)

The reference used in this validation case also shows the influence of twist and chord length on the aerodynamic and aeroacoustic behaviour of the propeller. The geometry of this validation case shows an increased pitch angle starting from 0,25 *r/R* towards the tip as well as an increased chord length in the section between 0,4 *r/R* and 0,85 *r/R* in comparison to the original unmodified APC 9 x 5 propeller geometry. With these adjustments, the generated thrust results are increased by about 14%. According to the reference article, these minor modifications in the geometry indicate no significant change with regard to aeroacoustics [54].

6.2 Validation case 2

This validation case has the purpose of reproducing data of a propeller blade with a serrated trailing edge, which is described in detail in [35], with the given OpenFOAM simulation setup. The reference paper was published in 2018 and contains experimental data for several serrated trailing edges.

6.2.1 Geometry and simulation input data

The most important data are summarised in table 6. The geometry, in terms of pitch angle and chord length ratio of the propeller, is based on an APC 11 x 4,7 propeller, which is scaled to a smaller diameter, and can be seen in figure 6.6.

Table 6: Overview of characteristics of validation case 2

Diameter	0,2 m
Number of blades	2
Profile	$0{,}15 \leq {}^{r}/_{R} < 0{,}2$: NACA 4430 $0{,}2 \leq {}^{r}/_{R} < 0{,}4$: NACA 4414 $0{,}4 \leq {}^{r}/_{R} < 1$: NACA 4412
Angular velocity	314 rad/s (3000 RPM)
Frequency resolution	9,5 Hz (experiment)
Amplitude *2h*	3 mm
Angle *α*	45°
Wavelength *λ*	2,49 mm

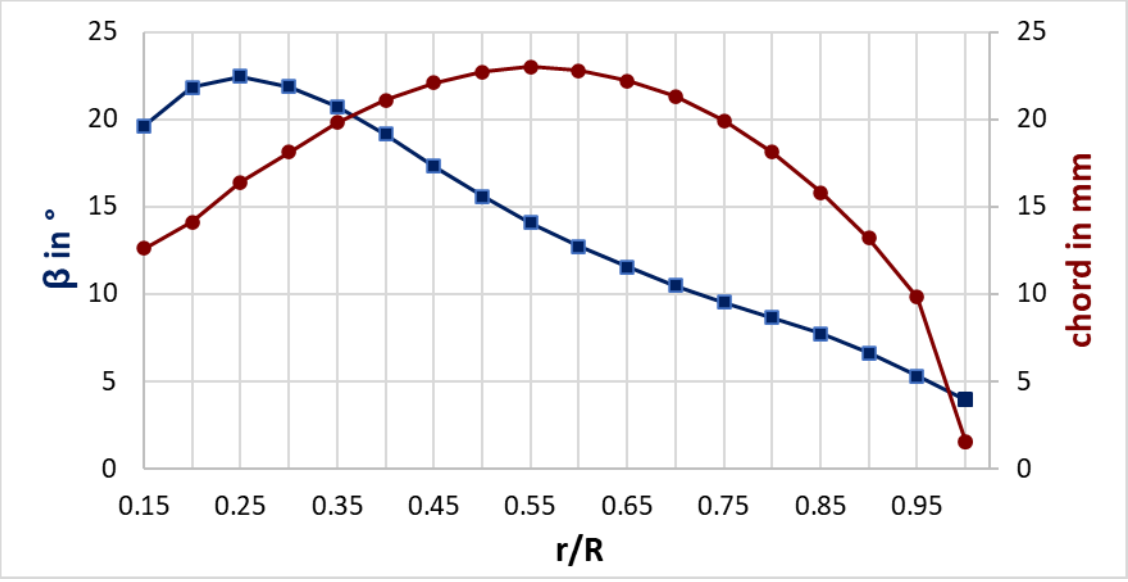

Figure 6.6: Pitch angle and chord length at multiple radial positions for validation case 2 [35]

The twist and chord length are valid for the baseline propeller. The serrated trailing edge shows other chord lengths, but since the serrations are cut out of the initial geometry, it is not reasonable to specify them, because they change due to the parameter serration angle α and wavelength λ. The corresponding values are listed in table 6. The diameter of the hub equals 0,02 m and its thickness value amounts to 0,01 m.

The airfoil changes along the radial position of the cross section starting from a NACA 4430 at the root, which offers a large thickness for structural strength. The NACA 4414 ($0{,}2 \leq {}^{r}/_{R} < 0{,}4$) serves as a transition in terms of thickness until the NACA 4412 airfoil is applied for the rest of the propeller geometry up to the tip. The rotational velocity is the lowest one for all the validation cases with a value of 3000 RPM. The top and front view of the propeller geometries used in validation case 2 can be seen in figure 6.7. The trailing edge is serrated in the outer half of the blades ($0{,}5 \leq {}^{r}/_{R} < 1$).

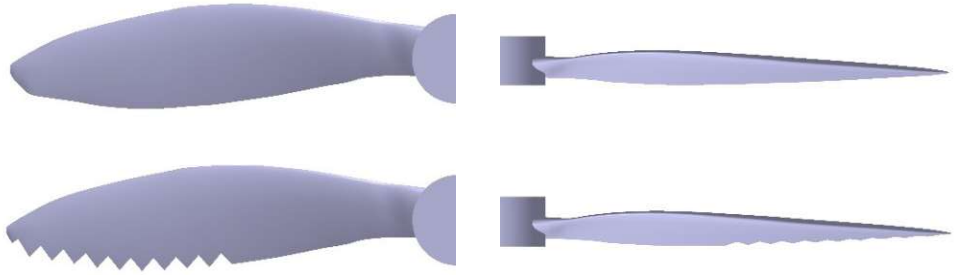

Figure 6.7: Top view (left) and front view (right) of validation case 2 propeller geometry: normal TE (top) and serrated TE (bottom)

In the experimental setup of this paper [35], 23 microphones are positioned in front of the propeller, as shown in figure 6.8. The distance from the source to the receivers is constant (R = 1,65m) and the angle difference between the observer points amounts to 5°. The rotation of the propeller is in the direction of the negative y axis.

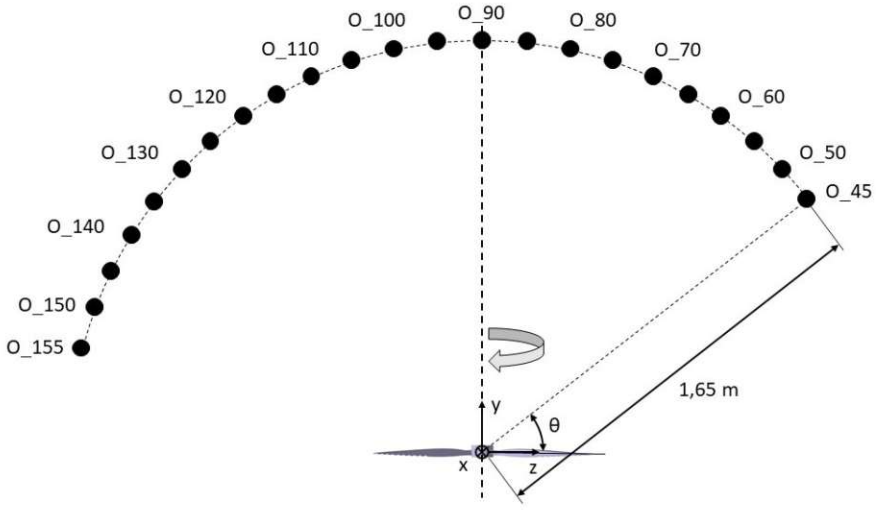

Figure 6.8: Schematic representation of observer positions for validation case 2 [35]

6.2.2 Aerodynamic validation

The reference paper does not provide detailed information about the aerodynamic analysis, it is only mentioned that the data are within the corresponding limits. According to the database [51], the propeller on which this reference case is based on, APC 11 x 4.7 Slow Flyer, the thrust coefficient c_T for the given RPM value is 0,1067. With the given data, the average thrust of the baseline propeller can be calculated according to the following formula 6.1 [55]:

$$T = c_T \cdot \rho \cdot \left(\frac{n}{60}\right)^2 \cdot D^4 = 0{,}1067 \cdot 1{,}18\ \frac{\mathrm{kg}}{\mathrm{m}^3} \cdot \left(\frac{3000\ \frac{1}{\mathrm{min}}}{60\ \frac{\mathrm{s}}{\mathrm{min}}}\right)^2 \cdot (0{,}2\ \mathrm{m})^4 = 0{,}504\ \mathrm{N} \qquad \text{(Eq. 6.1)}$$

As mentioned in chapter 3.2.1, the serration of the trailing edge decreases the produced thrust due to the reduction of the surface area. The thrust obtained by the simulation setup of this diploma thesis oscillates around 0,485 N for the unmodified trailing edge and around 0,445 N for the serrated trailing edge, as seen in figure 6.9 for several timesteps of the simulation. This results in a thrust difference of about 8%. It is important to mention that the generated thrust is very low for this specific setup which can be explained by the small propeller diameter and the low rotational velocity.

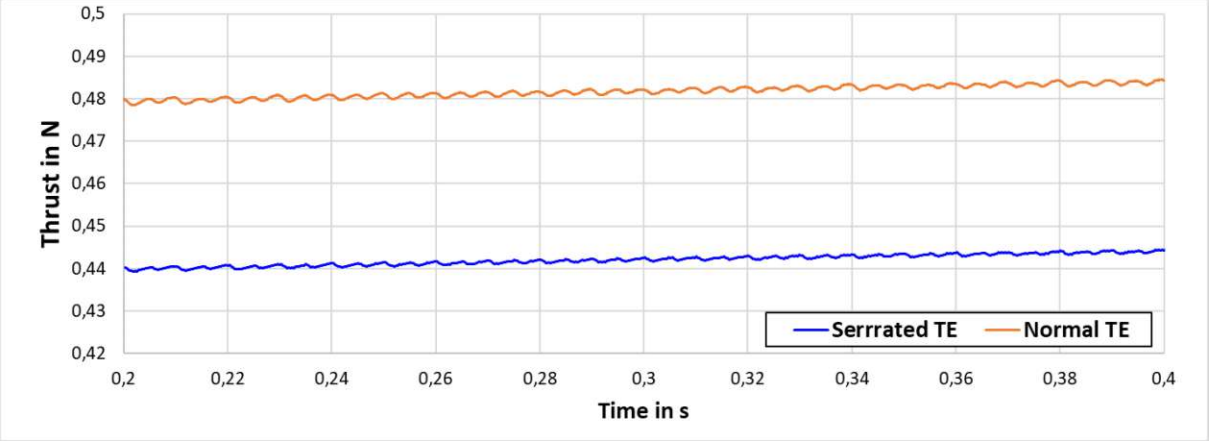

Figure 6.9: Generated thrust of the different propellers of validation case 2 plotted over time

6.2.3 Aeroacoustic validation

The aeroacoustic validation is divided into two sections: First, the reference values are compared with the output of the OpenFOAM simulation for an unprocessed and a serrated trailing edge at an observer angle of 90° (see Fig. 6.10). In the second part, directivity charts are generated using the data from the numerous microphones at the BPF and its first three harmonics, which show the directional behavior and can also be compared with the reference.

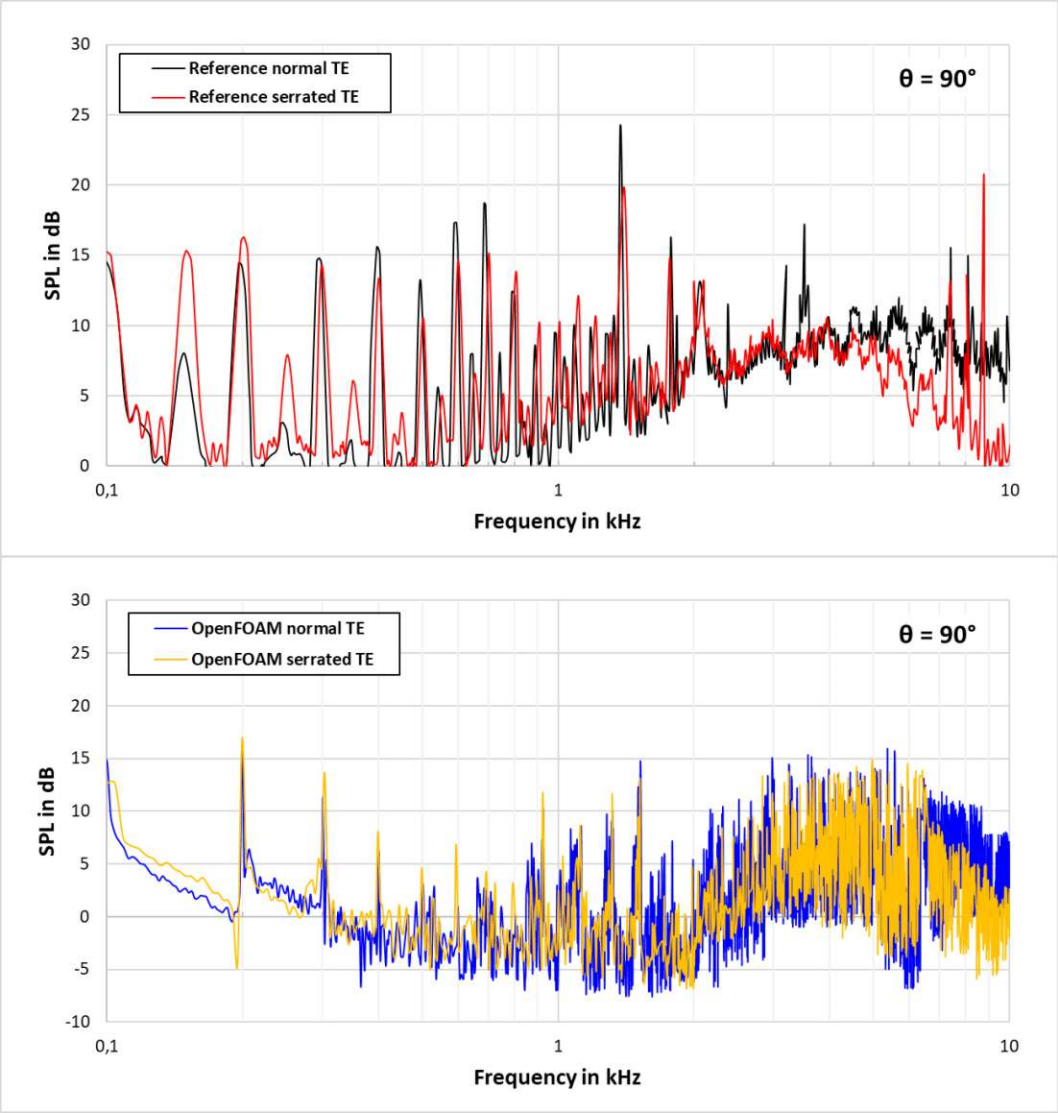

Figure 6.10: SPL plotted over frequency for an observer at θ = 90°: reference normal TE and reference serrated TE simulation (top) and OpenFOAM normal TE and OpenFOAM serrated TE simulations (bottom) [35]

The results from [35] show that the BPF amounts to 100 Hz, which is confirmed by equation 2.14, although there are also peaks visible at frequencies directly in the middle of two harmonics. In addition, the case with the serrated TE is responsible for slightly higher tonal noise peaks at low frequencies, but this changes to the opposite at higher frequencies. In the upper graph of figure 6.10 it can clearly be seen that the serration reduces the broadband noise for frequency values higher than 4000 Hz. The results obtained by the OpenFOAM simulation show a similar behaviour (see Fig. 6.10 bottom). Furthermore, the fluctuations of the SPL values differ between the reference models and the simulated ones. At high frequencies, the simulations performed in this thesis oscillate much more than the experimental ones by [35]. This is due to the large number of data points provided for the FFT. Pressure pulsations therefore have a greater influence.

In the reference diagram, the negative SPL values are just indicated, in the OpenFOAM simulation they become clearly visible. The reason for that can be found in the formula which is used to calculate the SPL, which is stated in equation 2.2. SPL values lower than 10 dB can be achieved with an acoustic pressure p_{acoustic} smaller than $6{,}3 \cdot 10^{-5}$ MPa. If this parameter gets lower than the reference pressure ($p_{\text{ref}} = 2 \cdot 10^{-5}$ MPa), the SPL output is negative. Due to this very narrow value range, it is important to correctly set the tolerance parameters for simulations that create small SPL value output. This shows the limitations of the given OpenFOAM simulation model.

When considering the directivity behaviour, some similarities, but also differences can be identified for the results shown at four different BPF values in figure 6.11. It is important to keep in mind that the following figures show the noise output in front of the propeller and not the lateral noise pattern. For the second to fourth BPF, the reference paper indentifies a dipole source which is characteristic for loading noise. The results of the OpenFOAM simulation only indicate a dipole character for the first and fourth BPF, which is turned by 90 degrees and corresponds to the actual direction of propagation of the loading noise, which is in front of and behind the propeller. The second and third characteristic frequency display a monopole noise source which is associated with thickness noise. The similarities can be clearly seen except for the fourth BPF. Due to the existing deviations between experimental and computational results, it is difficult to make a definite statement.

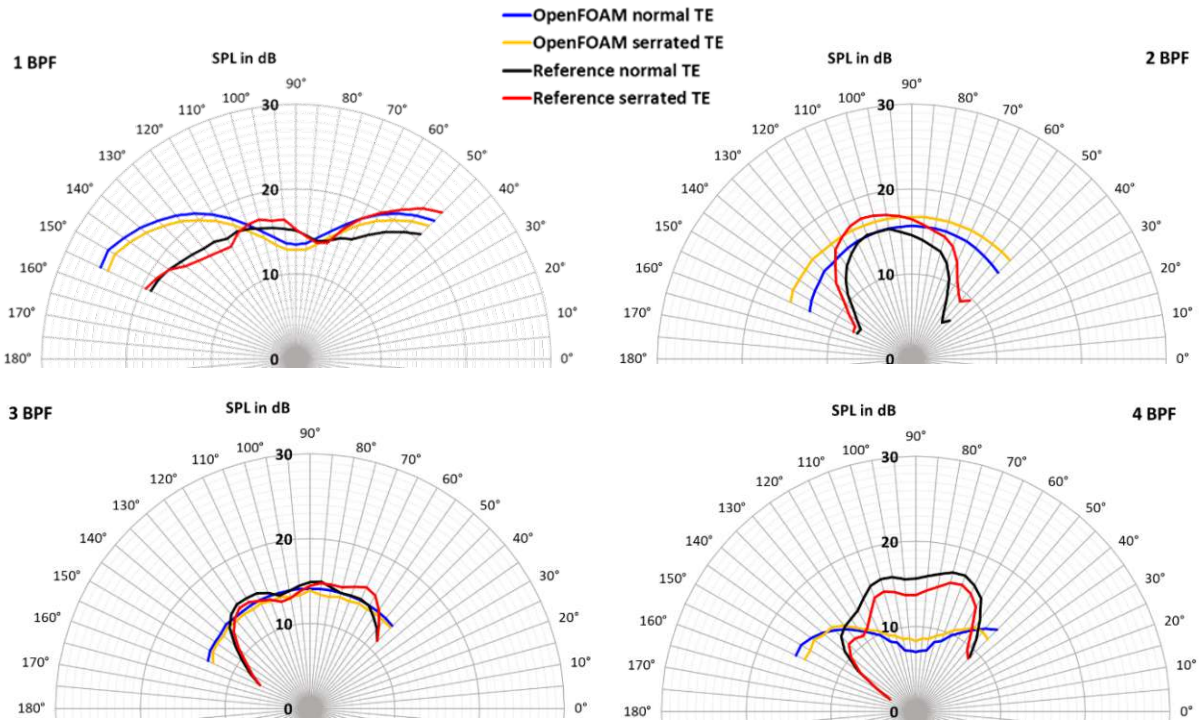

Figure 6.11: SPL directivity pattern for the first four blade passing frequencies, shown for normal and serrated trailing edges of reference experiments and OpenFOAM simulations [35]

6.3 Validation case 3

The third validation case aims to show the influence of a propeller tip modification as well as the ability of this simulation model to deal with larger diameters. The reference master thesis [12] was published in 2019 and contains simulation data and corresponding experimental results from literature. It is very difficult to find acoustic data regarding larger drone propeller diameters which are reproduceable. Initially a swept back tip would have been preferred to validate, but at this point there were no data available in literature.

6.3.1 Geometry and simulation input data

The tip modification in this validation case is a tapering of the tip starting at 75 % of the radius. The classification of the used profile is not given in the reference thesis but the shape of the root and tip cross-section. Those figures were analysed and a fitting airfoil (NACA 6407) was chosen. The profile of the tapering is given as NACA 6407, which confirms the assumptions made earlier. Key data of the propeller are summarized in table 7 [12]. The specified records for the pitch angle as well as the chord length ratio are displayed in figure 6.12.

Table 7: Overview of the characteristics of validation case 3

Diameter	0,377 m
Number of blades	2
Profile	$0 \leq {}^{r}/_{R} < 1$: NACA 6407
Angular velocity	419 rad/s (4000 RPM)
Frequency resolution	16,67 Hz

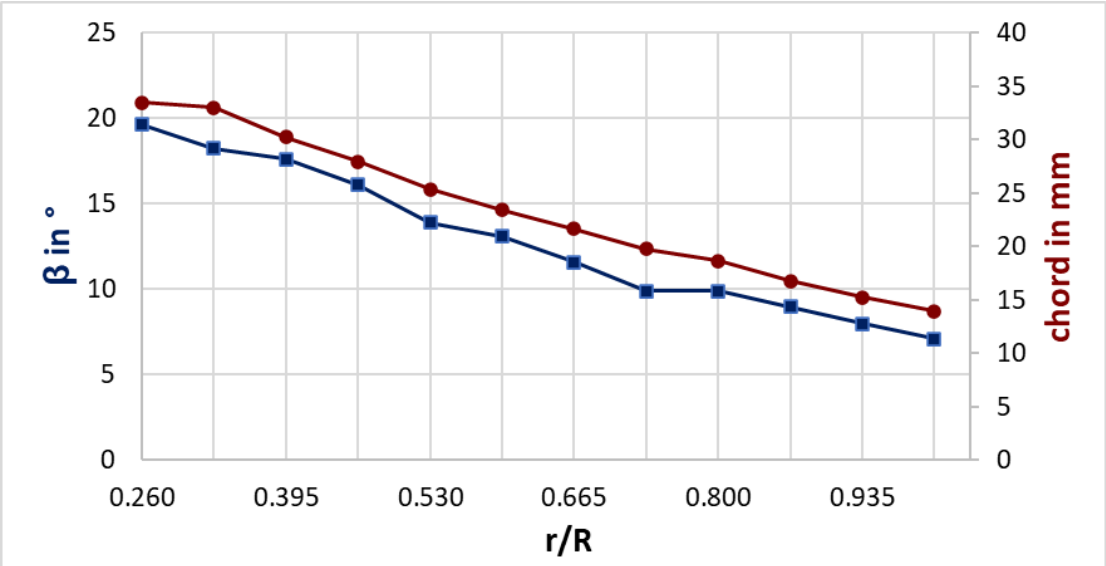

Figure 6.12: Pitch angle and chord length at multiple radial positions for validation case 3 [12]

The rotational velocity is 4000 RPM. The top and front view of the propeller geometries used in validation case 3 can be seen in figure 6.13. The hub and the connection to the hub are simplified in comparison to the source.

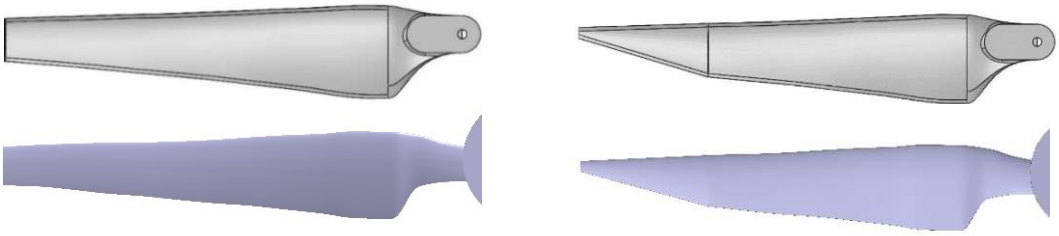

Figure 6.13: Unmodified propeller blade tip (left) and tapered blade tip (right) of validation case 3: first line shows geometry from [12], second line represents recreation in CATIA V5

In the reference thesis, nine microphones are positioned around the propeller, but the aeroacoustic data are only given at two observer positions, which can be seen in figure 6.14. The distance is the same for both receiver positions. The letter O stands for observer and the value next to it represents the observer angle θ. The rotation of the propeller is in the direction of the negative y axis. The coordinate system is rotated in relation to validation case 2.

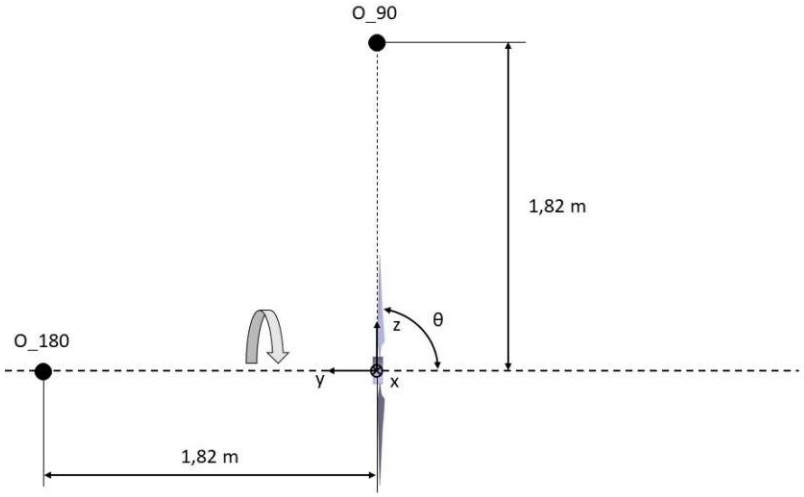

Figure 6.14: Schematic representation of the observer positions for validation case 3.

6.3.2 Aerodynamic validation

According to the reference thesis, the average thrust for the baseline propeller amounts to 7,203 N and to 6,307 N for the one with the tapered tip [12]. The tip modified propeller of the given OpenFOAM setup produces almost the thrust given by the reference with a value oscillating around 6,2 N. In opposition to that, the unmodified propeller geometry results in a thrust of about 6,8 N. Once again, the geometry, which is not completely identical, can be made responsible for this. The resulting thrust difference between the two considered geometries is about 9%.

6.3.3 Aeroacoustic validation

For the validation of the simulation model of the reference thesis, the data at the two observer angles 90° and 180° are compared with experimental data from literature (see Fig. 6.15). There are already deviations between the experimental and the simulation results of the reference thesis, especially regarding the broadband noise. However, the peaks and SPL values at the BPF of 133 Hz, demonstrate good agreement. Furthermore, the OpenFOAM results match very well with the ones obtained by the reference simulation, only the larger deviations at higher frequency values are the exception.

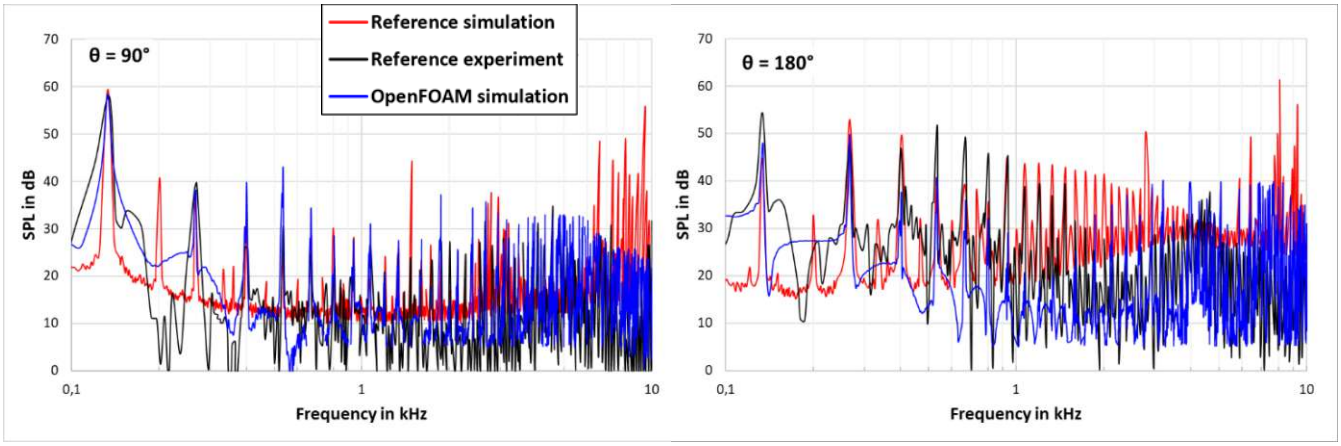

Figure 6.15: SPL plotted over frequency for observer at θ = 90° (left) and θ = 180° (right) for OpenFOAM simulation and reference experiment as well as simulation

The results of the tip modification cases are only given at the third octave band frequency values and with an applied A rating, therefore the OpenFOAM simulation results need to be adjusted. The output of the reference and the OpenFOAM simulation for the unmodified and the tapered tip are shown in figure 6.16 for both observer positions. The results of the tapered tip are marked with a dashed line. The difference in SPL is due to the oscillation of values at higher frequencies which significantly affects the calculation of third octave band values. Nevertheless, the general statement of the reference that the tapered tip can reduce the SPL at specific frequencies can also be seen to a certain degree in the OpenFOAM output.

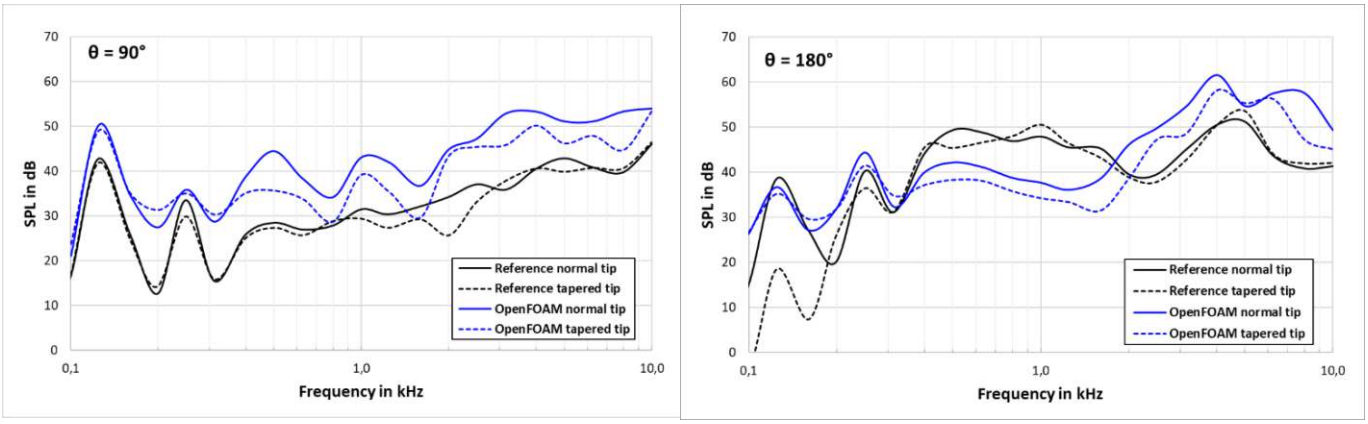

Figure 6.16: SPL plotted over frequency for an observer at θ = 90° (left) and θ = 180° (right) for OpenFOAM simulations (blue) and reference simulations (black) showing normal and tapered tip results at third octave band frequencies

7. Advanced simulations of the climb phase

Literature research has revealed that papers and articles published in the past are mainly focused on the optimisation of one feature or a single geometric modification, a combination of several adjustments has hardly been studied so far. However, combining all modifications at once will not necessarily lead directly to an optimal result. It is important to understand the influence of each feature and to apply it for the greatest benefit. In addition, very little consideration has been given to propellers that are not in the size range of small civilian drones, which can only carry a few kilograms of cargo. Since there are unfortunately no acoustic datasets for larger propeller diameters available in literature as a reference, they need to be determined first for the reference propeller.

The objective of this chapter is to adjust the reference common propeller with no specific geometrical modifications feature by feature in order to improve its aerodynamic and aeroacoustic performance. Therefore, every geometrical adaptation is added and tested individually, based on the most efficient application according to literature. Finally, the modifications are combined, and the results are presented. For the purpose of maintaining an overview, only the results of the climb case are discussed in this chapter. Hovering and descending are described in chapter 8, but not for each individual feature, only for the combined case in comparison to the reference propeller.

7.1 Reference propeller APC 27x13E

The APC 27x13E propeller from the company Advanced Precision Composites (APC) Propellers, which is commercially available, is selected as the reference propeller to be optimised. In this subchapter, at first the geometry and performance data of the reference propeller are described in detail. This is followed by a mesh study performed under the same boundary conditions which are used for all further simulations. Before the geometry is modified, the aerodynamic and aeroacoustic results of the reference APC 27x13E propeller at the defined observer locations are displayed.

7.1.1 Model geometry and performance data

As already stated in the designation of the propeller, it has a diameter of 27 inch and a pitch value of 13 inch. The additional letter E indicates the type of propeller, in this case it stands for electric, which gives information on the intended propulsion system it should be used with. The most important geometrical data and utilization limitations are summarized in table 8 [52].

Table 8: Overview of the characteristics of the APC 27x13E propeller

Diameter	0,685 m
Number of blades	2
Profile	$0 \leq {}^{r}/_{R} < 0{,}26$: NACA 4430 $0{,}26 \leq {}^{r}/_{R} < 0{,}57$: E63 $0{,}57 \leq {}^{r}/_{R} < 1$: NACA 4412
Rotational velocity	1000 - 9000 RPM

The airfoils installed are not changed abruptly at the indicated radial positions, instead there are interpolation zones, meaning that the profile is fully developed at the starting radial position and completely transformed at the end of the indicated radial ratio. The NACA 4430 airfoil is not part of official geometry dataset provided by [52] but is used to simplify the blade to hub transition algorithm. The hub diameter amounts to 0,0445 m. The comparison of the real APC 27x13E propeller and the one recreated in CATIA based on the available data by [52] can be seen in figure 7.1.

Figure 7.1: APC 27x13E in reality (left) and reengineered propeller in CATIA [52] (modified)

The variation of the pitch angle and the chord length depending on the radial position at the blade is displayed in figure 7.2. In particular, more data points are provided at the inner and outer ends of the given geometry section. The corresponding data from the hub to the boundary of the given data at 25 % radial position are assumed according to the template. The propeller configuration investigated in this chapter is smaller than some of the presented ones in the introduction chapter but still in a size that allows conclusions to be drawn for larger models, whereby direct scaling of the output is not permitted.

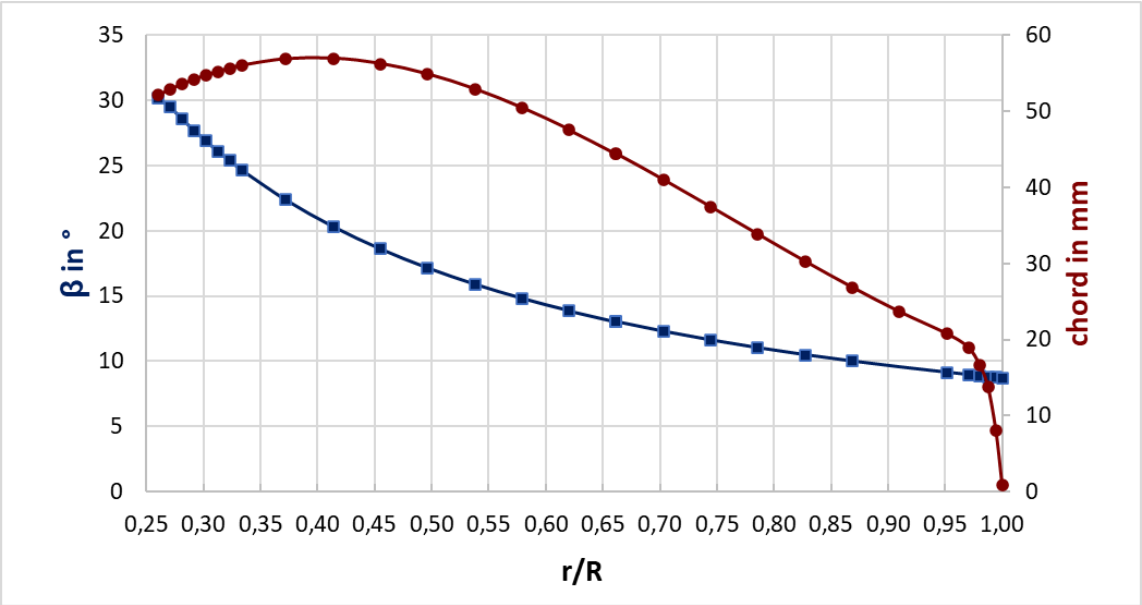

Figure 7.2: Pitch angle and chord length at multiple radial positions of the reference propeller APC 27x13E [52]

APC does not only provide the geometry data of its propellers, they also publish the computational performance results. The propeller efficiency plotted over the advance ratio for the reference propeller is given in figure 7.3. It is clearly visible that at higher inflow velocities and correspondingly higher advance ratios the propeller efficiency increases. The peak for all rotational velocities is reached at advance ratios of about 0,45 – 0,5. In addition, the highest η_P value of 0,77 is obtained at 7000 RPM for an advance ratio of 0,48 [52]. Since the difference of the efficiency values for 5000 RPM and 7000 RPM is very small, the rotational velocity of 5000 RPM is selected as the initial operating mode. Other RPM values are simulated in chapter 9 in the parameter study.

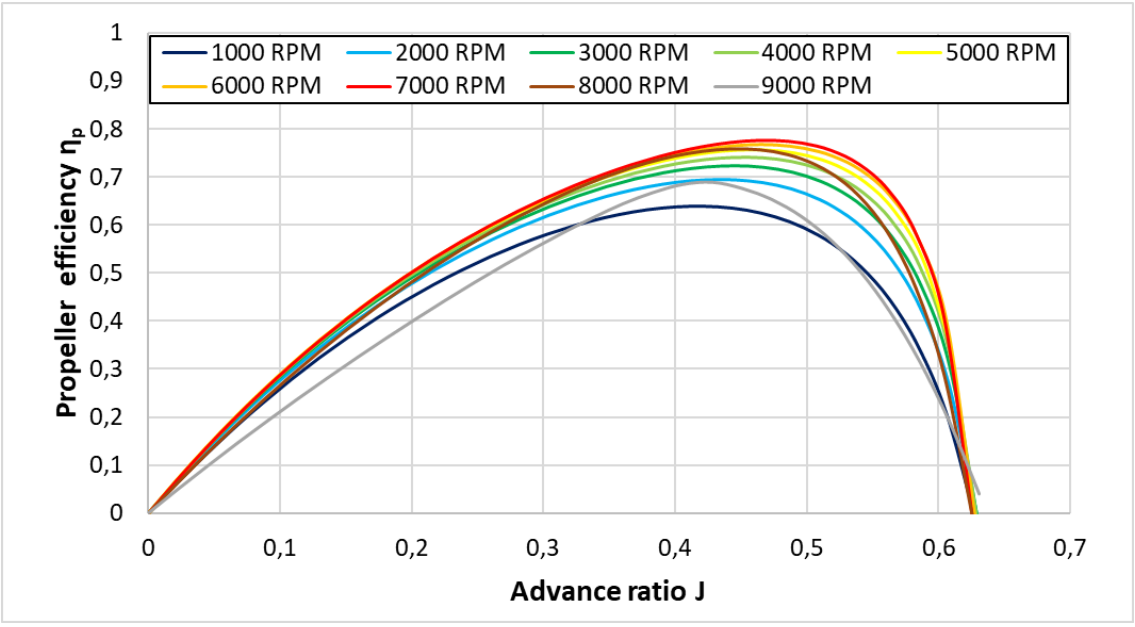

Figure 7.3: Propeller efficiency η_p plotted against the advance ratio for several rotational velocities [52]

In all three validation cases the inflow velocity is set to zero, therefore, the advance ratio and propeller efficiency can be neglected. For the optimisation of the propeller in terms of aerodynamics, an ideal correlation between those parameters must be found. The design case first needs to be specified clearly. The propeller driven air vehicle operates in different modes during take-off, climb, descent and landing, which differ mainly in the generation of thrust and in the rotational velocity. First, maximum thrust must be generated for a short period of time so that the aircraft lifts off the ground. Then this thrust is slowly reduced until a value is reached that ensures a constant climb. These phases also apply analogously to the landing process in the opposite sequence. In this thesis, only the phases with constant thrust are analysed, namely climb, hovering and descent flight. This means that an ideal propeller efficiency is available for these segments. The calculated thrust and mechanical power by [52] as a function of the advance ratio at the predefined operating mode of 5000 RPM are plotted in figure 7.4.

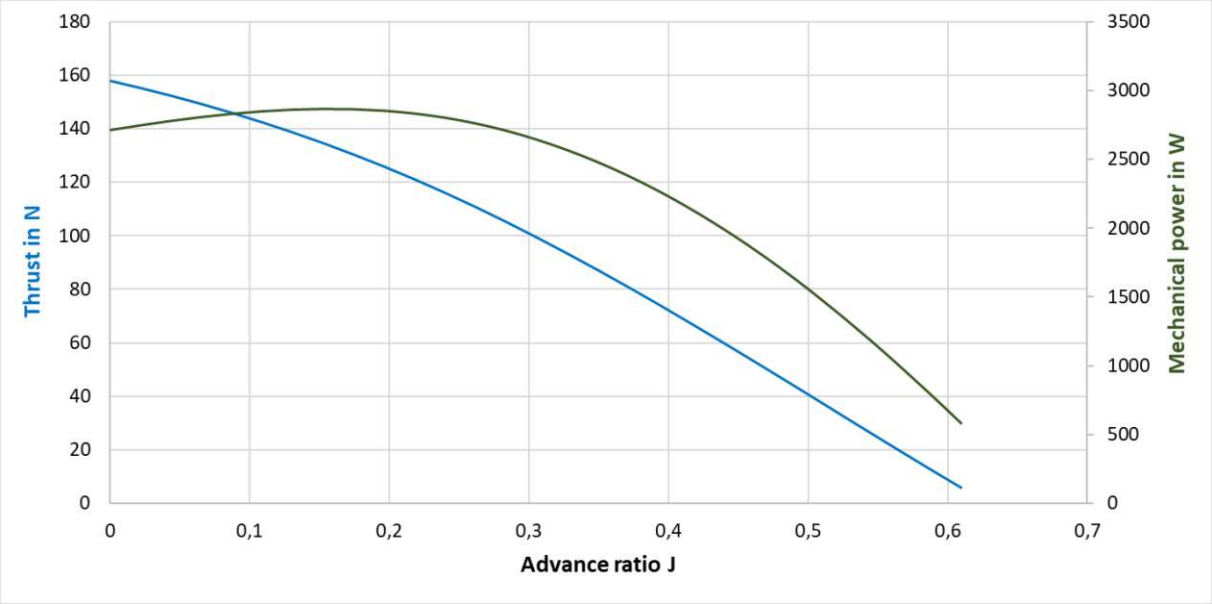

Figure 7.4: Thrust (blue) and mechanical power (green) plotted against advance ratio for a rotational velocity of 5000 RPM [52]

Analysing figures 7.3 and 7.4 indicates that an advance ratio of 0,3 provides a good balance between propeller efficiency (η_P = 0,655) and thrust (T = 100N) for the climb case. The inflow velocity calculated according to equation 3.1 results in 17,13 m/s, which exceeds the feasibility of an application in an urban area. Therefore, a much lower advance ratio of 0,1 is chosen, which corresponds to a propeller efficiency of 0,29, an inflow velocity of 5,75 m/s and a generated thrust of 143,8 N. On the other hand, for the hovering flight case the propeller efficiency is zero and the generated thrust amounts to 157,85 N for the same advance ratio.

As the data given by [52] are only calculated for positive advance ratios, there is no reference available for the negative inflow velocity of the descent case. Nevertheless, the same intake velocity in the opposite direction is considered for descending, which results in an advance ratio of -0,1. For negative advance ratios, the thrust and torque values are difficult to predict. Furthermore, certain effects need to be avoided, such as the recirculation of the generated flows of the propeller´s own wake region, because this can cause unintended steep descent and thus affect the safety of the flight operation. This so-called ring state can be prevented by choosing small rates of descent. It must also be noted at this point that unlike helicopters, which can control the generated thrust by collective pitch control, for air vehicles with this size and number of propellers, the thrust can only be changed by adjusting the rotational velocity. It is important to mention that the different phases of vertical flight are simulated for the same rotational velocity, only the advance ratio is changed. However, it also must be noted that a single payload as a design case is intentionally not selected for the various flight phases, so that a simpler study of various RPM values is possible. Thus, a variation of the thrust can be avoided, and a consistent comparability can be achieved.

7.1.2 Mesh quality study

In order to obtain a good result quality, a mesh quality study is performed. To do so, the initial APC 27x13E reference propeller is selected as the simulation study geometry. The advance ratio is set to 0,1 which leads to a generated thrust of 143,8 N and a mechanical power of 2850 W, according to [52]. These values of the climb case serve as comparative data for the different mesh sizes. As already stated in chapter 4.3 and equation 4.1, the Courant number increases if the mesh size decreases. For the given constant inflow velocity, this means that only a reduction of the timestep size can lead to a subsequent decrease of the Courant number if the mesh gets finer. Therefore, not only the number of cells of each mesh quality are shown in table 9, additionally the step size and step simulation time are given for comparison.

Table 9: Overview of the characteristics of each mesh category in the mesh quality study

Mesh quality	Number of cells	Step size	Step run time
Coarse	$9{,}38 \cdot 10^5$	$1 \cdot 10^{-6}$ s	1,1 s
Normal	$1{,}93 \cdot 10^6$	$1 \cdot 10^{-6}$ s	2,7 s
High	$3{,}32 \cdot 10^6$	$1 \cdot 10^{-7}$ s	4,1 s
Medium	$3{,}79 \cdot 10^6$	$1 \cdot 10^{-6}$ s	10 s

The first three entries in the table above differ in the number of blocks that are created along the axes in the “blockMesh” file, on which the refinement is based. This guarantees a uniform reduction of the mesh size. In the case of “Medium” mesh quality, on the other hand, one refinement level is increased locally. In this case that refers to the cylinder in the wake area of the propeller, which is why the number of cells increases significantly, but the step size is kept constant compared to the "Normal" mesh quality model, on which it is based.

The different mesh qualities are compared regarding the generated thrust over time, which can be seen in figure 7.5. Except for the coarse mesh, all simulations oscillate around a thrust value of approximately 133 N. The difference of about 10 N to the reference value can be explained by the limited information on the geometry connecting the propeller blades and the hub. Furthermore, no data are available about the detailed boundary conditions of the manufacturer's simulations. A small deviation from the reference value can also be noticed in the required mechanical power (see figure 7.6). Oscillation for the “Normal” mesh case occurs around a value of about 3000 W, so the difference here is approximately 150 W.

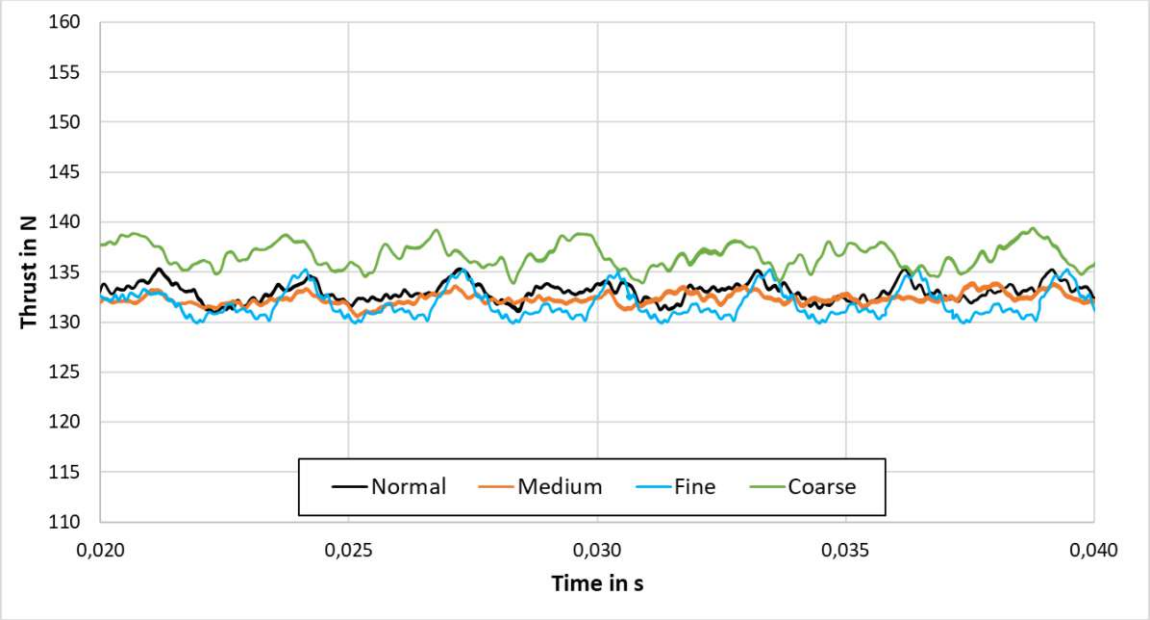

Figure 7.5: Generated thrust by the propeller of the reference case for different mesh sizes

To avoid the initial fluctuations of the parameters, the graphs start with a time offset. Furthermore, the time span is also limited, because simulation times for such short time periods have already become very large, especially for the “Fine” mesh quality. As shown in Figure 7.5 and 7.6, once a certain mesh size is reached, the deviation to simulations with more cells is reduced. Considering the time step size and step time as well as the results of the mesh quality study, the “Normal” mesh quality (represented by a black line in both figures) was classified as sufficiently accurate and is used in all the following simulations. In addition, the reproduction of the individual geometric modifications is sufficient with the selected mesh size.

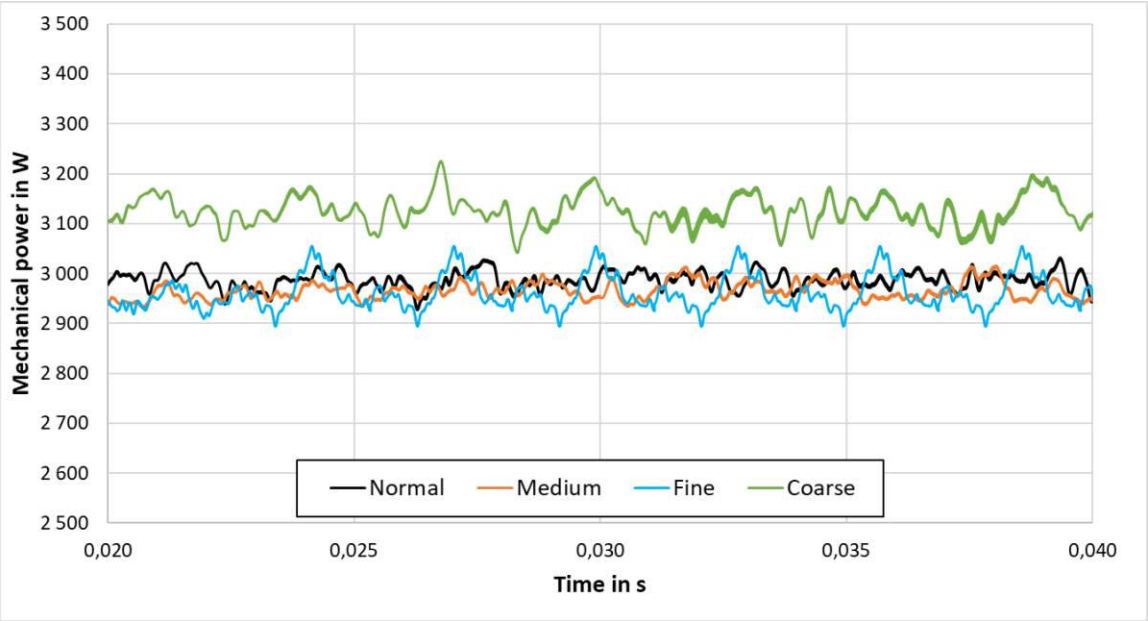

Figure 7.6: Mechanical power required by the propeller of the reference case for different mesh sizes

7.1.3 Aerodynamic results

As already mentioned in the introduction of this chapter, the following results only represent the climbing case. Starting with the aerodynamic results, figure 7.7 shows the velocity distribution in the yz plane at a timestep of 0,15 seconds. The wake flow field is similar to comparable simulations from literature and corresponds to the expected results. The blade tip velocity resembles a Mach number of 0,52 for the given boundary conditions. The expected increase of Mach number towards the tip is displayed in figure 7.8.

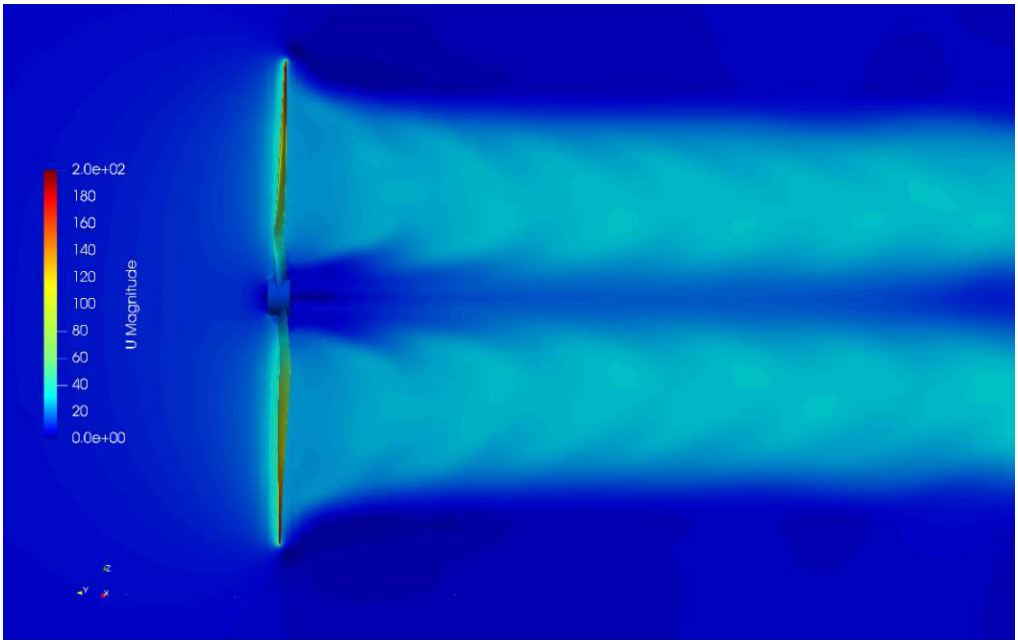

Figure 7.7: Velocity distribution (in m/s) of the propeller and its wake region at 0,15 s for a freestream velocity of 5,75 m/s at 5000 RPM

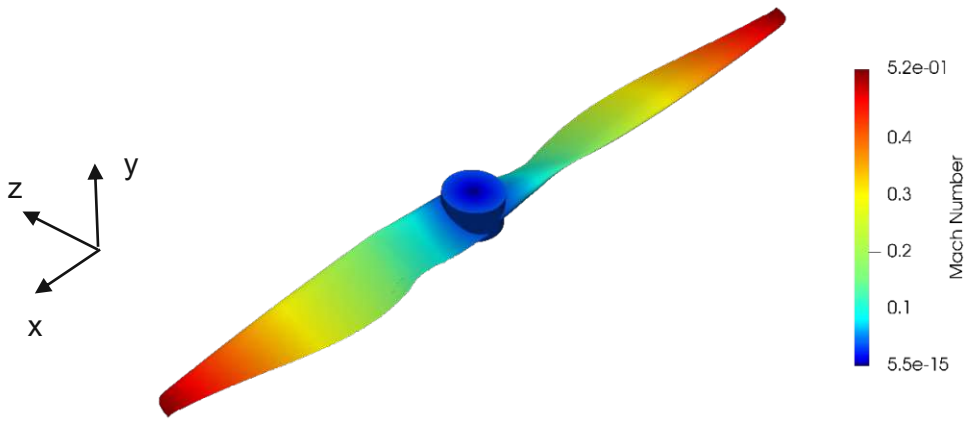

Figure 7.8: Mach number distribution on the surface of the reference propeller

According to equation 3.2, the propulsive efficiency η_p of the recreated propeller amounts to 25,92% which is in agreement with the literature data displayed in figure 7.3 [52]. The generated thrust as well as the required mechanical power are already shown in figure 7.5 and 7.6 as black lines. Nevertheless, it is also important to display the distribution of the thrust coefficient c_T and the lift coefficient c_l over the blade span. For this purpose, the thrust values of the reference geometry are determined at several radial positions at 5000 RPM. By using equation 6.1, the thrust coefficients can thus be calculated. Regarding the lift coefficient c_l, the standard equation found in literature is applied [32]. The results are summarized in figure 7.9.

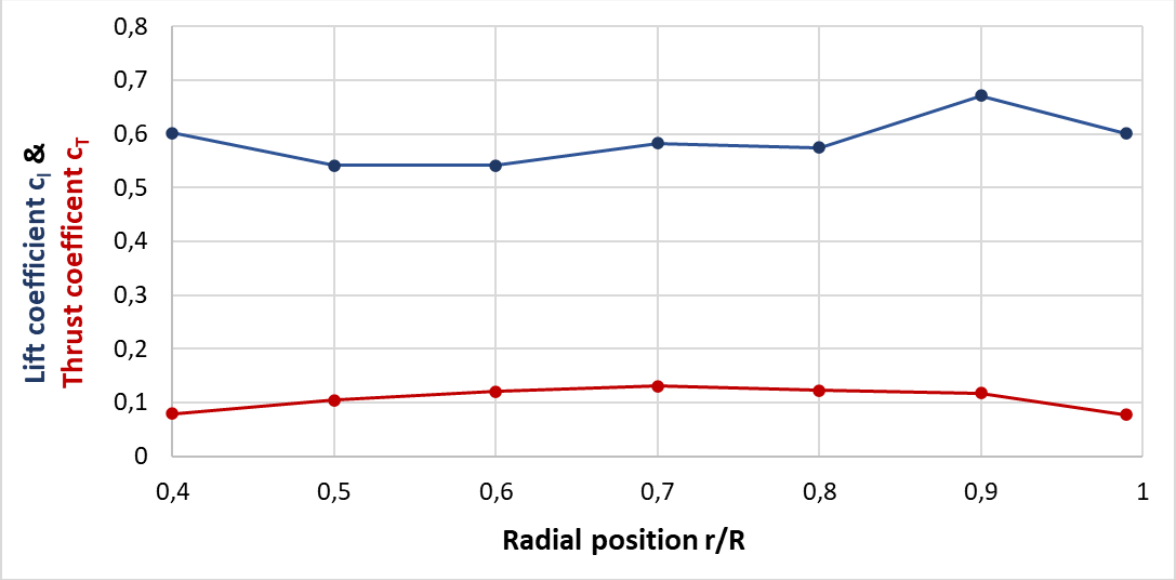

Figure 7.9: Thrust coefficients c_T and lift coefficients c_l plotted at several radial positions of the propeller blade

The thrust and accordingly also the thrust coefficients increase towards the tip, however, a reduction can again be seen near the blade tip. This behaviour is analogous to that described in literature for thrust coefficients of propellers. The lift coefficient fluctuates around a value of 0,6. The maximum lift coefficient values of the sectionally applied airfoils (NACA 4412 and

E63) are not exceeded. The data were determined for all radial positions according to the corresponding Reynolds and Mach numbers and all resulted in a value around 1,37. Accordingly, it can be assumed that the applied RANS turbulence model meets the requirements and no laminar flow separation occurs. However, a hybrid approach of RANS and LES could further improve the accuracy of the results, but this would also imply an increased computational effort.

The vorticity distribution of the propeller is displayed in figure 7.10. Due to the early time step, there are still signs of the start vortices in the lower section of the figure visible. In general, vorticity describes the tendency of a fluid element to self-rotate around an axis, in this case the rotational axis, from which a circulation in a closed area results. Accordingly, the values in the area near the propeller are higher and the circulations in the wake area also differ from the surrounding region. The display options in Paraview are limited, which is why a wireframe representation has been chosen for better visibility of the vortices.

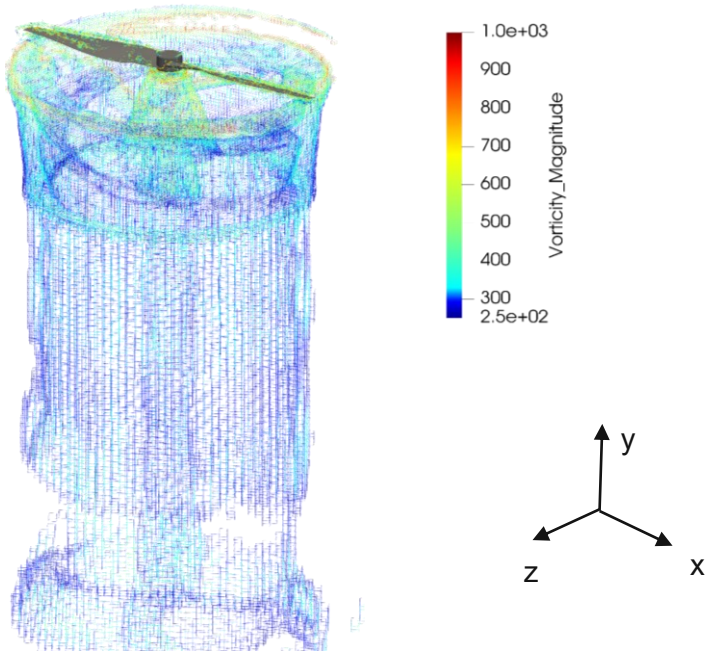

Figure 7.10: Filtered vorticity distribution (in 1/s) of the propeller and its wake region at 0,15 s for a freestream velocity of 5,75 m/s at 5000 RPM

7.1.4 Aeroacoustic results

For the advanced simulations, observer microphones are positioned at every 5° in the propeller plane (see Fig. 7.11 blue circle) and transverse to it (see Fig. 7.11 red circle) at a distance of 5 meters to the center of rotation, which corresponds to far field measurements. As the results in the space behind the propeller are influenced by its wake, no receiver points are installed there because of reducing accuracies due to the chosen FHW control surface set-up, as already explained in chapter 4.2. All the observer locations are shown in figure 7.11, represented by small black dots at the perimeter of each circle.

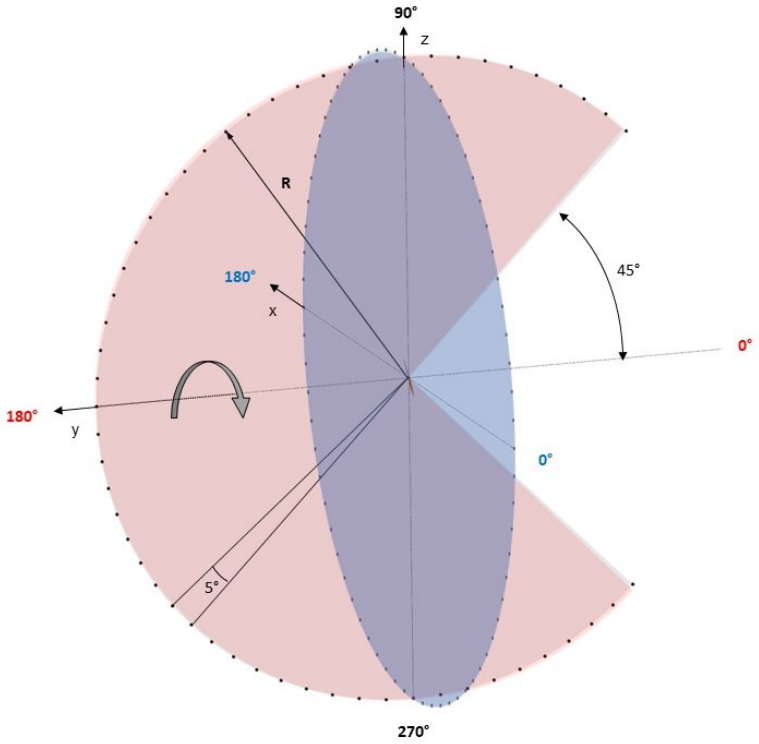

Figure 7.11: Observer positions (black dots) for the advanced simulations in the xz (blue) and yz plane (red)

In order to obtain acoustic results with the desired frequency resolution, especially for such small time steps, it is important to increase the simulation time. Due to the limitation of the simulation time by VSC to 72 hours, it was decided to set the frequency resolution to 10 Hz. As mentioned in the fundamentals chapter, a reduction of this value to 5 Hz would consume twice as much time as the current version. Another important consideration that led to this selection is the fact that due to the external implementation of the acoustic library, it is not possible to restart the acoustic analysis, it can only start again from the onset point. For a controlled SPL output, an external FFT is carried out, which allows for very accurate frequency results. The comprehensibility and the inclusion of the Nyquist criterion are thus improved. The acoustic output of the reference propeller for the climb phase at a rotational velocity of 5000 RPM is displayed in figure 7.12 at an observer position of 90° in the rotational plane.

Since a comparison of the data is complicated at higher frequencies due to the large number of values and the logarithmic representation, the results of the 1/12 octave bands are also plotted, starting from 1000 Hz. These are higher than the simulation results due to the sum of the logarithms of the individual SPL data points in a defined frequency range. However, these data sets are for comparison purposes only and should not be considered as direct SPL output. The original results are still displayed transparently for frequencies above 1000 Hz.

The resulting BPF amounts to 166,7 Hz according to equation 2.14 and is especially pronounced at the first three harmonics. At frequencies higher than 1000 Hz, the SPL values oscillate between 20 dB and 50 dB. The reason for the SPL hump at 5000 Hz is unknown. The acoustic outputs of other observer positions are only presented in the context of the directivity plots, otherwise this chapter no longer provides a clear overview. The colour black represents the reference propeller in all subsequent SPL frequency plots.

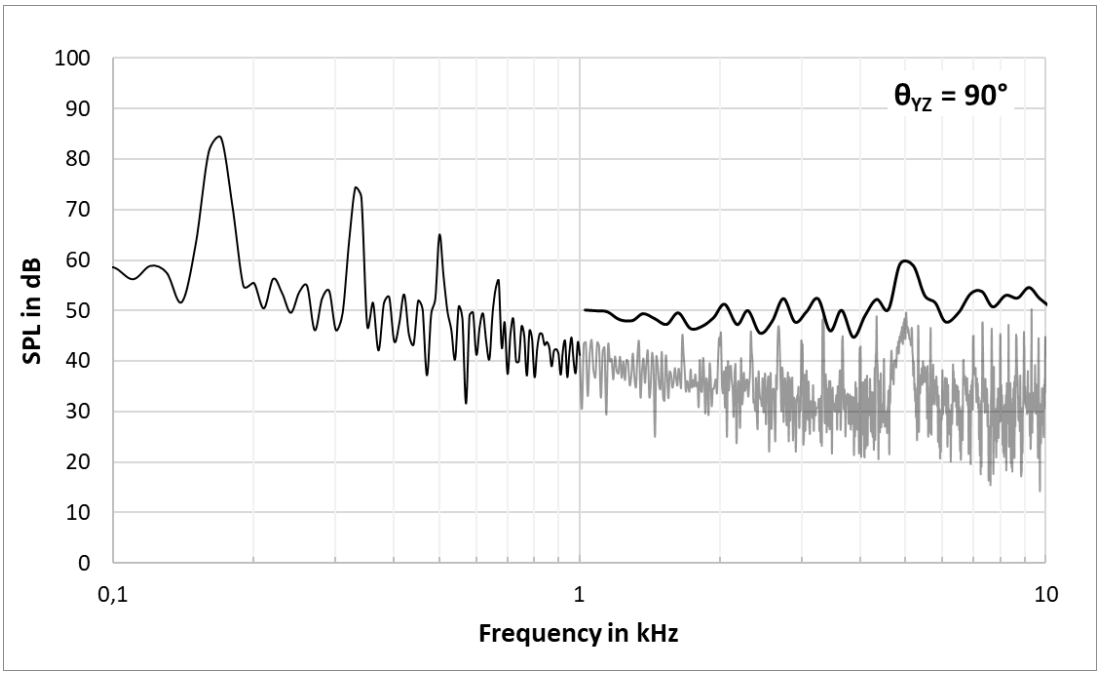

Figure 7.12: SPL plotted over frequency for an observer at θ = 90° for the reference propeller with additional 1/12 octave band SPL output starting at 1000 Hz

Figure 7.13 displays the directivity plots for both observer planes for the first three blade passing frequencies and the OASPL value of the reference case. Due to the inaccuracy in the wake region, the measurements in the yz plane are limited from 45° to 315°. For the yz plane, a reduction of the SPL output directly in front of the propeller is visible. At 180°, however, there is a local peak that can be associated with the dipole character of the loading noise. This local peak is also visible in the OASPL output which otherwise shows relatively constant results for all observer angles. In the xz plane, the monopole source of the thickness noise dominates for all BPFs and the OASPL output.

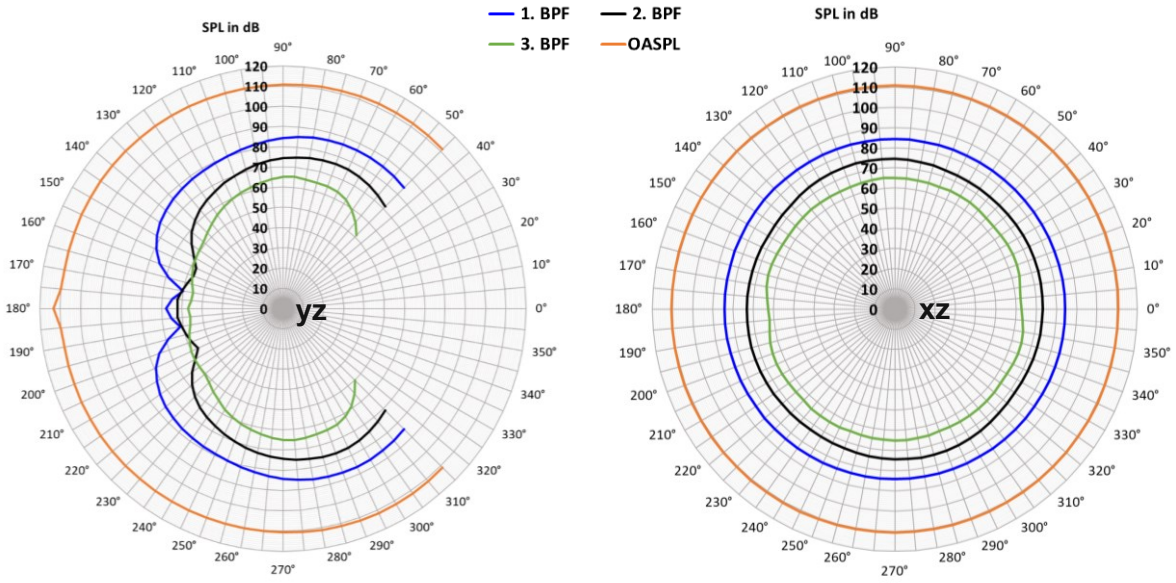

Figure 7.13: Directivity plots of the yz plane (left) and the xz plane (right) for the first three BPFs of the reference propeller as well as the OASPL values at all defined observer positions

7.2 Individual geometrical modifications

The geometrical modifications that are first individually tested in this section are leading edge tubercles, trailing edge serrations and several blade tip modifications as listed in table 10. Knowing the individual effects are helpful to better interpret the impact of the effects of the combined features later on. In addition, geometry modifications of propellers of this size have not been aeroacoustically studied in the available literature so far. Some of the listed features have been validated in chapter 6 at a smaller scale, conditional on availability of reference literature and data. Furthermore, these modifications are concluded as reasonable in this field of application by literature research. This refers to the size, number, position and type of the named modifications.

Table 10: Overview of the individual geometrical modifications and the radial application range

Case	Modification	Application radial position
1	Leading edge tubercles	0,75 < *r/R* < 0,95
2	Trailing edge serration	0,35 < *r/R* < 0,95
3	Blade tip modification	0,95 < *r/R* < 1

It is important to mention that the fundamental shape of the APC 27x13E propeller is not changed by the geometric adjustments, therefore the diameter, the number of blades, the airfoils used and the pitch remain the same. Only local changes to the chord length and airfoil positioning are introduced. In addition, the freestream velocity is fixed, and the thrust must

remain constant, since this is the criterion for comparing the models. One way to control the generated thrust is to adjust the rotational velocity. The listed cases 1 - 3 are described in detail in the following subchapters. Table 11 compares the number of cells and time step sizes of these modifications. The smaller time difference between each step of the simulation for the case with the trailing edge serration applied derives from the detailed geometry of each serration which also leads to slightly more cells than in the other cases.

Table 11: Overview of the number of cells and the step size of the individual geometrical modification simulation cases

Modification	Number of cells	Time step size
Leading edge tubercles	$1{,}926 \cdot 10^6$	$1 \cdot 10^{-6}$ s
Trailing edge serration	$1{,}942 \cdot 10^6$	$8 \cdot 10^{-7}$ s
Blade tip modification	$1{,}932 \cdot 10^6$	$1 \cdot 10^{-6}$ s

7.2.1 Case 1: Leading edge tubercles

Since the tubercles are the only geometrical modification that is not part of the validation, the effect could not yet be demonstrated within the framework of this thesis. Simulations by [45] prove that tubercles close to the tip section have the best noise reduction effect. Therefore, the geometry of the leading edge is changed between 75% and 95% of the radial position. Furthermore, the results from this study indicate that a constant wavelength λ of the tubercles has a bigger positive influence than a constant amplitude A of the tubercle shape. The wavelength λ is set to 20% of the maximum chord length of the propeller blade, which corresponds to a value of 11,4 mm. In addition, the corresponding amplitude values are defined as 10% of the local chord length $\bar{c}$. Accordingly, the tubercles appear smaller closer to the tip. The reference propeller with added tubercles can be seen in figure 7.14.

Figure 7.14: Case 1 with leading edge tubercles created in CATIA V5

Due to the reduction of the surface area in this section, the generated thrust decreases slightly. This thrust deficit can be compensated by local increases in chord length or an increase in rotational velocity. As the difference of the time averaged thrust value is very small, about 0,2 N, which is plotted in figure 7.15, and since oscillation occurs approximately at the same nominal value, any changes have been omitted. The increase of the mechanical power due to the modification of the leading edge amounts to about 1%. The course of the curve of the graph is similar to the one of the thrust.

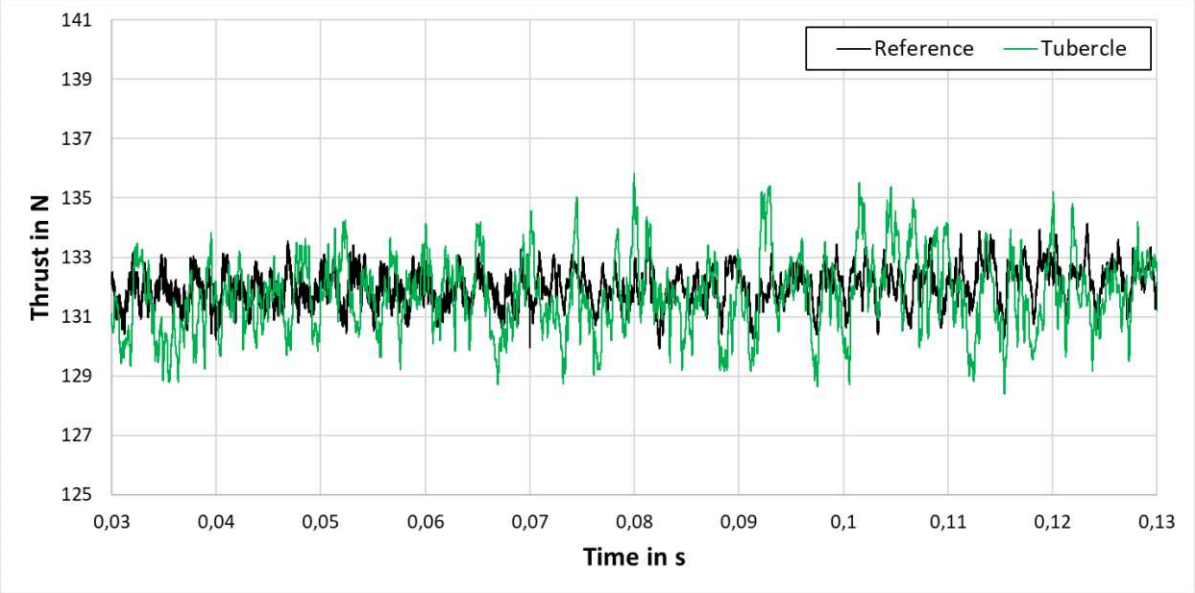

Figure 7.15: Comparison of the generated thrust by the propeller of the reference case and the one with tubercles

The comparison of the kinematic pressure distribution, which is used for calculation in OpenFOAM, on the upper surface of the propeller blade between the reference geometry and case 1 is shown in Figure 7.16. The tubercles cause lower pressure values at the leading edge to occur further inwards. The change in the pressure distribution of the trailing edge is minimal and can be neglected. In contrast, no differences are noticeable with regard to the velocity distribution or the maximum tip Mach number. This is likely to be related to the fact that the leading edge has been modified only locally.

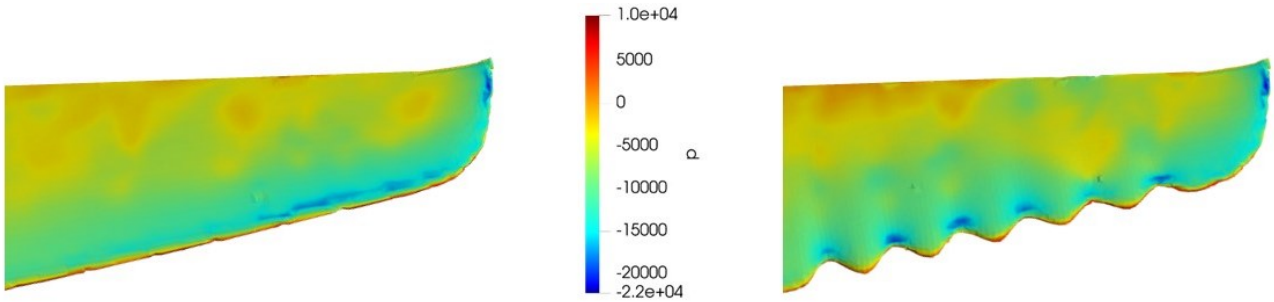

Figure 7.16: Kinematic pressure distribution (in m^2/s^2) on the upper surface of the reference propeller (left) and the propeller with applied tubercles (right)

In terms of the acoustic results, there are some differences in the frequency spectrum between the APC propeller and the modified one at the observer position $\theta_{YZ} = 90°$ (see figure 7.17). The SPL output between the tonal noise peaks, which is associated with narrow band random noise, is lower than the one of the reference geometry. Furthermore, the local peak at 5000 Hz does not appear in the results of the propeller with applied tubercles. The sporadic tonal peaks in the broadband noise range cannot be avoided due to the large number of data but they are neglectable. The 1/12 octave band results in figure 7.17 indicate local SPL reductions of up to 5 dB especially between 1000 Hz and 2000 Hz, with the exception of the deviation at 5000 HZ. In the frequency range of the broadband noise, there are further reductions visible.

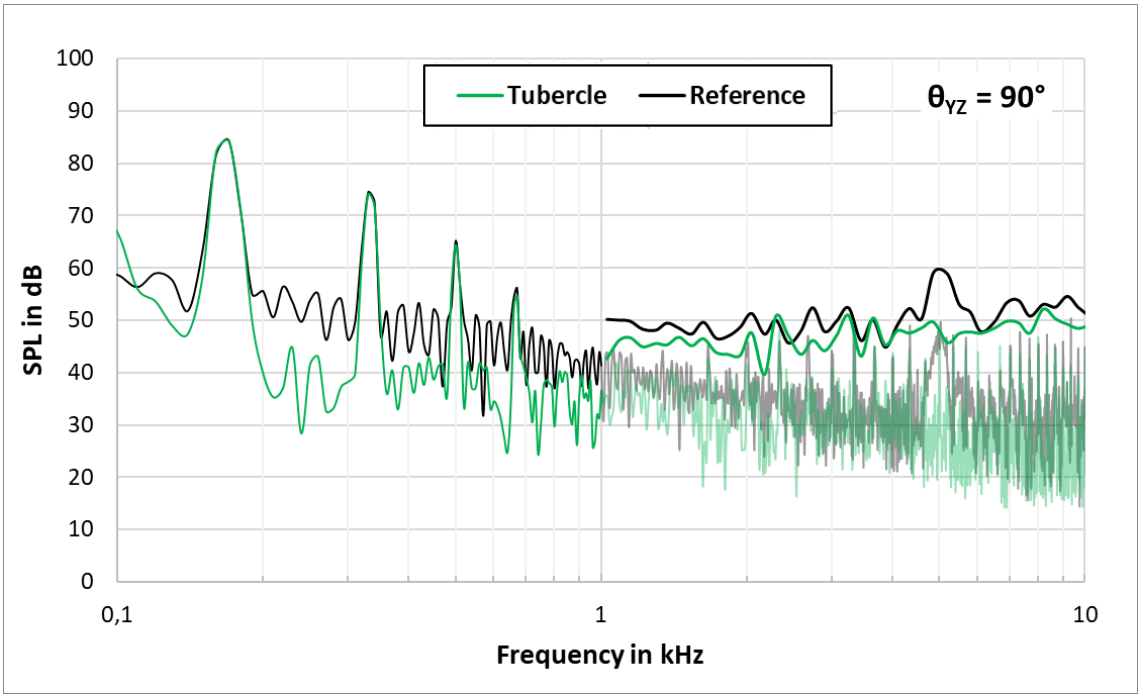

Figure 7.17: SPL plotted over frequency for an observer at θ = 90° for the reference propeller and the propeller with leading edge tubercles with additional 1/12 octave band SPL output starting at 1000 Hz

As mentioned by [45], there is a difference in the directivity pattern of the generated noise in the yz plane, which is shown in figure 7.18. Especially in front of the propeller between 135° and 225°, an almost constant SPL distribution for the modified propeller is visible for all three displayed blade passing frequencies. In comparison to the output of the reference propeller, which is visualised with dashed lines, this leads to locally higher SPL values for all BPFs. The reason for this is assumed to be the greater level of loading noise. Responsible for this are the pressure values, which are higher in magnitude and located radially further inwards, which contributes to a local amplification effect of the dipole source. The OASPL distribution in the yz plane indicates a minor reduction of the SPL output in front of the propeller of about 2 dB. On the other hand, the differences to the reference propeller in the xz plane are very small for all BPFs and the OASPL values.

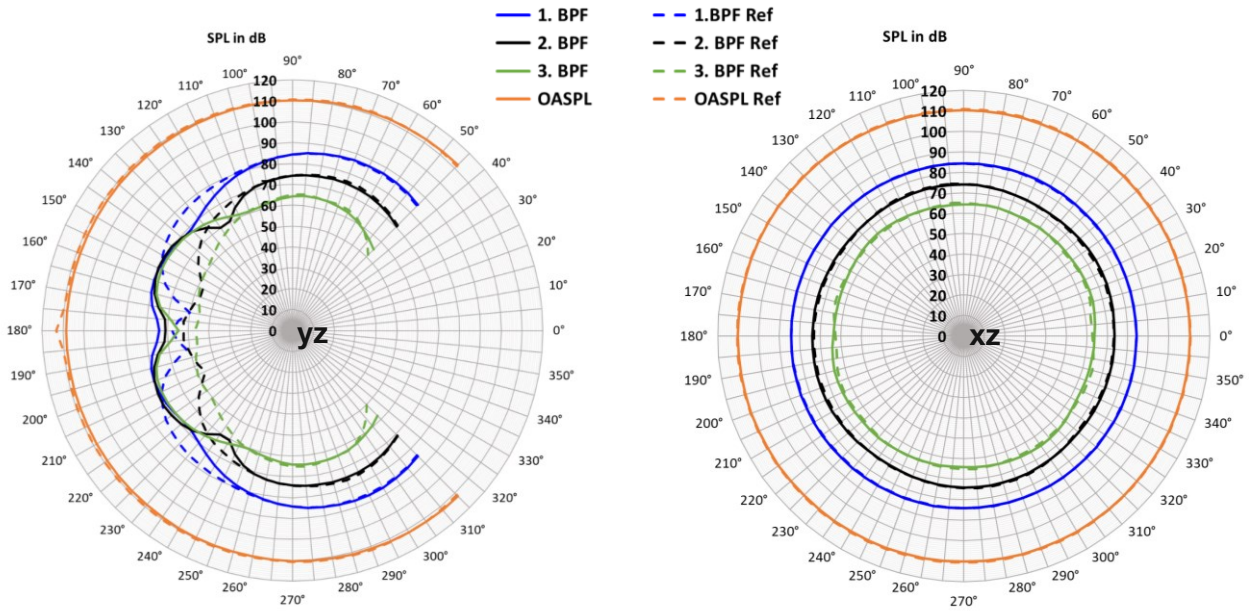

Figure 7.18: Directivity plots of the yz plane (left) and the xz plane (right) for the first three BPFs as well as the OASPL values at all defined observer positions of the reference propeller (dashed lines) and the one with applied tubercles

7.2.2 Case 2: Trailing edge serration

The literature research of chapter 3 concluded that a sawtooth serration with small spacings between the single serrations leads to the best aeroacoustic output. Furthermore, the ratio between wavelength λ and amplitude h should not be too small, which means that less serration is more effective. Nevertheless, according to [42] a good ratio is reached when the amplitude value is about twice as high the wavelength. Moreover, the noise reduction effect is greatest when only the exterior section up to an inner radial position of approximately 40% is serrated [41]. Considering the fact that there is already a minor reduction of the generated thrust due to the implementation of the tubercles, an addition of serrations is more appropriate than a further reduction of the surface area that can generate thrust. The ratio of the wavelength to the amplitude $\lambda/_h$ is selected as 0,6. As stated in literature [41], the wavelength can be set as 1% of the diameter. The serrations are applied in a section between 35% and 95% of the radius. The thickness of these modifications amounts to 2 mm. The final geometry of the propeller blade with the applied trailing edge serrations recreated in CATIA is displayed in figure 7.19.

Figure 7.19: Case 2 with trailing edge sawtooth serrations created in CATIA V5

Due to the enlarged surface area, there is an increase in the generated thrust. The difference between the propellers with the same rotational speed of 5000 RPM, of which the modified one is displayed in figure 7.20 as the red line, amounts to approximately 10 N. Therefore, an additional simulation is submitted with a reduced rotational velocity of 4820 RPM to generate the same thrust as the reference propeller blade (see figure 7.20 orange line). The output of the mechanical power plotted over time looks similar to the one of the generated thrust. The serrated propeller at 5000 RPM requires 10% more power, the one operated at 4820 RPM leads to a power reduction of about 2% in comparison to the reference propeller. This shows the potential of geometric optimisation, which not only leads to acoustic improvements, but can also achieve energy reductions while maintaining the same thrust.

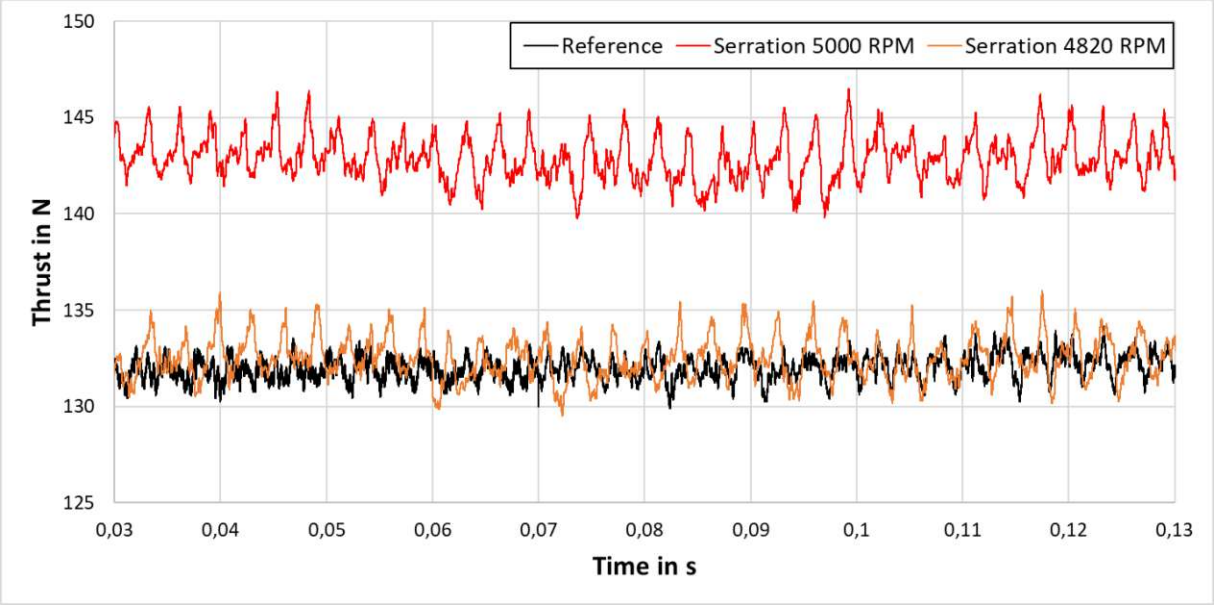

Figure 7.20: Comparison of the generated thrust by the propeller of the reference case and by the propeller with trailing edge serration at a rotational velocity of 4820 RPM (orange line) and 5000 RPM (red line)

The direct comparison of the velocity distribution at two different cross-sections in close proximity, namely one with maximum amplitude corresponding to the tip of a serration and one with minimum amplitude corresponding to the unmodified trailing edge, is displayed in figure 7.21 for a representative time step. The velocity differences are hardly visible, but it can be noted that due to the serration there is a higher velocity on the suction side of the airfoil and a slightly lower velocity on the pressure side in comparison to the trailing edge between two serrations. This behavior is also visible for other time steps.

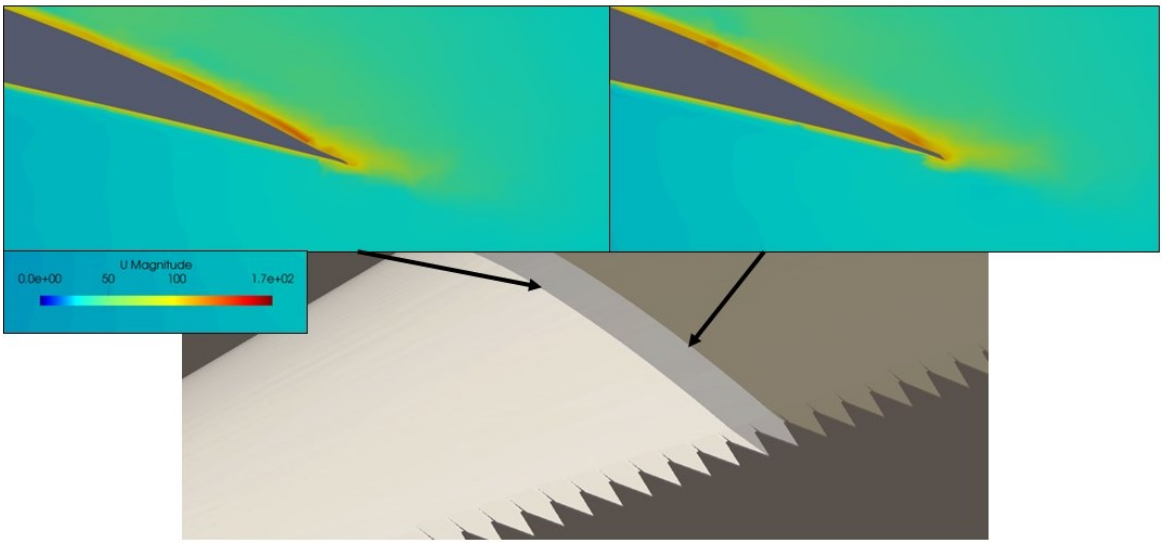

Figure 7.21: Velocity distribution (in m/s) at the minimum (right side) and maximum (left side) amplitude value of the serration

Once again, the comparison of the SPL output plotted over the frequency spectrum is displayed for an observer in the rotational plane. The simulation results of the serrated propeller at the same rotational velocity as the reference case (see Fig. 7.22 red line) already show a decrease of the narrow band random and broadband noise of up to 10 dB. However, there is no reduction of the tonal peaks at the BPF values. On the other hand, the output of the simulation with the reduced rotational velocity of 4820 RPM (see Fig. 7.22 orange line), indicates minor decibel reductions at the tonal noise peaks. Due to the change of the rotational velocity, the blade passing frequency also decreases which is the reason for the shifted peaks for this simulation output. It has to be noted that due to the chosen frequency resolution of 10 Hz, the new BPF value for the reduced rotational velocity still lies between 160 Hz and 170 Hz which is why definitive statements on the magnitudes of the peak values are still only possible to a limited extent. Both serration cases result in roughly the same broadband noise reduction. It is an objective of future work to further investigate the influence of amplitude size and wavelength of the serrations for propellers with large diameters.

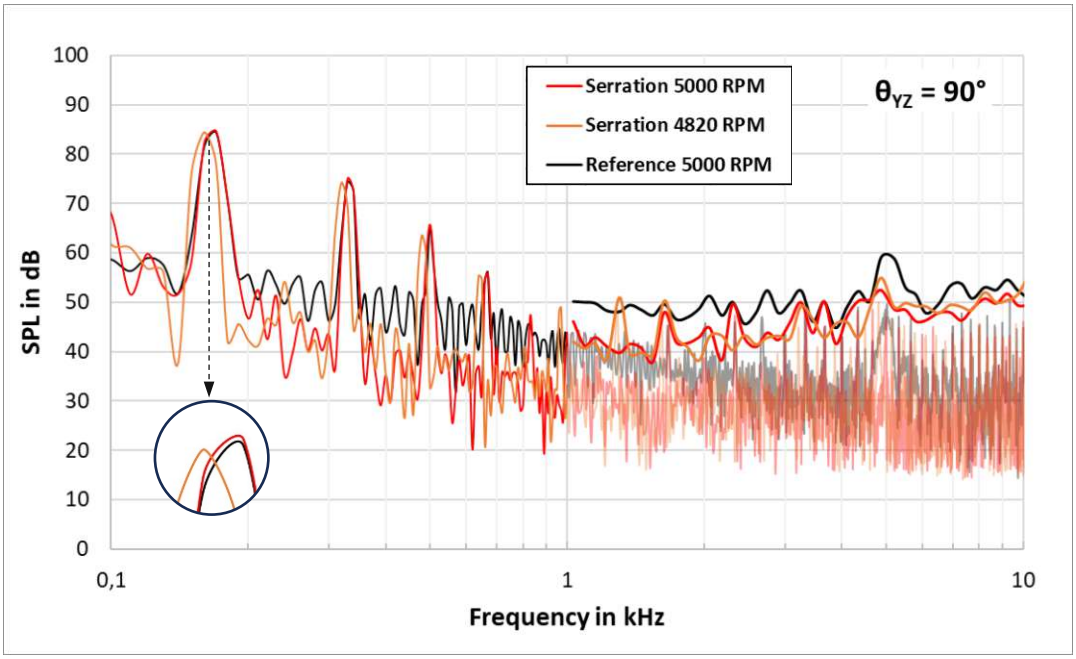

Figure 7.22: SPL plotted over frequency for observer at θ = 90° for the reference propeller and the propeller with trailing edge serration at a rotational velocity of 4820 RPM and 5000 RPM

The results in the xz plane of the directivity pattern are similar to those of the reference propeller with the exception that for the lower rotational velocity, smaller circles are displayed. The following figure 7.23 therefore only plots the directivity behaviour in the yz plane for both rotational velocities of 4820 RPM and 5000 RPM. There is hardly any change of the SPL output for both cases, however, the directivity pattern changes for the smaller RPM value. Especially in front of the propeller at 180°, there is an increase of the noise output visible for the first two BPFs. Furthermore, the OASPL values are slightly higher for the case with the reduced RPM value.

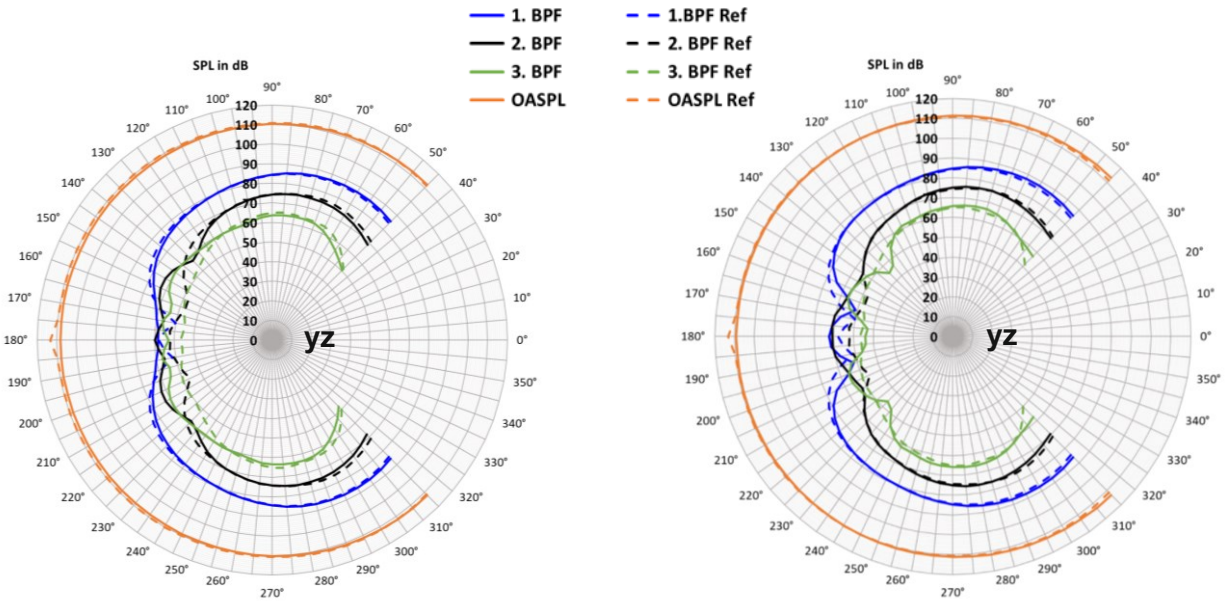

Figure 7.23: Directivity plots of the yz plane at 4820 RPM (left) and at 5000 RPM (right) for the first three BPFs and the OASPL of the propeller with a serrated trailing edge in comparison to the reference propeller at 5000 RPM (dashed lines)

7.2.3 Case 3: Tip modifications

The current tip of the reference propeller blade represents a parabolic tip which is a common concept especially for helicopters in Europe. The typical US approach is characterised by a swept tapered anhedral tip. The third major concept is the BERP (British Experimental Rotor Programme) rotor tip as well as the more recent comparable blue edge approach by Airbus. Those two were developed, among other things, to reduce the blade vortex interaction (BVI) and the corresponding generated noise during descending. According to [56], it is not possible to determine the best option, as they all have their advantages and disadvantages in terms of aerodynamic and aeroacoustic properties as well as design and manufacturing constraints.
Without changing the complete structure of the blade and in order to stick to geometrical improvements during only vertical flight phases, it was decided to change the already existing parabolic tip to a larger swept tapered anhedral tip. This modification is based on a blade tip sweep angle $\Lambda_{\mathrm{Tip}} = 46°$ and an anhedral angle $\Gamma_{\mathrm{Tip}} = 11°$, referred to 0,95 *r/R*, which can be seen in figure 7.24.

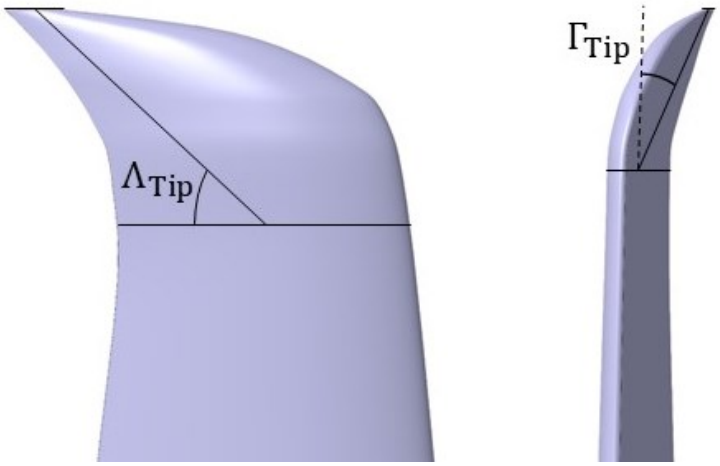

Figure 7.24: Blade tip sweep angle Λ_{Tip} and anhedral angle Γ_{Tip} geometry specification

Because of the lack of data available in literature, two different sizes of tip modifications are investigated. The larger tip (see Fig. 7.25 in the middle) differs from the already described tip (see Fig. 7.25 on the left) by the twice as large blade tip sweep angle Λ_{Tip}. The third tip, which can be seen in figure 7.25 on the right side, is identical to the initial tip but additionally a trailing edge notch at 95% of the radius is added. According to the promising results by [44], the best effect can be accomplished if the trailing edge notch has similar dimensions as the one investigated in the published paper. There, the depth was set to 2,65% of the radius and the width to 1,28%. Those percentages are also used for the notch applied in this thesis.

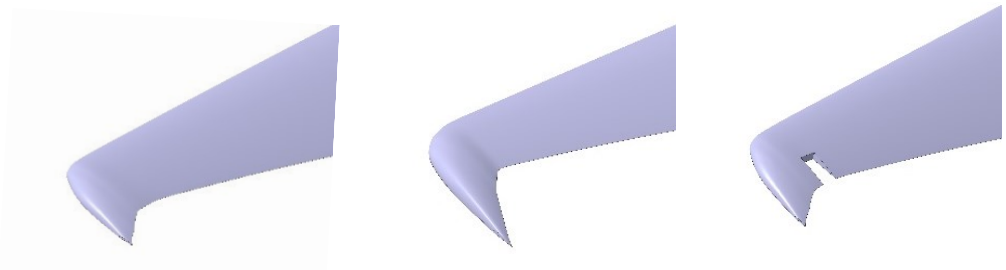

Figure 7.25: Case 3 with blade tip modifications created in CATIA V5: small tip (left), large tip (middle) and small tip with trailing edge notch (right)

Due to the modifications, different thrust values are generated, which are displayed in figure 7.26 in comparison to the reference propeller. As a result of the increased surface area, the larger tip (light blue line) produces locally more thrust, the smaller tip (dark blue line) follows this scheme in a reduced version. On the other hand, the cut-out notch (purple line) is exactly large enough to compensate for the minor thrust increases of the small tip modification.

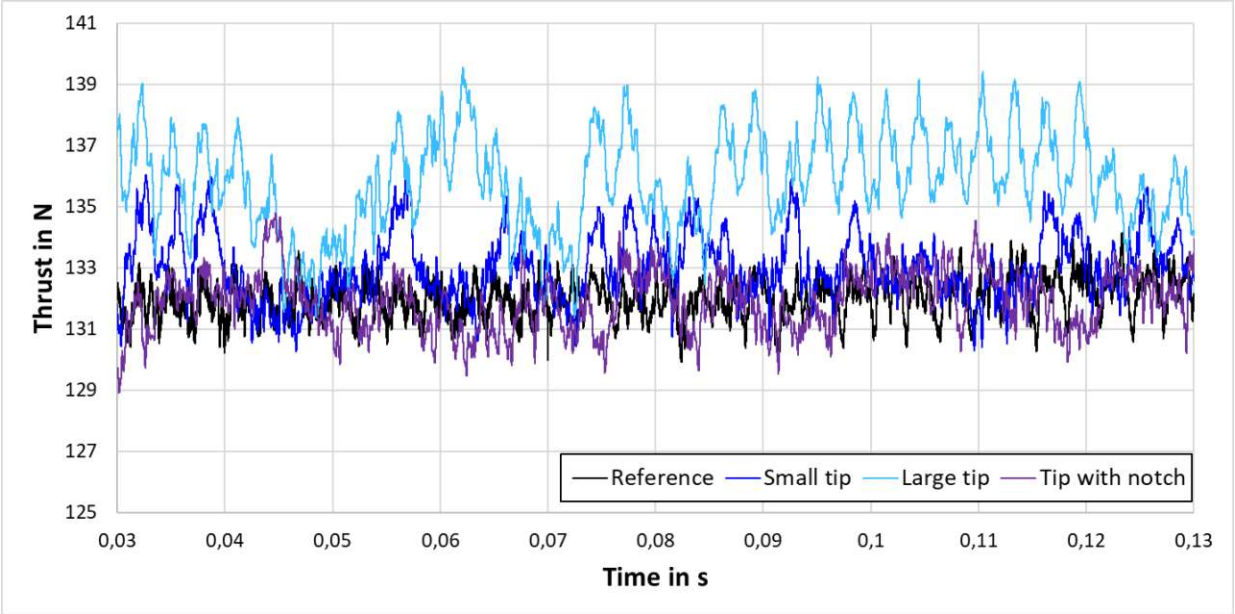

Figure 7.26: Comparison of the generated thrust by the propeller of the reference case and the propellers with different tip modifications

Moreover, the required power input to rotate the propeller at the predefined rotational velocity changes as well. The percentages in relation to the reference blade tip are summarised in table 12. As assumed, the larger tip requires the most additional power. The notch reduces the power increase of the smaller tip to approximately the original value of the reference case. In addition, the tip Mach numbers as defined in [12] are also compared in this table. Figure 7.27 shows the effect of the notch on the formation and size of tip vortices. This qualitative representation is intended to show the comparable size of the vortices of the two configurations.

Table 12: Overview of the mechanical power differences and tip Mach number values of the defined tip modifications in comparison to the reference blade tip

Tip modification	Mechanical power	Tip Mach number
Reference tip	0 %	0,521
Small tip	+ 2 %	0,526
Large tip	+ 3,5 %	0,529
Small tip with notch	+ 0,5 %	0,527

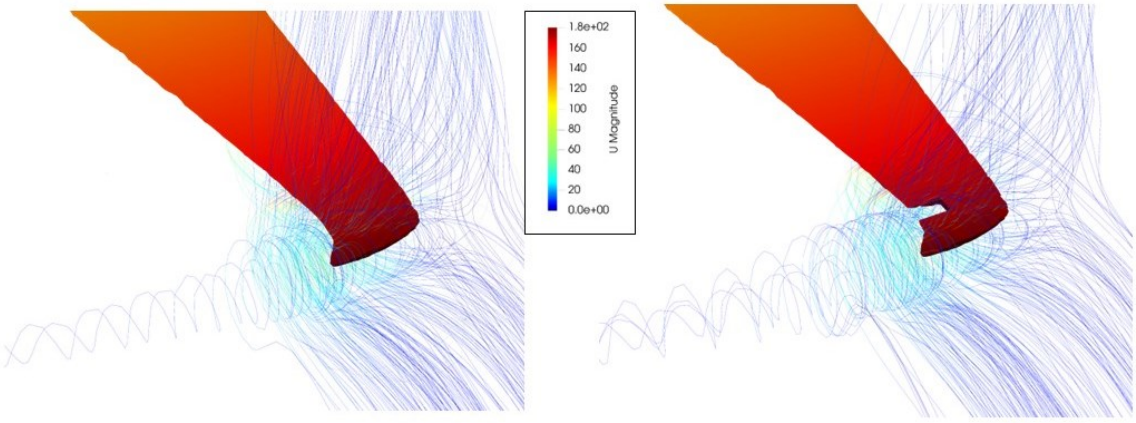

Figure 7.27: Velocity streamlines (in m/s) indicating tip vortices at the small tip (left) and the tip with the notch (right)

The direct comparison of the SPL results of the small tip as well as the large tip modification and the reference propeller, which can be seen in figure 7.28, enhances the advantage of the swept tapered anhedral tip. Minor decibel reductions of the narrow band random and broadband noise are visible in the rotational plane for both sizes of the tip modification.

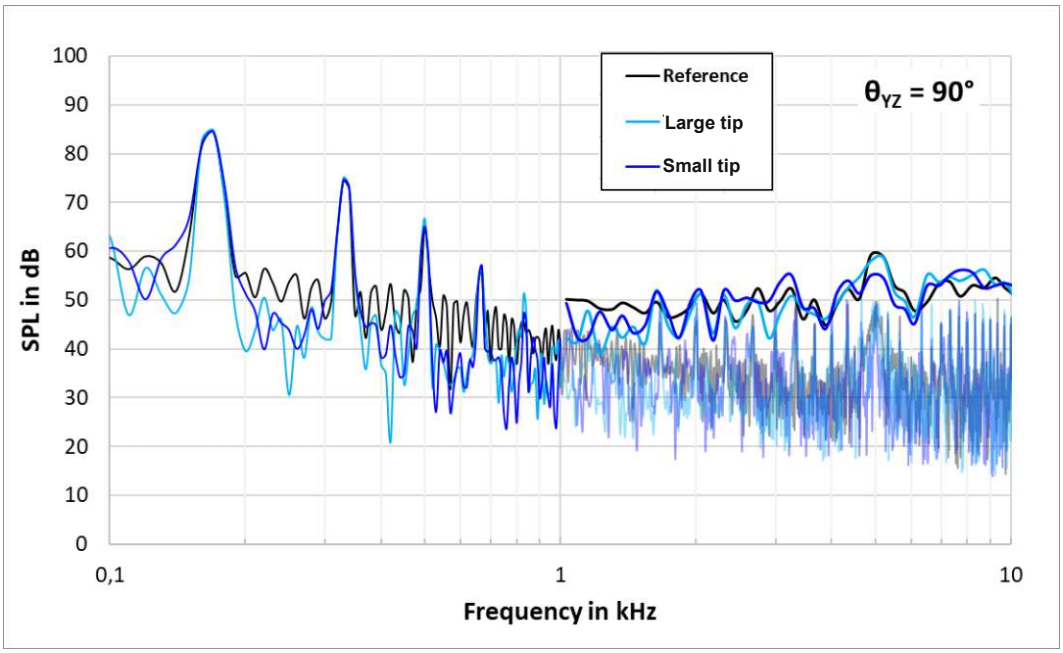

Figure 7.28: Comparison of the SPL results for the propeller with the small tip modification and the one with the large tip modification plotted over the frequency for an observer at θ = 90° in relation to the reference propeller

Nevertheless, the smaller tip is selected as the more suitable modification. Therefore, only the addition of the trailing edge notch to this modification is tested. For the sake of clarity, the influence of the notch is shown in a separate figure (see Fig. 7.29). The addition of the notch results in an even further reduction of the narrow band random as well as broadband noise. This is clearly indicated by the 1/12 octave band results, which for example show a decibel reduction of about 10 dB between 1000 and 1500 Hz. However, the tonal noise peaks at the blade passing frequencies remain unchanged.

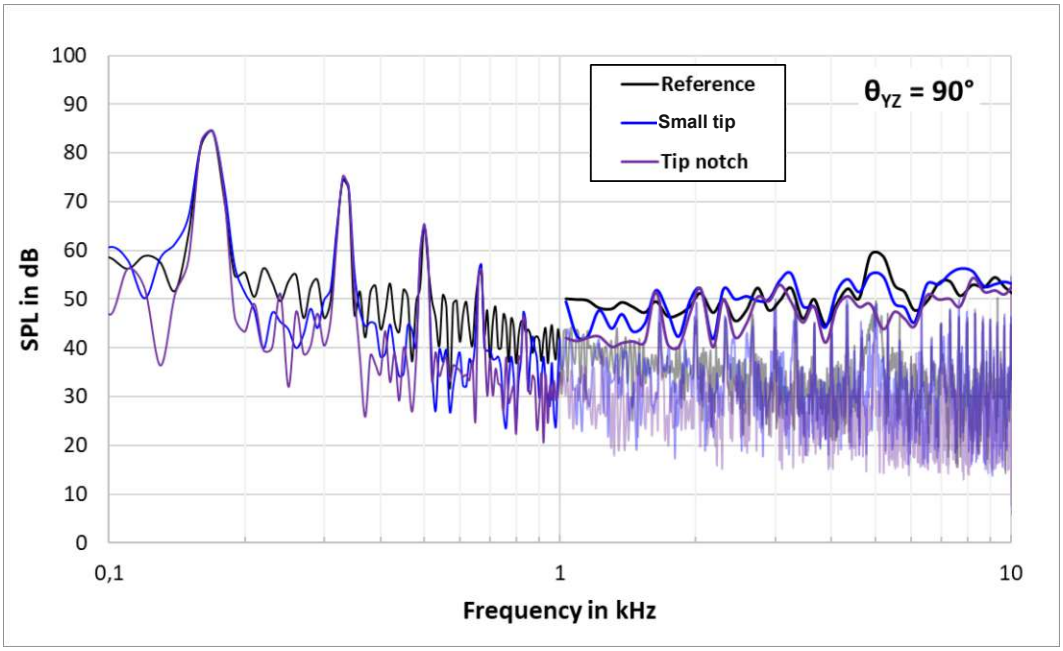

Figure 7.29: Comparison of the SPL results for the propeller with the small tip modification and the one with the notch plotted over the frequency for an observer at θ = 90° in relation to the reference propeller

The analysis of the directivity patterns for the small tip and the small tip with notch, which are displayed in figure 7.30, show minimal deviations from each other. In relation to the reference propeller, differences can be seen in front of the propeller. While small increases are visible for the first two BPFs, there are occasional reductions for the third one. The characteristics of the thickness and loading noise sources are comparable to those known from the reference case. The OASPL results indicate a reduction of the SPL values in front of the propeller, which is more pronounced in the case without the notch. The directivity results in the xz plane show the expected monopole characteristics.

Finally, the consistency of the thrust, the almost equal required mechanical power and the reduced SPL output favor the implementation of the notch. Therefore, this feature is applied in addition to the swept tapered anhedral tip in upcoming simulations of the combination of the modifications. A study to determine the influence of blade tip sweep angle and anhedral angle on the aerodynamic and aeroacoustic behaviour of propellers of this size is necessary to further improve the results.

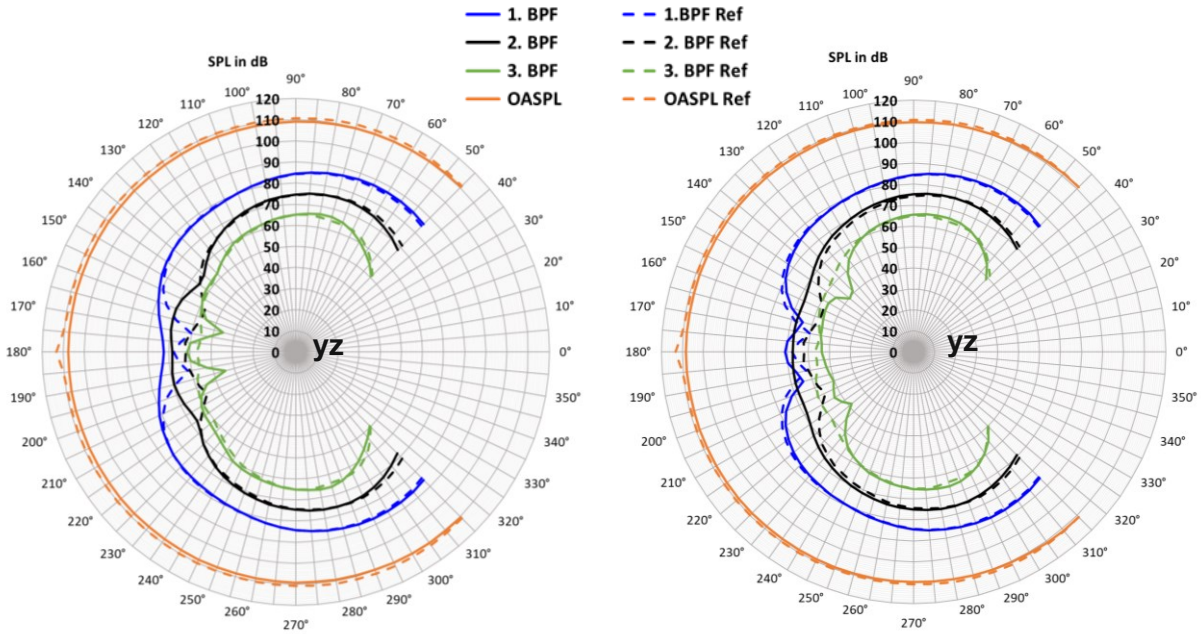

Figure 7.30: Directivity plots of the yz plane for the propeller with the small tip (left) and the same one with applied notch (right) for the first three BPFs and the OASPL in comparison to the reference propeller (dashed lines)

7.3 Combination of geometrical modifications

After the individual examination of the different modifications, this chapter investigates the aerodynamic and aeroacoustic effects of the combination of all three described adjustments. The final geometry is displayed in figure 7.31 as a CATIA model. It must be noted that the combination only refers to the specifications of these modifications as a result of a literature research. A subsequent adaptation based on the results of the joint application would exceed the scope of this thesis especially due to the multiple geometrical and computational parameters that influence the output.

Figure 7.31: Combination of all geometrical modifications created in CATIA V5

With the combination of all geometric adjustments, special attention must also be paid to the applied mesh. The number of cells is similar to the other cases and amounts to $1{,}943 \cdot 10^6$. Furthermore, the time step size of $1 \cdot 10^{-6}$ seconds for the climb case at a rotational velocity of 5000 RPM has been selected to guarantee a maximum Courant number of less than 0,9. The generated mesh with regions of increased density, especially where the geometrical modifications are applied, can be seen in figure 7.32.

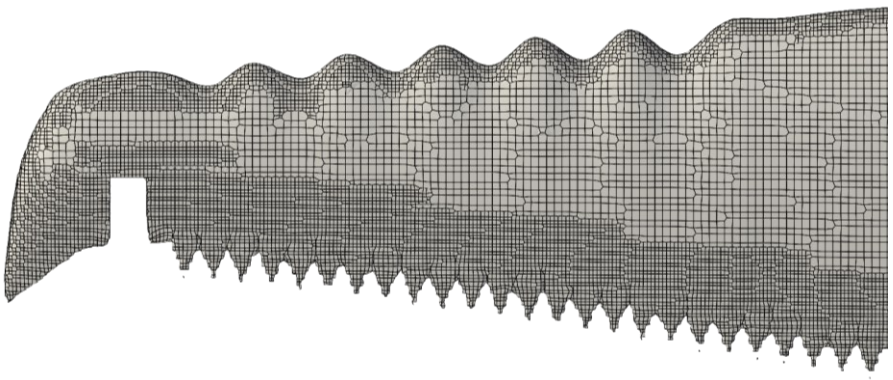

Figure 7.32: Generated mesh at the outer blade section with increased density sections

In order to find the appropriate rotational velocity that leads to the generation of the predefined thrust, a simulation with 5000 RPM is conducted first. The thrust and mechanical power output for this RPM value can be seen in the figures 7.33 and 7.34 in comparison to the reference propeller. As the time averaged thrust is just slightly higher than in the reference case (about 1%), no adaptation of the rotational velocity is carried out. This also simplifies the comparability of the data in the parameter study. It can be noted that the large thrust increase of the serrations is no longer present when combining the modifications. However, some local peaks are still visible.

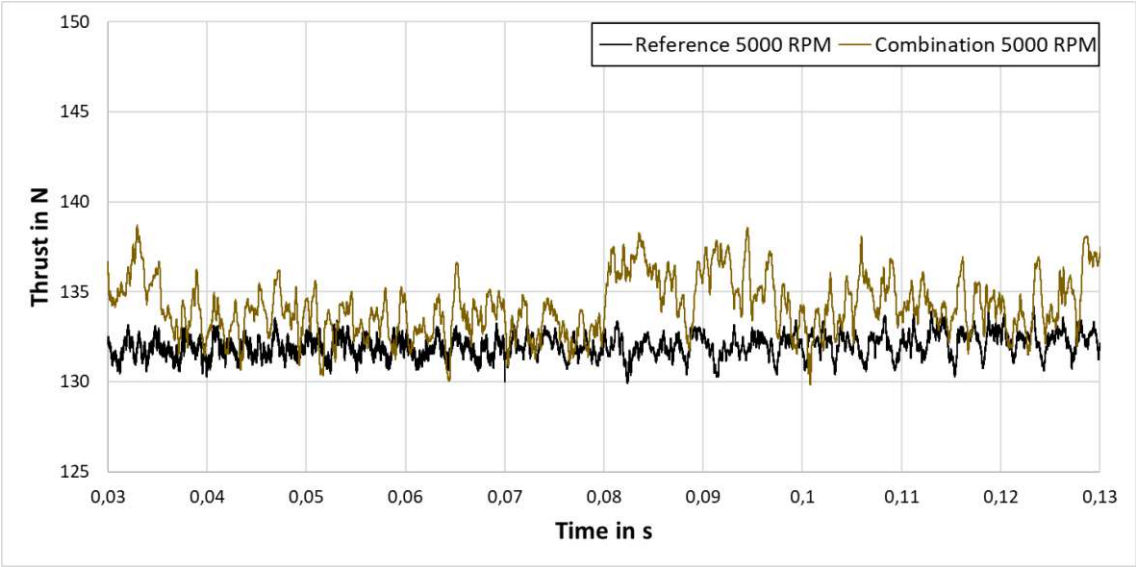

Figure 7.33: Comparison of the generated thrust by the propeller of the reference case and the one with all modifications combined at a rotational velocity of 5000 RPM

There is also a reduction of the required mechanical power due to the combination in relation to the power value output for the simulation in which the serrations are analysed individually, which resulted in an increase of about 10% compared to the reference case. The average increase for the case considered in this chapter amounts to 150 W, which corresponds to approximately 5% more power than the reference propeller required. Figure 7.34 displays the mechanical power consumption over time in comparison to the reference case.

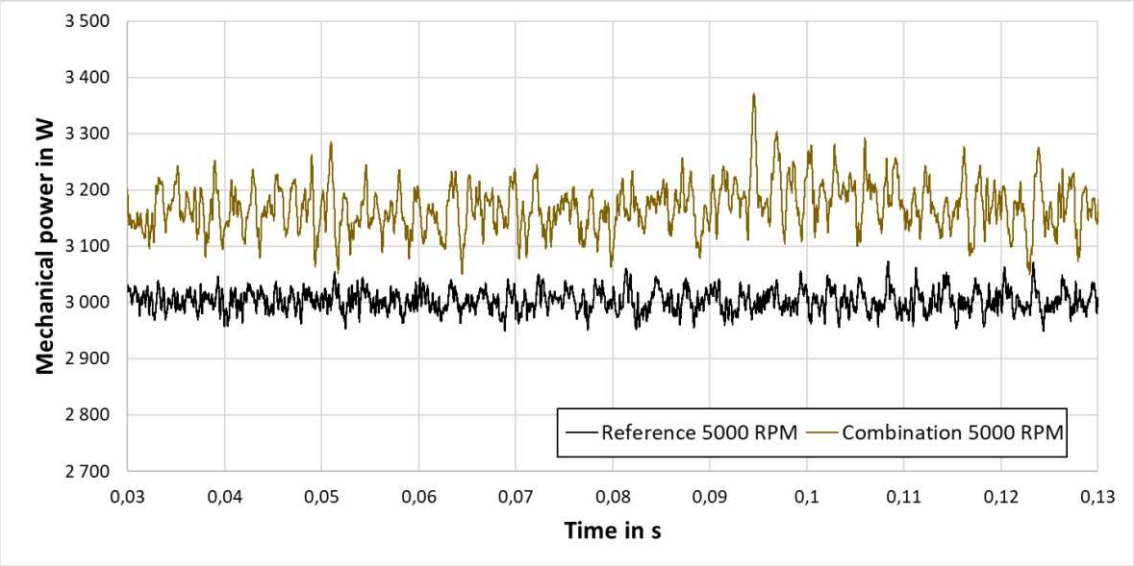

Figure 7.34: Mechanical power required by the propeller with all modifications in comparison to the propeller of the reference case at a rotational velocity of 5000 RPM

Looking at the velocity distribution, a similar pattern as for the reference case in figure 7.7 emerges at first glance. This is also indicated by the tip Mach number, which measures 0,527. However, a closer look at the tip section reveals that the velocities are distributed differently due to the tip modifications and the tubercles (see Fig. 7.35). In this context, the diameter of the vorticity fields in the wake region is slightly smaller, which can explain the obtained thrust.

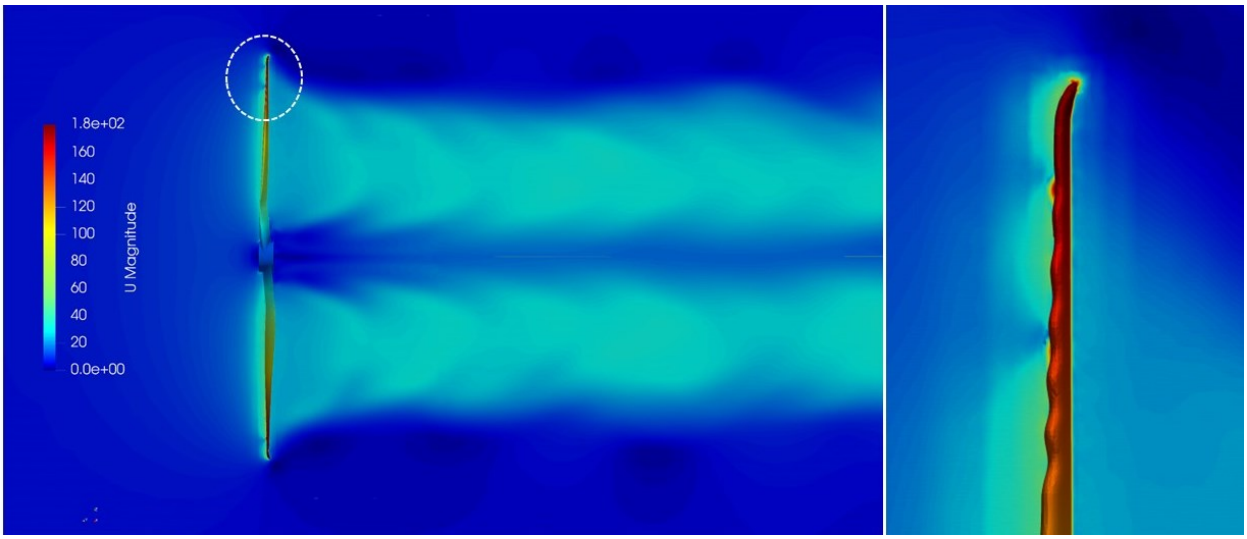

Figure 7.35 Velocity distribution (in m/s) of the propeller with all modifications combined at 0,15 s (left) and a detailed view of the tip region (right) for a freestream velocity of 5,75 m/s at 5000 RPM

The acoustic results for an observer in the rotational plane, which are displayed in figure 7.36, show a promising development. On the one hand, the tonal noise peaks at the blade passing frequencies remain high, as for all other simulations so far. The attached detailed view indicates an increase of 0,7 dB, but due to the selected frequency resolution such deviations can be neglected. On the other hand, the decrease of the narrow band random noise and sections of the broadband noise, which are also partially observed in the simulations of individual features, are preserved. The 1/12 octave band results indicate this SPL reduction of up to 8 dB at frequencies below 1500 Hz and above 5000 Hz. In addition, the local peak is no longer present at this frequency value.

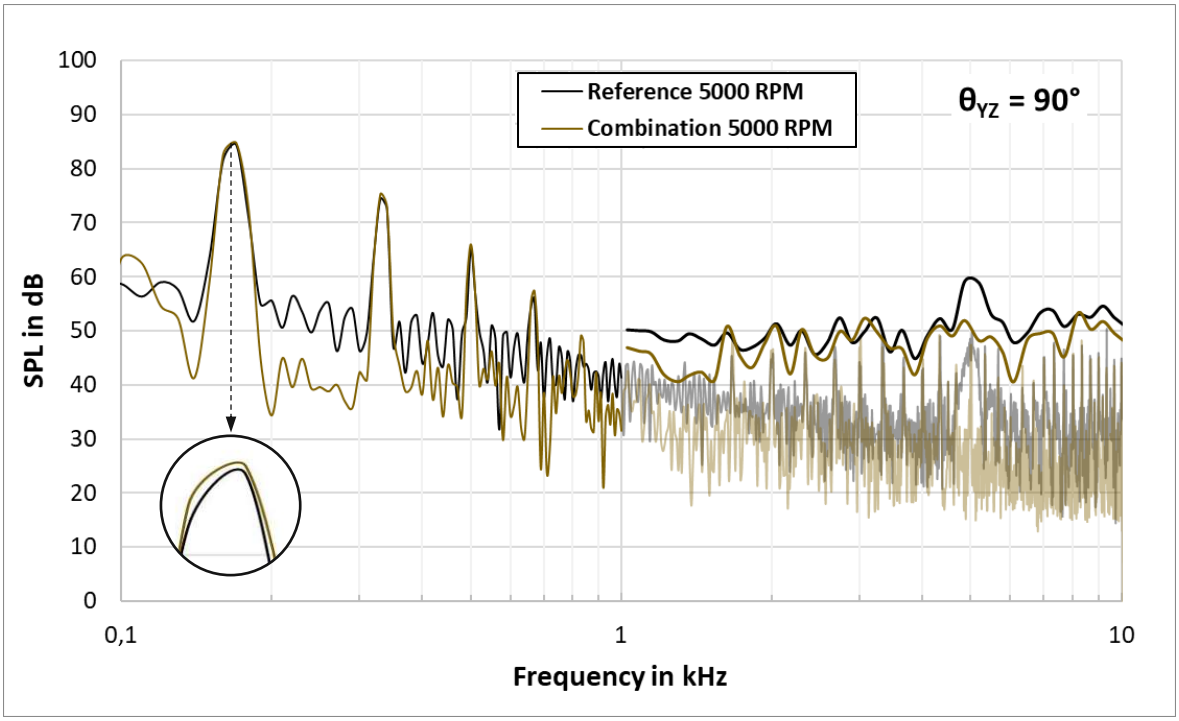

Figure 7.36: Comparison of the SPL results for the propeller with the combined modifications plotted over the frequency for an observer at θ = 90° in relation to the reference propeller at a rotational velocity of 5000 RPM

So far, the results of the directivity pattern have been difficult to interpret, as both advantages and disadvantages cannot be ruled out. Special attention must be paid to the area in front of the propeller at 180° in the yz plane, as large deviations between the results of the tubercles and the blade tip modifications can be seen here. For the combination case, all three BPFs result in almost the same SPL value at this position. The dominance of thickness noise as a monopole noise source is clearly visible, but for higher BPFs the loading noise as a dipole noise source becomes more perceptible. The OASPL result is 2 dB lower than for the reference case and shows no small local peak at 180°. The directivity pattern in the xz plane is similar to the reference propeller. The results for the combination case at a rotational velocity of 5000 RPM are displayed in figure 7.37.

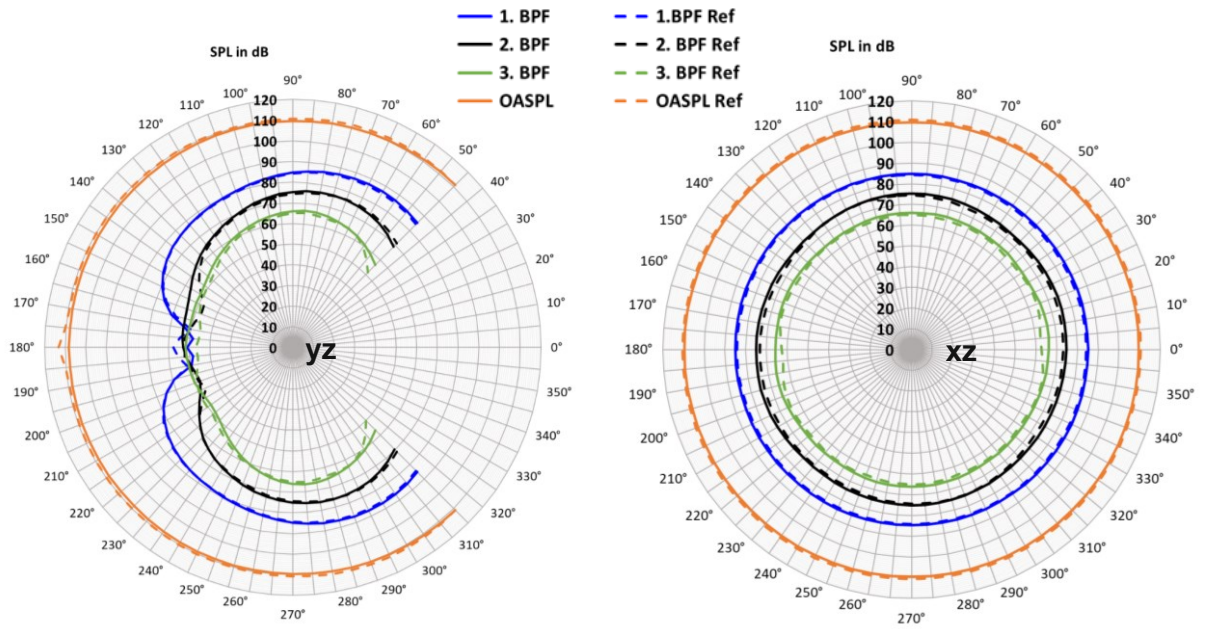

Figure 7.37: Directivity plots of the yz plane (left) and the xz plane (right) for the first three BPFs and the OASPL of the propeller with all modifications combined in comparison to the reference propeller (dashed lines)

In conclusion, it can be stated that a reduction of the noise output is definitely possible with the geometric modifications investigated for the climb phase. The most important results in terms of time averaged thrust, mechanical power and OASPL are summarized in table 13. However, to compare the frequency-dependent reduction of broadband noise, the SPL plots have to be considered. Since only one inflow velocity is examined for the vertical climb, further studies must be conducted that take other advance ratios into account. As observed for the serration case with the reduced rotational velocity, it is possible to decrease the tonal peaks while maintaining the same aerodynamic characteristics, especially with regard to the generated thrust. Accordingly, it is even more important to find the right operating conditions based on the combination of advance ratio, rotational velocity and size as well as number of propeller blades. Therefore, the advance ratio is changed in chapter 8 to simulate other operational phases. Furthermore, in the parameter study of chapter 9, the same geometry is additionally tested at other rotational velocities and compared with the reference propeller results.

Table 13: Summary of the time averaged generated thrust, time averaged required mechanical power and OASPL results in relation to the unmodified reference propeller at a rotational velocity of 5000 RPM

Modification	Thrust	Mechanical power	OASPL
LE tubercles (5000 RPM)	133,2 N (+ 0,1%)	3029 W (+ 1%)	110,3 dB (- 0,4%)
TE serrations (4820 RPM)	133,8 N (+ 0,6%)	2940 W (- 2%)	110,2 dB (- 0,5%)
Tip with notch (5000 RPM)	132,9 N (- 0,1%)	3016 W (+ 0,5%)	109,6 dB (- 1%)
Combination (5000 RPM)	134,3 N (+ 1%)	3147 W (+ 5%)	109,6 dB (- 1%)

8. Advanced simulations of hovering and descent phases

In this part of the thesis, the propeller which combines all geometrical modifications is tested regarding other operational phases which can be associated with vertical flight, namely hovering flight and descent. Therefore, the advance ratio has to be adjusted. In the following subchapters, the hover case is discussed first, since reference data are provided for this flight phase by [52]. The descending case is then analysed on the basis of the results obtained by the OpenFOAM simulations. In order to achieve better comparability, the decision was made to keep the rotational velocity constant at 5000 RPM rather than to keep the thrust constant.

8.1 Hovering flight

According to [52], the generated thrust of the reference propeller APC 27x13E amounts to 157,85 N for an advance ratio of zero at a rotational velocity of 5000 RPM. Furthermore, the mechanical power required to achieve this operating condition equals 2713 W. Both data values can be obtained from figure 7.4. As for the climb phase, the simulation model applied cannot reproduce the high thrust rates. The average value obtained for the hovering case corresponds to 134 N, as shown in figure 8.1. On the other hand, noticeably higher thrust values are achieved for the combination case, which are, however, also subject to significant temporal fluctuations. A time average yields a value of 138 N here. Due to the small deviation and for the sake of simplification and comparability of the results, the rotational velocity remains constant at 5000 RPM.

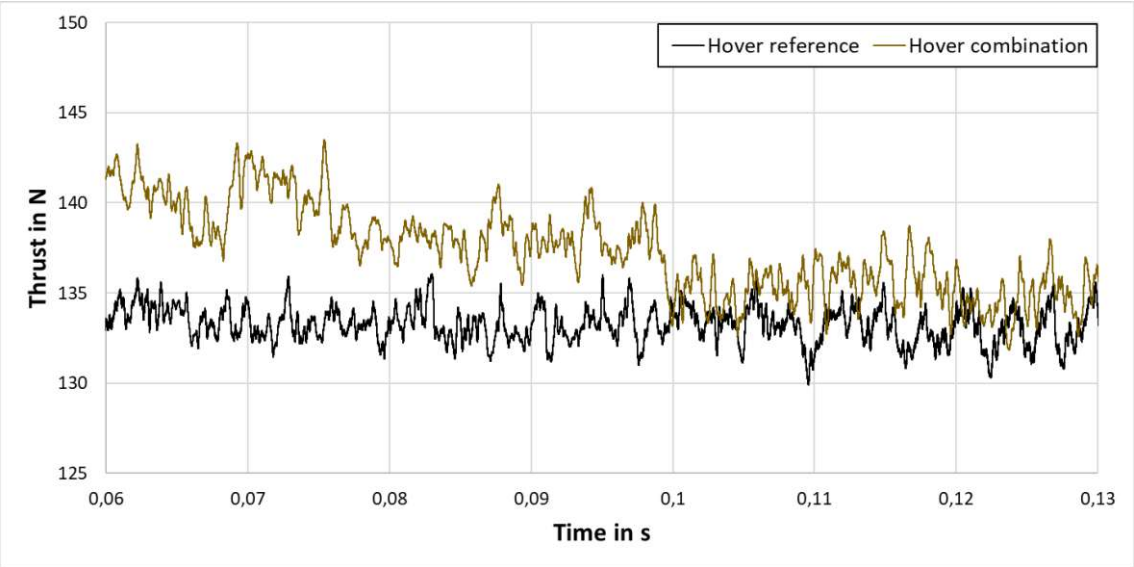

Figure 8.1: Comparison of the generated thrust by the propeller of the reference case and the one with all modifications combined for the hovering flight mode at a rotational velocity of 5000 RPM

In terms of mechanical power, there is a minimal increase in comparison to the reference case, which is displayed in figure 8.2. The deviation from the nominal value as stated in the literature is in fact slightly greater than 12%. The required power for the propeller with all modifications combined measures approximately 3200 W. The calculated tip Mach number is similar to the one of the climb case and amounts to 0,523 for the reference propeller and 0,527 for the one with all geometrical modifications.

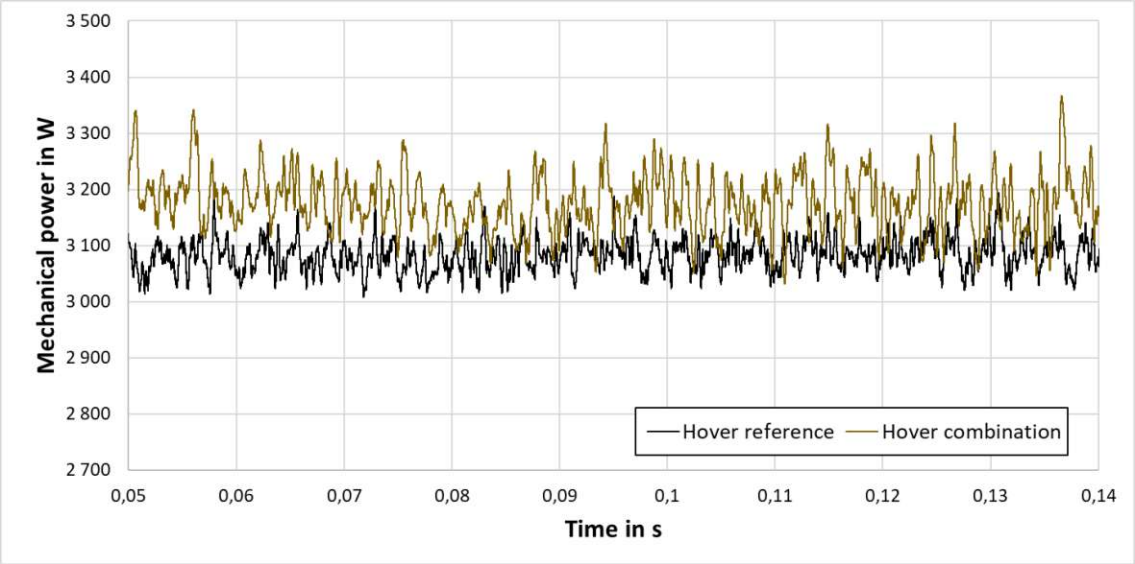

Figure 8.2: Mechanical power required by the propeller with all modifications in comparison to the propeller of the reference case for the hovering flight mode at a rotational velocity of 5000 RPM

Due to the absence of an inflow, the loading forces on the propeller surface increase because, on the one hand, the air has to be set in motion from standstill and, on the other hand, the boundary conditions are changed without a constant inflow velocity. The tonal peaks for the reference propeller achieve comparable values as for the climb phase. However, it can be observed that the propeller with combined modifications shows a decibel reduction of 5 dB at the first and third BPF. Furthermore, the fourth BPF on the other hand is clearly more pronounced for this propeller. The effects of the change in the advance ratio on the aeroacoustic behaviour are particularly noticeable at higher frequencies for the broadband noise. In contrast to the vertical climb flight, the SPL values do not drop below 20 dB at high frequency values but fluctuate between 20 dB and 50 dB. This behaviour applies to the reference propeller as well as to the modified one. These results are shown in figure 8.3 as well as the 1/12 octave band SPL values, which indicate local reductions of the decibel values for the combination case for the broadband noise frequency range.

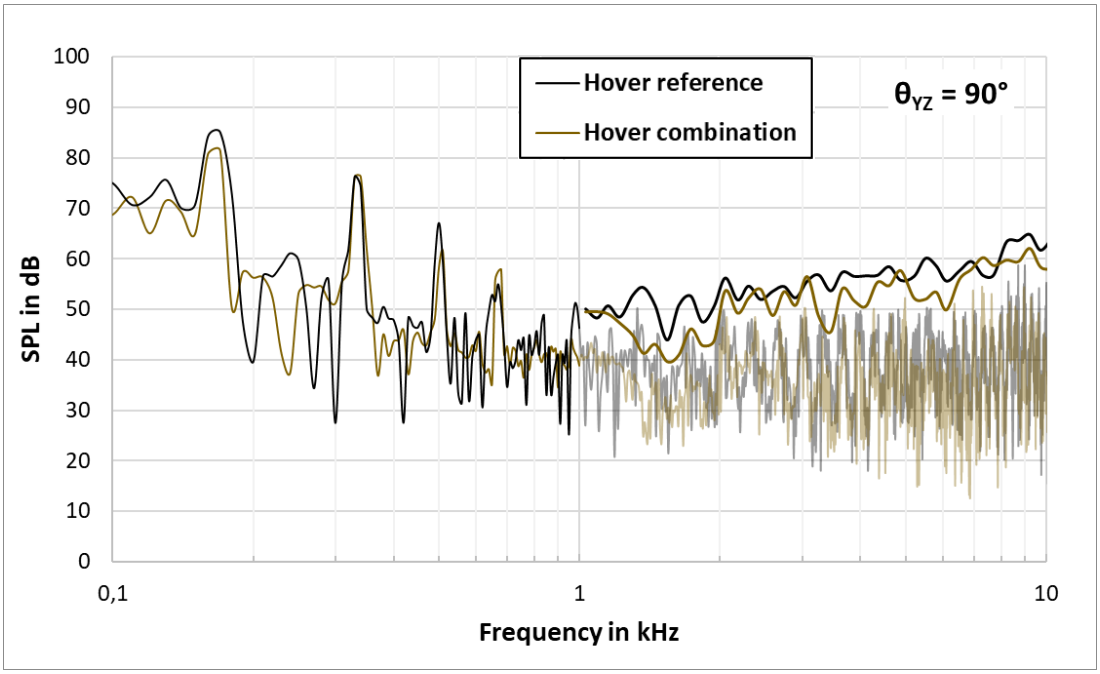

Figure 8.3: Comparison of the SPL results for the propeller with the combined modifications plotted over the frequency for an observer at θ = 90° in relation to the reference propeller at a rotational velocity of 5000 RPM for the hovering flight mode

Regarding the directivity pattern, a few differences between the flight modes and the two propeller geometries can be identified. First of all, in comparison to the vertical climb results shown in figure 7.35, there is an overall increase of the SPL output in front of the propeller in the yz plane as seen in figure 8.4. It is also important to note that the decibel values for the case with the combinations are, regarding the second and third BPF, for some observer positions significantly higher than for the reference propeller, in some regions by almost 30%. Due to the occurring superpositions of vortices as well as the not clearly assignable shapes in figure 8.4, no statements can be made about the character of the source.

In the xz plane, it is evident that the case with the combination of geometric features shows a tendency towards non pronounced monopole sources at the third blade passing frequency. According to [57], this behaviour occurs at higher harmonics, especially when they are no longer clearly distinguishable from broadband noise. Thus, the tonal noise effects can no longer be clearly detected above a certain frequency. However, the transition also varies depending on the rotational velocity and inflow velocity. Therefore, the geometrical modifications investigated in this study are not only advantageous for the hovering flight phase.

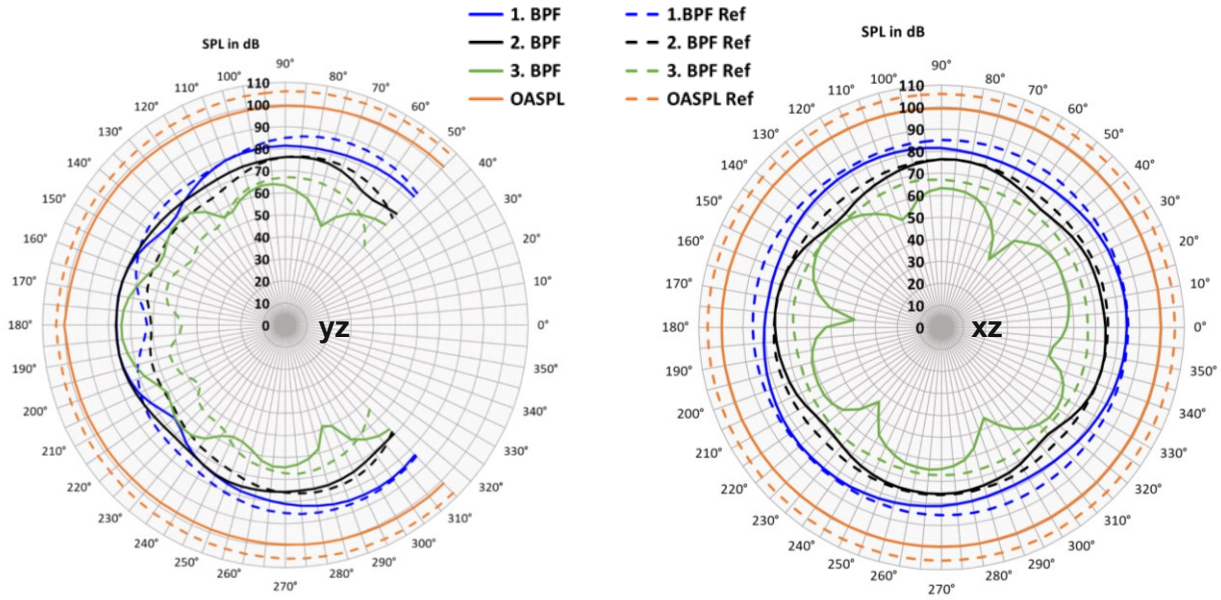

Figure 8.4: Directivity plots of the yz plane (left) and the xz plane (right) for the first three BPFs and the OASPL of the propeller with all modifications combined in comparison to the reference propeller (dashed lines) for the hovering flight mode at rotational velocity 5000 RPM

8.2 Descent flight

For this vertical flight state, no reference data are available, as it is not common to specify a negative advance ratio. Often descending flight is carried out by reducing thrust through lowering the rotational velocity. The ratio of the mass of the flying object including payload, to the generated thrust of all propulsion systems plays a decisive role. Once again, the rotational velocity is kept constant for the sake of comparability. The generated thrust plotted over time for the reference propeller geometry and the modified one is displayed in figure 8.5.

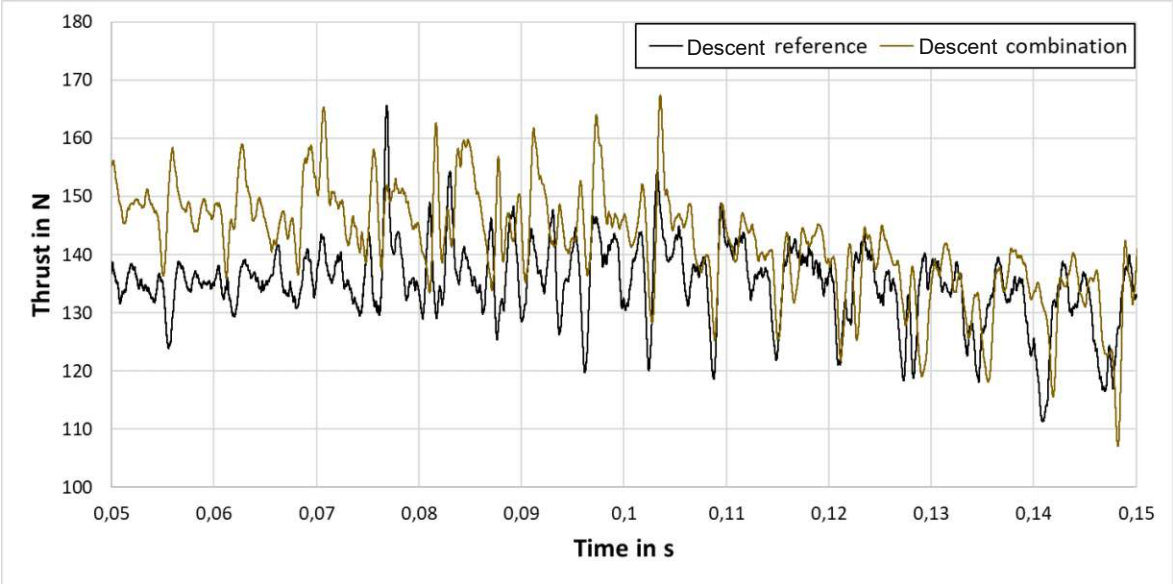

Figure 8.5: Comparison of the generated thrust by the propeller of the reference case and the one with all modifications combined for the descend flight mode at a rotational velocity of 5000 RPM

In order to avoid vortex ring state, in which a recirculation of the flows from the wake region of the propeller takes place, the same vertical velocity as in chapter 7 for the climbing flight is selected but with opposite sign. The resulting thrust varies significantly and, averaged over time, amounts to about 134 N for the reference propeller (see figure 8.5). Locally, however, peaks are to be expected that deviate by up to 30 N from this average value. The propeller with the combined modifications shows a similar behaviour although, especially before 0,1 seconds, the generated thrust is considerably higher than the one of the reference propeller. Averaged over time, this results in a thrust value of 139 N.

In contrast, the required mechanical power of both cases, which is displayed in figure 8.6, shows minor differences between the two geometries. In general, it can be stated that there are fluctuations around a value of 3100 W. For the reference case, a clear peak is again visible at the same time as for the thrust distribution. The strong oscillations can be explained by the inflow velocity, which is applied in the opposite direction to the thrust vector and therefore also has a different origin. This also shows the limitations of this simulation model. Once again, the tip Mach number of the reference case amounts to 0,523 and to 0,527 for the propeller with all modifications installed.

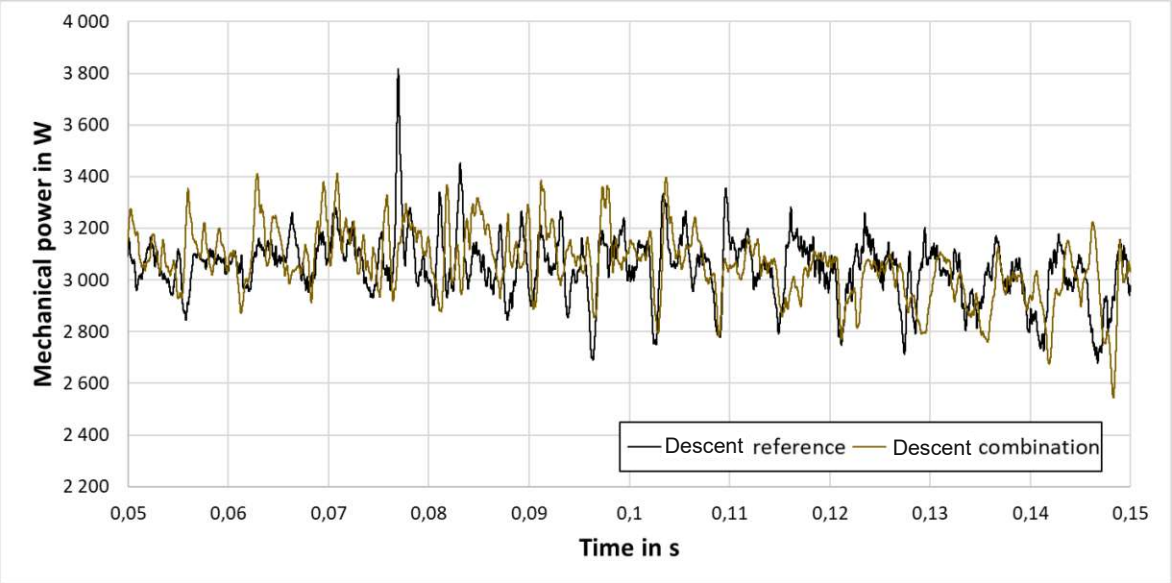

Figure 8.6: Mechanical power required by the propeller with all modifications in comparison to the propeller of the reference case for the descent flight mode at 5000 RPM

When comparing the SPL output in the rotational plane, shown in figure 8.7, with the results from the climb or hover state, a clear increase of the decibel values is noticeable. The tonal peaks at the low frequencies do not stand out as much because the narrow band random noise causes very high SPL output. In addition, the third and fourth BPF are both around 70 dB and are thus also increased in comparison to the other vertical flight modes. The broadband noise at high frequency values is elevated as well. The direct comparison of the two propellers in the

descending phase does not show a clear advantage for one of the blades. The 1/12 octave band results indicate smaller SPL values for the modified propeller until a frequency of 3000 Hz, above that the reference propeller geometry generates less noise emissions.

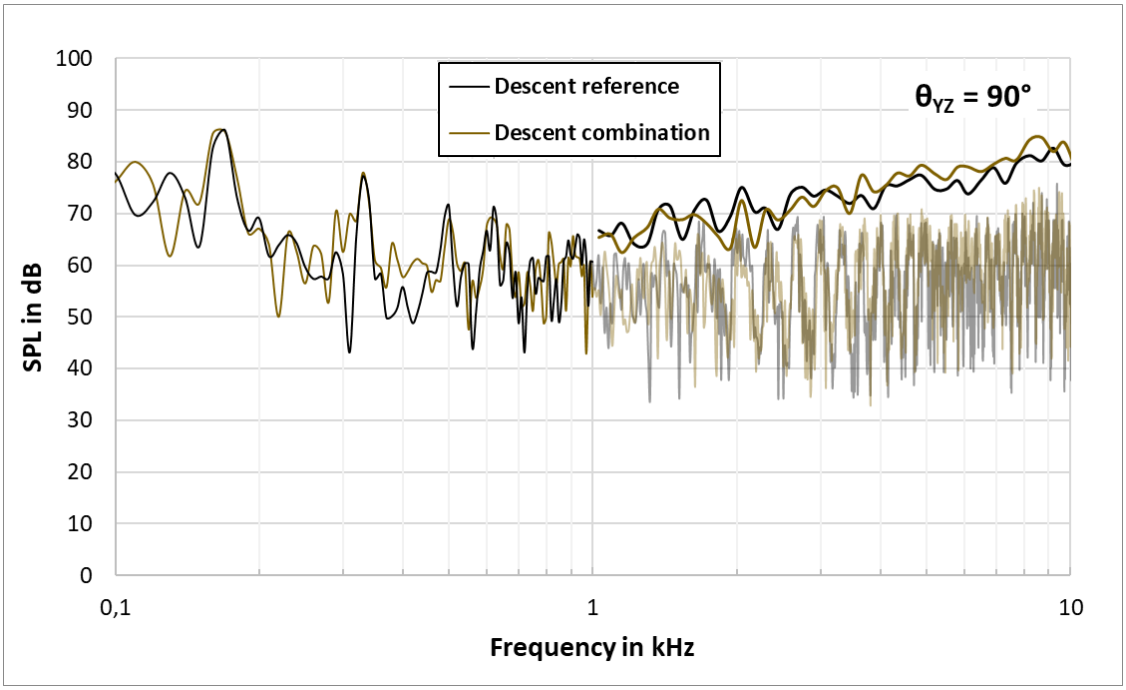

Figure 8.7: Comparison of the SPL results for the propeller with the combined modifications plotted over the frequency for an observer at θ = 90° in relation to the reference propeller at a rotational velocity of 5000 RPM for descent flight mode

Similarly to the hovering phase, the directivity pattern does not display such a strong reduction of the SPL values in front of the propeller as for the climb mode. While the first two BPFs represent a monopole source in both the yz and the xz plane, the interpretation of the third blade passing frequency is not as clear. Especially at an observer position of 180° in the yz plane, this harmonic is responsible for higher decibel values than the first two BPFs. The constrained distinguishability of the third blade passing frequency from the broadband noise is also clearly visible in the xz plane. This behaviour is very similar to the hovering case for this specific frequency value. The results of the descending flight phase are summarised in figure 8.8.

The two vertical flight modes described in this chapter show the limitations of the OpenFOAM model. At the same time, it must be noted that the geometric adjustments cannot be ideally implemented for each flight mode. Therefore, a further extensive optimisation is suggested, in which, in addition to the adjustments to the geometry, other advance ratios shall also be simulated. Notably, adjusting the inflow velocity is much more complex in terms of simulation setups than changing the rotational velocity, which is examined in the following chapter.

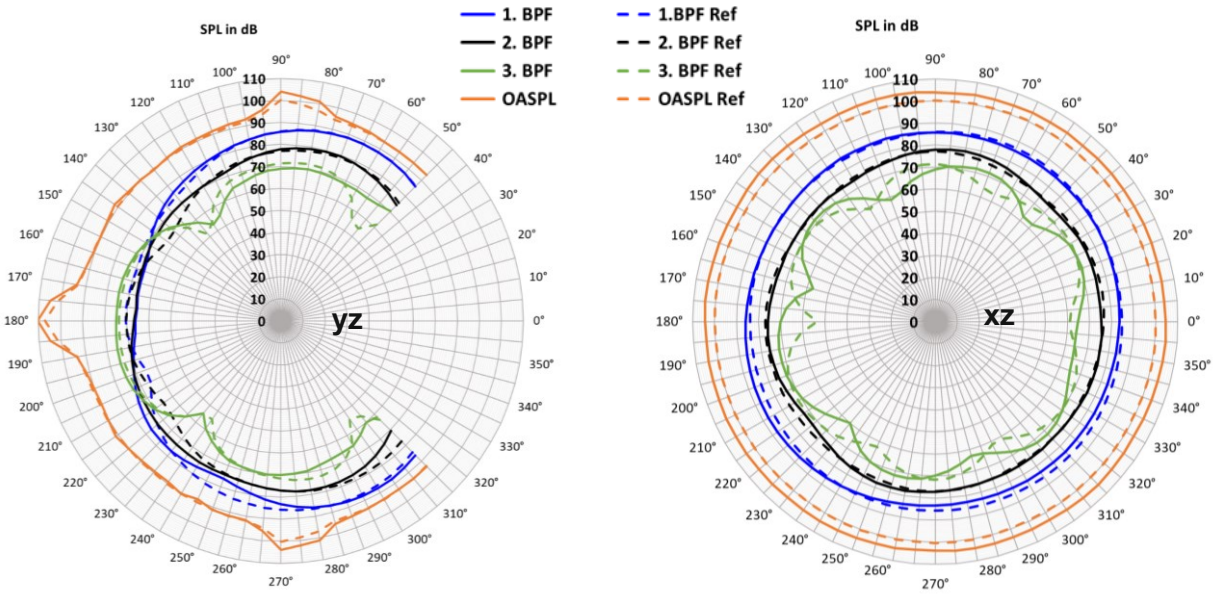

Figure 8.8: Directivity plots of the yz plane (left) and the xz plane (right) for the first three BPFs and the OASPL of the propeller with all modifications combined in comparison to the reference propeller (dashed lines) for the descent flight mode at a rotational velocity of 5000 RPM

9. Parameter study

After all vertical flight modes for an initial rotational velocity of 5000 RPM have been analysed, a parameter study for other revolution speeds is necessary to be able to classify the results more precisely. Due to the high fluctuations of the output of the hovering and descending flight modes, this parameter study is based on an advance ratio of 0,1, which corresponds to a vertical climb. The following four rotational velocities are examined, two higher and two lower than the previous value, namely 3000, 4000, 6000 and 7000 RPM. In order to provide a clear structure, only one graph of each measured parameter is shown in this chapter. The remaining diagrams can be found in the appendix.

9.1 Aerodynamic results

The most important reference values given by [52] in terms of thrust, mechanical power and tip Mach number are summarised in table 14 for all the examined rotational velocities. In addition, the blade passing frequency values calculated according to equation 2.14 are listed.

Table 14: Summary of important data of the reference propeller cases at multiple rotational velocities [52]

Rotational velocity	BPF	Thrust	Power	Tip Mach number
3000 RPM	100 Hz	50,3 N	608 W	0,32
4000 RPM	133 Hz	90,5 N	1440 W	0,43
5000 RPM	166 Hz	143,8 N	2850 W	0,54
6000 RPM	200 Hz	211,2 N	5015 W	0,64
7000 RPM	233 Hz	295,9 N	8225 W	0,75

As already mentioned in chapter 7 for 5000 RPM, the simulation of the reference geometry shows minor deviations of the thrust with regard to the listed values above. This can for example also be seen in figure 9.1 for 3000 RPM, where instead of the specified 50,3 N by the manufacturer [52], only an average thrust of 45 N is obtained by the OpenFOAM simulation. This deviation of the time-averaged thrust value of about 10% can also be seen in the other cases in figures A.1 - A.3. When considering the difference of generated thrust between both propeller geometries, it is evident that the higher the rotational velocity becomes, the smaller the variation gets. Nevertheless, no adjustments of the rotational velocities are carried out in this parameter study in order to guarantee the comparability of the data.

The tip Mach numbers are 1,5% - 2,5% too low compared to the data given by APC. Due to the not exactly defined speed of sound by [52], this may also be a relation error. In this thesis, a speed of sound of $c_0 = 343\ \mathrm{m/s}$ is assumed due to the defined boundary conditions.

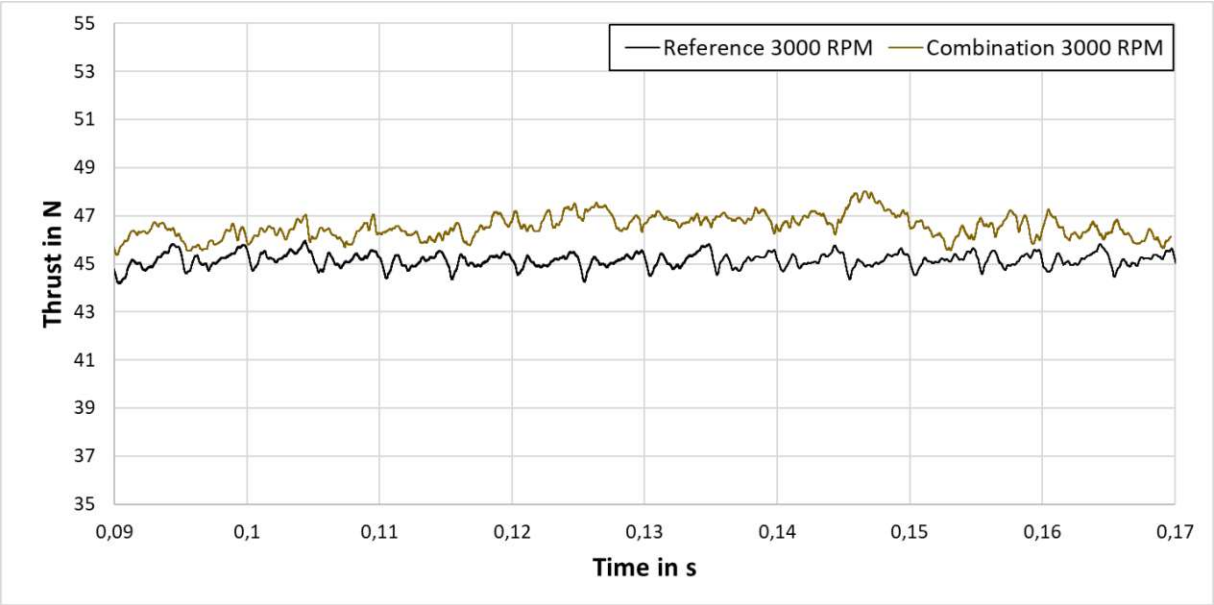

Figure 9.1: Comparison of the generated thrust by the propeller of the reference case and the one with all modifications combined at a rotational velocity of 3000 RPM

The mechanical power required to achieve the desired revolution rate is shown in this chapter for a rotational velocity of 4000 RPM (see figure 9.2). As for the thrust, a deviation between the manufacturer's datasets and the simulation results for the reference geometry can be detected here as well. Figures A.4 - A.6 show higher power values of the OpenFOAM simulations than the listed data in table 14, except for the case with a rotational velocity of 7000 RPM. Here the time-averaged simulation value is in fact lower than the reference value. Furthermore, it must be noted that the propeller geometry with all modifications applied requires more power than the unmodified case and this deviation grows with rising RPM values. Thus, the difference at 3000 RPM is only 3%, but at 7000 RPM it amounts to 6%.

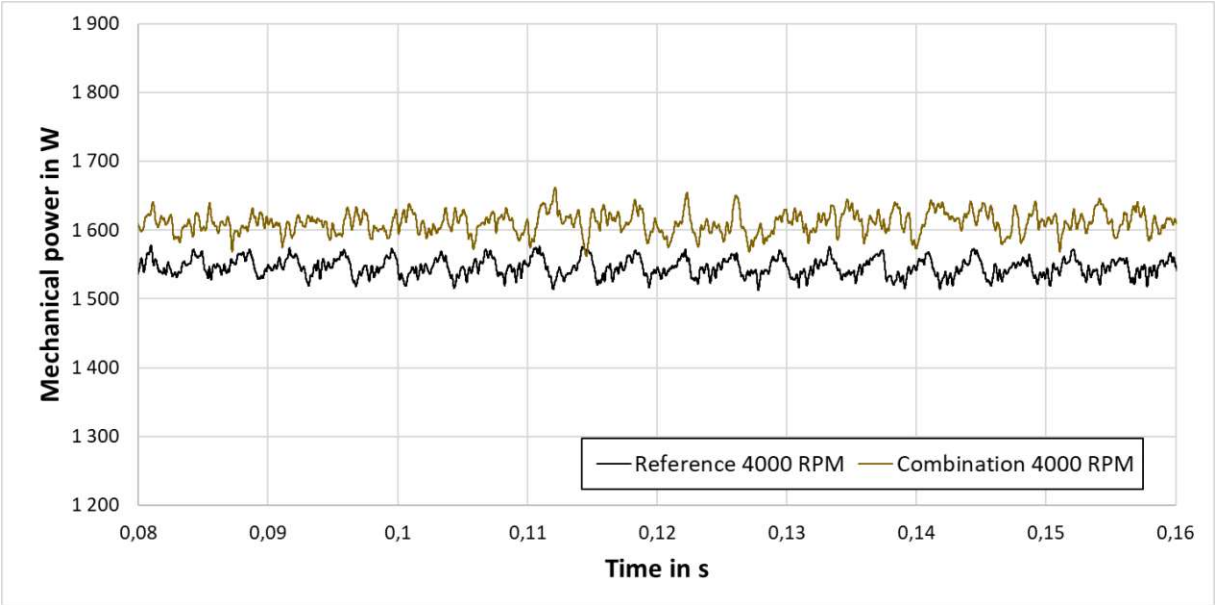

Figure 9.2: Mechanical power required by the propeller with all modifications in comparison to the propeller of the reference case at a rotational velocity of 4000 RPM

9.2 Aeroacoustic results

When considering the aeroacoustic results, it is important to take a look at the tonal peaks at the blade passing frequency values, as listed in table 14. The frequency values are met for all rotational velocities of the parameter study. However, the development of these is not always sufficiently pronounced, especially at low rotational velocities. For 3000 RPM, displayed in figure A.7, the peaks do not stand out so clearly. In general, it can be stated that an increase in rotational velocity is also directly associated with an increase in the maximum SPL values for the BPFs. This can be seen when comparing diagram 7.35 for 5000 RPM and figure 9.3 for 6000 RPM. The decibel value of the peak at the first BPF has increased by approximately 6 dB. At the same time, an increase in the narrowband random noise and broadband noise can be observed with increasing rotational velocity. The SPL values at high frequencies shift from an oscillation around approximately 25 dB at 3000 RPM to a fluctuation with a nominal value of 40 dB at 7000 RPM. This is also clearly indicated by the 1/12 octave band results.

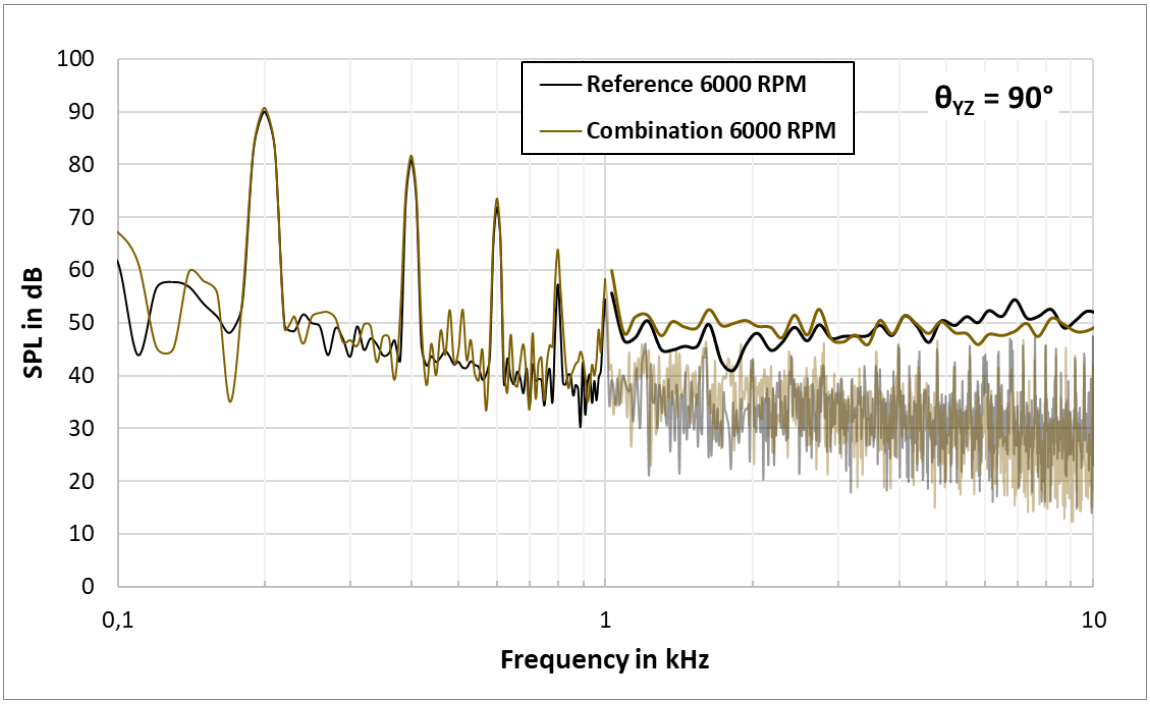

Figure 9.3: Comparison of the SPL results for the propeller with the combined modifications plotted over the frequency for an observer at θ = 90° in relation to the reference propeller at a rotational velocity of 6000 RPM

The direct comparison of the reference geometry with the modified one demonstrates a similar behaviour as described in chapter 7.3, but the magnitude is not the same for all cases. For example, for the observer in the plane of rotation at 3000 RPM (see Figure A.7), there is clearly a considerable deviation in the peaks of the harmonic noise. In addition, the narrow band random noise for the case with the combined modifications is higher at frequencies below 1000 Hz than for the unmodified case. In the broadband range, a small reduction of the decibel output occurs above 7000 HZ, according to the 1/12 octave band results. For a rotational

velocity of 4000 RPM, the behaviour is very similar to the one at 5000 RPM, but the reduction of the broadband noise at higher frequencies is not as pronounced (see figure A.8). The same applies to the rotation rate of 6000 RPM shown in Figure 9.3, where the broadband noise decrease only occurs above 6000 RPM. Lastly, the results at 7000 RPM must be studied. There is no explicit improvement of the acoustic output visible, on the contrary, the decibel values increase in almost all sections. Accordingly, the importance of optimisation becomes evident with regard to rotational velocity, advance ratio and generated thrust.

Finally, the directivity pattern at different rotational rates is studied. First, the yz plane is considered. The reference propeller data for a rotational velocity of 3000 RPM show for all examined BPFs a propagation that corresponds approximately to a monopole source (see figure A.10). The modified propeller also reflects this for the first BPF, but the harmonics indicate a minimum for the observer positioned at 180°. The SPL maxima are found at angles of 135° and 225°. This propagation has quadrupole character, but due to the Farassat analogy applied, this cannot be reproduced. The behaviour in this plane at the other rotational velocities is very similar to that described case in chapter 7.3 for 5000 RPM, which is displayed in the figures 9.4, A.11 and A.12. The limitations of the OpenFOAM model become evident when looking at the results in the xz plane. The normally purely monopole propagation of the thickness noise in this plane is not reproduced for each BPF. Especially at low rotational velocities, this noise source is not yet fully developed at the third BPF. However, the OASPL values indicate a decibel reduction of 10 dB for 3000 RPM when comparing the modified geometry to the initial one. This decrease is smaller for 4000 RPM and for higher rotational velocities there is even an increase of the OASPL visible.

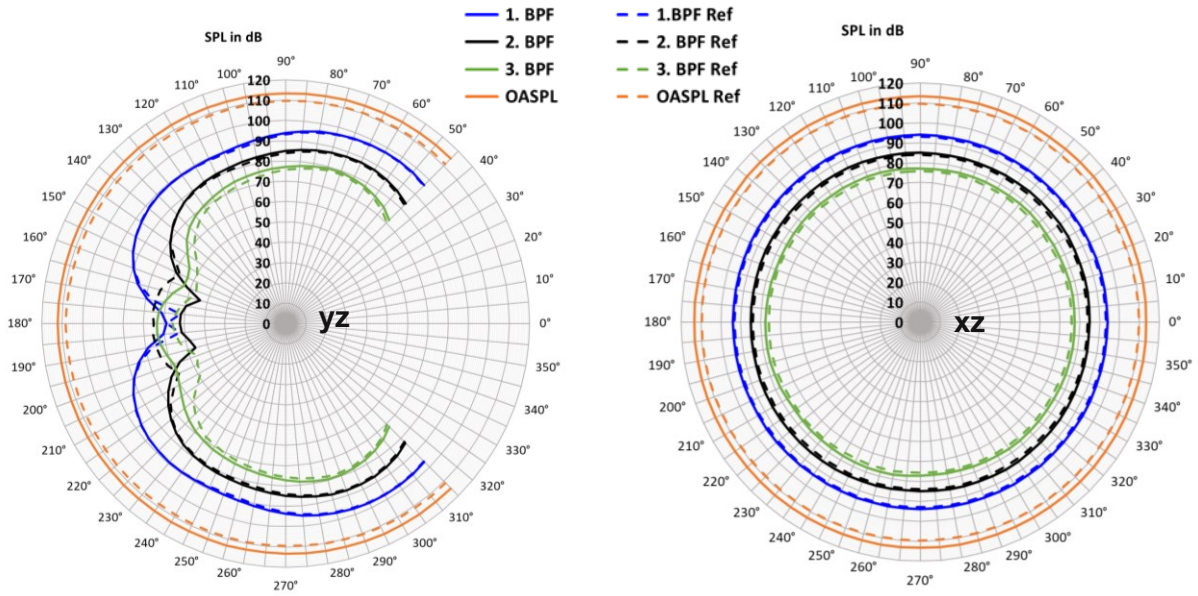

Figure 9.4: Directivity plots of the yz plane (left) and the xz plane (right) for the first three BPFs and the OASPL of the propeller with all modifications combined at a rotational velocity of 7000 RPM in comparison to the reference propeller

The collected results of this parametric study in terms of OASPL, as well as the evaluations of the different flight modes from the previous chapter, are shown in figure 9.5 for an observer at θ = 90°. The outputs of the simulations based on the reference geometry (squares) and the ones of the propeller with all combined modifications (triangles) are displayed. For the climb case, for which results are available for several rotational velocities, a clear trend of the OASPL data can be seen. For low RPM values, the overall sound pressure level is clearly lower for the combined geometry than for the unmodified one. Above a rotational velocity of about 5200 RPM this behaviour changes to the opposite. These conclusions are relevant for further studies on the optimisation of the influence of geometrical features on the acoustic behaviour.

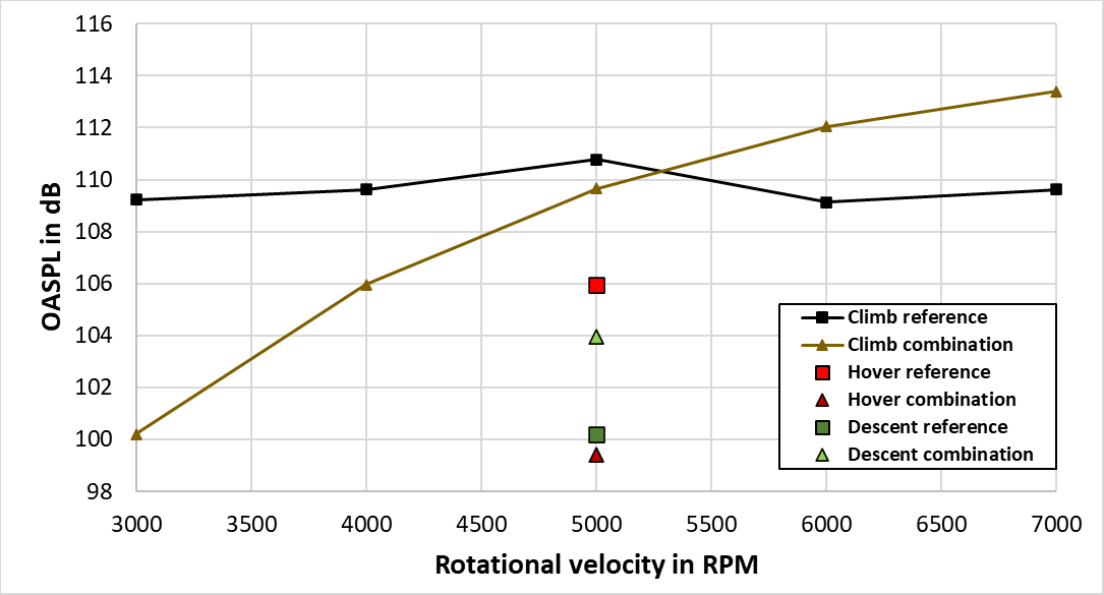

Figure 9.5: Comparison of the OASPL output at θ = 90° for the climb, hover and descent case at several rotational velocities for the reference geometry and the modified one

With regard to the other two flight modes, statements are only possible for a rotational velocity of 5000 RPM. The geometric modifications are advantageous during hovering, but disadvantageous for the descent flight case. However, it still must be considered that these are only the OASPL values and that this does not allow any conclusions about the tonal noise peaks or the broadband noise development. For that, as in the previous chapters, the individual frequency spectra must be assessed.

Regarding the generated thrust, only a small deviation between the reference propeller and the geometry with all modifications combined can be seen for all considered rotational velocities for the climb operation (see figure 9.6 green lines). On the contrary, with regard to the required mechanical power to achieve the corresponding rotational speeds, a clear deviation between the two geometries can be seen. An increase in the required power for the combination case in relation to the reference case with increasing rotational velocity is visible

(see figure 9.6 blue lines). Accordingly, operating the propellers with all modifications at higher rotational speeds is not beneficial here either. A reduction of the required power by combining these geometrical adjustments cannot be observed for any RPM value.

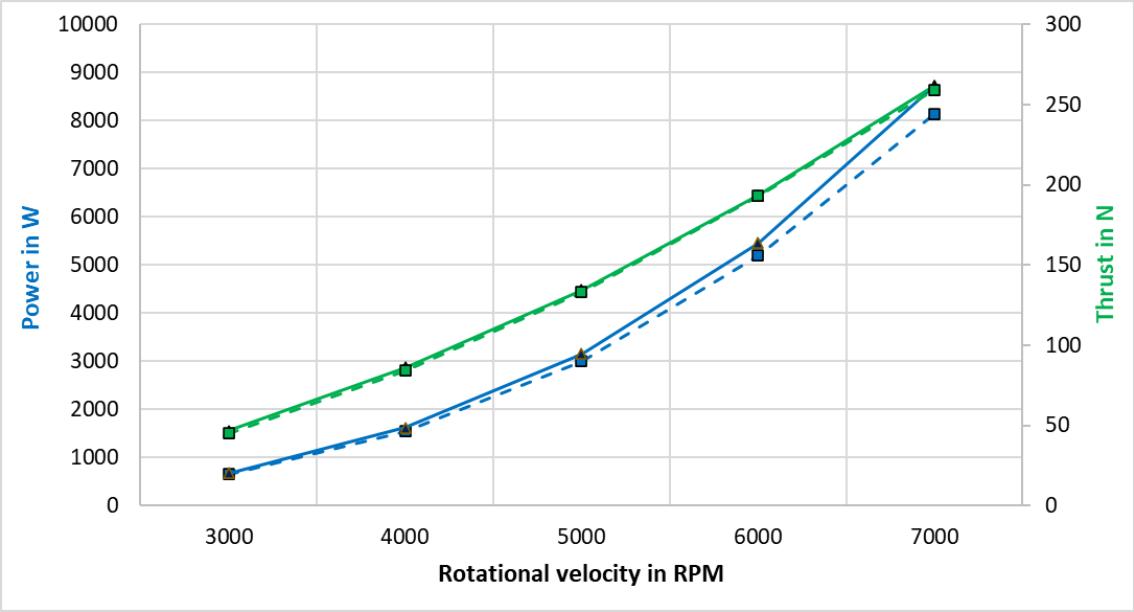

Figure 9.6: Comparison of the generated thrust (green) and the required mechanical power (blue) for the climb case at several rotational velocities for the reference geometry (dashed line, square data points) and the combination case (solid line, triangle data points)

10. Conclusion and outlook

Within the scope of this diploma thesis, numerous simulations were carried out using the CFD software OpenFOAM in order to analyse the aerodynamic and aeroacoustic behaviour of different propeller geometries. Since only aeroacoustic results for small propeller diameters are available in literature, the individual geometric features for a propeller with a diameter of 0,69 m had to be simulated first. The most promising approaches, according to a literature review, for trailing edge serrations, leading edge tubercles and tip modifications were realised. While keeping the generated thrust constant, the modifications were studied for the climb case at a nominal rotational velocity of 5000 RPM. This value could be adapted to guarantee a constant thrust. The effects of the individual geometrical adjustments described in reference papers have been observed to a certain extent in the OpenFOAM simulations as well. In this way, the application of trailing edge serrations, for example, makes it possible to reduce the broadband sound pressure level by 5 dB, depending on the frequency range, while at the same time increasing the generated thrust and maintaining the same rotational velocity. However, a 10% higher mechanical power to rotate the propeller is required.

The combination of the above-mentioned features in a single propeller blade geometry was tested for the climb, hover and descent cases at 5000 RPM. Concerning the climb case, a significant reduction of the broadband noise of up to 8 dB below 1500 Hz and above 5000 Hz can be seen. However, the tonal noise peaks as well as the directivity pattern and the OASPL output are hardly changed compared to the reference. The hover and descent flight mode results lead to an increased broadband noise in relation to the reference geometry, however, there is a general decrease of the OASPL output value for the investigated rotational velocity. The combination of geometric modifications leads to a noise reduction in the hover case in comparison to the results of the reference geometry in that flight mode, while the opposite is observed for the descent flight case.

The parameter study carried out for the climb case at different rotational velocities shows that, in relation to the OASPL output, there is an RPM value that can be considered as the transition point. Below this rotational velocity, the combination of geometric modifications leads to a reduction of noise emissions, above it, the opposite is to be expected. However, an individual examination of the frequency spectra and the directivity plots at the rotational velocities below the transition point does not indicate a clear direct SPL reduction neither in the broadband noise range nor in the tonal peaks. Accordingly, all individual data sets must also be taken into account for the overall assessment.

The results of the OpenFOAM simulations of this diploma thesis indicate that a potential for noise minimisation is given by combining several geometrical modifications. Additionally, it can be concluded that the geometric adjustments investigated in literature for small propeller diameters up to 0,3 m are also applicable for larger sizes of propellers. The perspective for optimisation in terms of aerodynamic and aeroacoustic properties through the application of geometric modifications is very promising. Therefore, it is even more important to find a consensus between rotational velocity, advance ratio, required power, generated thrust and diameter of the propeller in combination with the targeted application of geometrical adjustments. Particular attention must be paid to the different vertical flight modes in the optimisation process.

The aeroacoustics of geometric modifications during horizontal flight have not been studied. Therefore, this represents a future field of research. It also has to be mentioned that fundamental changes in geometry, such as those applied in Airbus' blue edge concept, also need to be studied in more detail in this context. Additional basic parameter studies of the individual geometrical features must be carried out for different diameters, as the acoustic influence also depends on the magnitude of the environmental parameters. More in-depth simulations must be conducted with another simulation software, as the externally implemented acoustic library in OpenFOAM also has its limitations in terms of turbulence model selection and post processing capabilities. Furthermore, the utility of the obtained information in other fields of application is possible. From blades of a turbofan engine to the ones of a helicopter rotor and fans of electrical devices, there are several areas of application which can also benefit from a reduction of the noise output.

11. References

[1] Metzger F. B.: A review of propeller noise prediction methodology: 1919-1994. NASA Contractor Report 198156 (1995). p. 3 – 66, URL: https://ntrs.nasa.gov/citations/19960008819 (accessed 07/2023)

[2] Joby Aviation, URL: https://www.jobyaviation.com (accessed 07/2023)

[3] Pascioni K. A., Watts M. E., Houston M., Lind A., Stephenson J. H., Bain J.: Acoustic Flight Test of the Joby Aviation Advanced Air Mobility Prototype Vehicle. AIAA 2022-3036 (2022). 28th AIAA/CEAS Aeroacoustics 2022 Conference, URL: https://doi.org/10.2514/6.2022-3036 (accessed 07/2023)

[4] CityAirbus NextGen, URL: https://www.airbus.com/en/innovation/zero-emission-journey/urban-air-mobility/cityairbus-nextgen (accessed 07/2023)

[5] Phoenix Wings ORCA, URL: https://phoenixwings.com/pworca/ (accessed 07/2023)

[6] Jetson One eVTOL, URL: https://www.jetsonaero.com/jetson-one (accessed 07/2023)

[7] Glegg S., Devenport W.: Aeroacoustics of Low Mach Number Flows: Fundamentals, Analysis, and Measurement. Academic Press (2017).

[8] Sound Fields: Free versus Diffuse Field, Near versus Far Field. Siemens (2020). URL: https://community.sw.siemens.com/s/article/sound-fields-free-versus-diffuse-field-near-versus-far-field (accessed 07/2023)

[9] Möser M.: Technische Akustik. Springer-Verlag Berlin Heidelberg (2007). Volume 7, p. 100-103, URL: https://doi.org/10.1007/978-3-540-71387-6 (accessed 07/2023)

[10] Sinambari G. R., Sentpali S.: Ingenieurakustik: Physikalische Grundlagen und Anwendungsbeispiele. Springer Vieweg Wiesbaden (2014). Volume 5, URL: https://doi.org/10.1007/978-3-658-05072-6 (accessed 07/2023)

[11] DIN Deutsches Institut für Normung e.V. EN 61260-1: Elektroakustik – Bandfilter für Oktaven und Bruchteile von Oktaven – Teil 1: Anforderungen. Beuth Verlag (2014). IEC 61260-1:2014, p. 34

[12] Henricks Q. M.: Computational Aerodynamic and Aeroacoustic Study of Small-scale Rotor Geometries. Ohio State University. Department of Mechanical and Aerospace Engineering (2019). URL: https://etd.ohiolink.edu/apexprod/rws_etd/send_file/send?accession=osu1546618814905583&disposition=inline (accessed 07/2023)

[13] Fast Fourier Transformation FFT – Basics. NTi Audio, URL: https://www.nti-audio.com/en/support/know-how/fast-fourier-transform-fft (accessed 07/2023)

[14] Pandey A.: Investigation of propeller characteristics at low Reynolds number with an angle of attack: A computational aeroacoustic study. Master thesis (2021). Delft University of Technology, URL: https://repository.tudelft.nl/islandora/object/uuid%3A8b1692b1-ec8e-41a0-99f6-1a76a5c26fdc (accessed 07/2023)

[15] Müller G., Möser M.: Strömungsgeräusche. Springer Vieweg (2017). Fachwissen Technische Akustik, Volume 1, URL: https://doi.org/10.1007/978-3-662-55438-8 (accessed 07/2023)

[16] Korchagova V., Kraposhin M., Strijhak S.: Computational Aeroacoustics Methods with OpenFOAM v. 4.1. 12th OpenFOAM Workshop (2017). URL: 10.13140/RG.2.2.32022.24641 (accessed 07/2023)

[17] Gutin L.: On the Sound Field of a Rotating Propeller. NACA Technical Memorandum 1195 (1948). URL: https://ntrs.nasa.gov/citations/20030068996 (accessed 07/2023)

[18] Lighthill M. J.: On sound generated aerodynamically: I. General theory. Proceedings of the Royal Society London (1952). Volume 211, p.564–587, URL: http://doi.org/10.1098/rspa.1952.0060 (accessed 07/2023)

[19] Kaltenbacher M.: Computational Acoustics. Springer International Publishing (2018). CISM International Centre for Mechanical Sciences, Volume 579, URL: https://doi.org/10.1007/978-3-319-59038-7 (accessed 07/2023)

[20] Epikhin, A., Evdokimov, I., Kraposhin, M., Kalugin, M., Strijhak, S.: Development of a Dynamic Library for Computational Aeroacoustics Applications Using the OpenFOAM Open Source Package. Procedia Computer Science (2015). Volume 66, p. 150 -157, URL: 10.1016/j.procs.2015.11.018 (accessed 07/2023)

[21] Curle N.: The influence of solid boundaries upon aerodynamic sound. Proceedings of the Royal Society London (1955). Volume 231, p. 505-514, URL: http://doi.org/10.1098/rspa.1955.0191 (accessed 07/2023)

[22] Ffowcs Williams J. E., Hawkings D. L.: Sound Generation by Turbulence and Surfaces in Arbitrary Motion. Philosophical Transactions of the Royal Society of London (1969). Series A, Mathematical and Physical Sciences, Vol. 264, No. 1151, p. 321-342, URL: https://doi.org/10.1098/rsta.1969.0031 (accessed 07/2023)

[23] Farassat F., Brentner K.: The Acoustic Analogy and the Prediction of the Noise of Rotating Blades. Theoretical and Computational Fluid Dynamics (1998). Volume 10, p. 155–170, URL: https://doi.org/10.1007/s001620050056 (accessed 07/2023)

[24] Ghosh D.: Implementation of the FWH aero-acoustic analogy for sector analysis of an axi-symmetric turbomachine. In Proceedings of CFD with OpenSource Software (2021). Edited by Nilsson, Chalmers University of Technology, URL: http://dx.doi.org/10.17196/OS CFD#YEAR 2021 (accessed 07/2023)

[25] Hubbard H. H.: Aeroacoustics of Flight Vehicles: Theory and Practice. NASA Reference Publication 1258 (1991). Volume 1, p. 1 – 64, URL: https://ntrs.nasa.gov/citations/19920001380 (accessed 07/2023)

[26] Filippone A.: Aircraft Noise: Noise Sources. In Advanced Aircraft Flight Performance, Cambridge University Press (2012). Cambridge Aerospace Series, pp. 470-532, URL: https://doi.org/10.1017/CBO9781139161893.019 (accessed 07/2023)

[27] Kurtz D. W., Marte J. E.: A review of aerodynamic noise from propellers, rotors, and lift fans. NASA technical report (1970). Technical report 32-1462, URL : https://ntrs.nasa.gov/citations/19700005920 (accessed 07/2023)

[28] Hanson D. B., Fink M. R.: The importance of quadrupole sources in prediction of transonic tip speed propeller noise. Journal of Sound and Vibration (1979). Volume 62, Issue 1, p. 19-38, URL: https://doi.org/10.1016/0022-460X(79)90554-6 (accessed 07/2023)

[29] OpenFoam User Guide. OpenCFD Limited (2022). Version 2212, URL: https://www.openfoam.com/documentation/user-guide (accessed 07/2023)

[30] Nichols R.H.: Turbulence Models and Their Application to Complex Flows. University of Alabama at Birmingham (2010). Department of Mechanical Engineering, URL: https://overflow.larc.nasa.gov/wp-content/uploads/sites/54/2014/06/Turbulence_Guide_v4.01.pdf (accessed 07/2023)

[31] Greenshields C. J.: OpenFOAM User Guide. The OpenFOAM Foundation Ltd. (2022). 10th version, URL: https://doc.cfd.direct/openfoam/user-guide-v10 (accessed 07/2023)

[32] Hurt H. H. Jr.: Aerodynamics for Naval Aviators. Federal Aviation Administration (1965). URL: https://www.faa.gov/regulations_policies/handbooks_manuals/aviation/media/00-80t-80.pdf (accessed 07/2023)

[33] Lam T.: Propellers: Introduction of Aerospace Propulsion. ARO 103L (2015), URL: http://www.trylam.com/files/ARO-103L_tlam_Week2.pdf (accessed 07/2023)

[34] Wisniewski C., Byerley A., Heiser W., Van Treuren K., Liller T.: The Influence of Airfoil Shape, Reynolds Number and Chord Length on Small Propeller Performance and Noise. American Institute of Aeronautics and Astronautics (2015). 33rd AIAA Applied Aerodynamics Conference, URL: https://doi.org/10.2514/6.2015-2266 (accessed 07/2023)

[35] Pang E., Cambray A., Rezgui D., Azarpeyvand M., Showkat Ali S.: Investigation Towards a Better Understanding of Noise Generation from UAV Propellers. AIAA/CEAS Aeroacoustics Conference (2018). URL: https://doi.org/10.2514/6.2018-3450 (accessed 07/2023)

[36] de Haan W.: Impact of Blade Sweep on Aerodynamic and Aeroacoustic Performance Optimization of Isolated Propellers. Master thesis (2021). Delft University of Technology, URL: https://repository.tudelft.nl/islandora/object/uuid:09137b04-f499-47f5-9c17-7334d0ef92ac?collection=education (accessed 07/2023)

[37] Kevadiya M.: CFD Analysis of Pressure Coefficient for NACA 4412. International Journal of Emerging Trends & Technology in Computer Science (2013). Volume 4, p. 2041-2043, URL: https://www.researchgate.net/publication/305072558_CFD_Analysis_of_Pressure_Coefficient_for_NACA_4412 (accessed 07/2023)

[38] Rutkay B. D.: A Process for the Design and Manufacture of Propellers for Small Unmanned Aerial Vehicles. Master thesis (2014). Carleton University, URL: https://doi.org/10.22215/etd/2014-10450 (accessed 07/2023)

[39] Wiedemann A. D.: A Study of the Aeroacoustics of Swept Propellers for Small Unmanned Aerial Vehicles. Master thesis (2020). Mechanical & Aerospace Engineering, Old Dominion University, URL: 10.25777/8qwv-vq29 (accessed 07/2023)

[40] Hanson D. B.: Influence of propeller design parameters on far-field harmonic noise in forward flight. AIAA Journal (1980). Volume 18, number 11, p. 1313-1319, URL: https://doi.org/10.2514/3.50887 (accessed 07/2023)

[41] Wei Y., Qian Y., Bian S., Xu F., Kong D.: Experimental Study of the Performance of a Propeller with Trailing-Edge Serrations. Acoustics Australia (2021). Volume 49, p. 305-316, URL: https://doi.org/10.1007/s40857-021-00221-w (accessed 07/2023)

[42] Ning Z., Wlezien R., Hu H.: An Experimental Study on Small UAV Propellers with Serrated Trailing Edges. AIAA Fluid Dynamics Conference (2017). URL: 10.2514/6.2017-3813 (accessed 07/2023)

[43] Chong T. P., Vathylakis A.: On the aeroacoustic and flow structures developed on a flat plate with a serrated sawtooth trailing edge. Journal of Sound and Vibration (2015). Volume 354, p. 65-90, URL: https://doi.org/10.1016/j.jsv.2015.05.019 (accessed 07/2023)

[44] Treuren K. W. V., Wisniewski C. F.: Testing Propeller Tip Modifications to Reduce Acoustic Noise Generation on a Quadcopter Propeller. ASME Journal of Engineering for Gas Turbines and Power (2019). Volume 141, Issue 12, URL: https://doi.org/10.1115/1.4044971 (accessed 07/2023)

[45] Asghar A., Perez R. E., Jansen P. W., Allan W. D. E.: Application of Leading-Edge Tubercles to Enhance Propeller Performance. AIAA Journal (2020). Volume 58, p. 4659-4671, URL: https://doi.org/10.2514/1.J058740 (accessed 07/2023)

[46] Haddadi Sisakht B., Jordan C., Harasek M.: OpenFOAM® Basic Training. chemical-engineering.at (2019). 5th edition,
URL: https://repositum.tuwien.at/handle/20.500.12708/16579 (accessed 07/2023)

[47] Epikhin A.: Validation of the developed open source library for far-field noise prediction. Proceedings of the 27th International Congress on Sound and Vibration (2021). 27th International Congress on Sound and Vibration (ICSV),
URL: https://doi.org/10.5281/zenodo.5906668 (accessed 07/2023)

[48] Afari S. O.: Prediction of Noise Associated with an Isolated UAV Propeller. Dissertations and Theses (2019). Embry-Riddle Aeronautical University, Issue 463, URL: https://commons.erau.edu/edt/463 (accessed 07/2023)

[49] Courant number in CFD simulations, URL: https://www.idealsimulations.com/resources/courant-number-cfd/ (accessed 07/2023)

[50] De Rosa Jacinto M.: Aerodynamic Effect of a Wingtip - Mounted Propeller. Diploma Thesis (2021). University of Sao Paulo

[51] Brandt J.B., Deters R.W., Ananda G.K., Dantsker O.D., Selig M.S.: UIUC Propeller Database. University of Illinois at Urbana-Champaign, Department of Aerospace Engineering (2022). Vol. 1 - 4, URL: https://m-selig.ae.illinois.edu/props/propDB.html (accessed 07/2023)

[52] Geometry and performance data of APC propellers, URL: https://www.apcprop.com/technical-information/performance-data/ (accessed 07/2023)

[53] Y plus wall distance estimation, URL: https://www.cfd-online.com/Wiki/Y_plus_wall_distance_estimation (accessed 07/2023)

[54] Jiang H., Wu H., Chen W., Zhou P., Zhong S., Zhang X., Zhou G., Chen B.: Toward high-efficiency low-noise propellers: A numerical and experimental study. Physics of Fluids, AIP Publishing (2022). Volume 34, Issue 076116, URL: https://doi.org/10.1063/5.0098891 (accessed 07/2023)

[55] Burgers P.: A thrust equation treats propellers and rotors as aerodynamic cycles and calculates their thrust without resorting to the blade element method. International Journal of Aviation, Aeronautics, and Aerospace (2019). Volume 6, Issue 5, URL: https://doi.org/10.15394/ijaaa.2019.1427 (accessed 07/2023)

[56] Brocklehurst A., Barakos G. N.: A review of helicopter rotor blade tip shapes. Progress in Aerospace Sciences (2013). Volume 56, p. 35-74, URL: https://doi.org/10.1016/j.paerosci.2012.06.003 (accessed 07/2023)

[57] Barry F. W., Magliozzi B.: Noise Detectability Prediction Method for Low Tip Speed Propellers. National Technical Information Service (1971). Technical report AFAPL-TR-71-37, URL: https://apps.dtic.mil/sti/citations/AD0729432 (accessed 07/2023)

12. List of figures

Figure 1.1: Joby Aviation S4 prototype [3] (top) and visualisation of the City Airbus NextGen concept [4] (bottom) 2
Figure 1.2: Phoenix wings ORCA cargo drone (left) [5] and Jetson One eVTOL (right) [6] 3
Figure 2.1: Definition of near and far field with corresponding wave propagation [8]..... 5
Figure 2.2: Correction of SPL values due to ratings (A, B, C and D) [10] (modified) 6
Figure 2.3: Schematic representation of the basic principle of the FFT [13]..... 8
Figure 2.4: Acoustic sources and propagation: monopole (left), dipole (middle) and quadrupole (right) [16]..... 9
Figure 2.5: Propeller noise sources categorised according to the source type [25].....12
Figure 2.6: Schematic representation of harmonic noise (a), broadband noise (b) and narrow band random noise (c) amplitudes displayed over time (left) and the corresponding frequency spectrum(right) (BN = BPF) [25] 13
Figure 3.1: Propeller efficiency as a function of the advance ratio J and pitch angle β [32]...16
Figure 3.2: Pitch angle β at two different propeller blade cross sections [33].....17
Figure 3.3: SPL output for several propellers with different pitch values P_b [35].....18
Figure 3.4: NACA 4412 airfoil with indicated parameters (not scaled correctly) [37] 19
Figure 3.5: Definition of blade sweep angle Λ and mid-chord alignment as a function of the radius r [36] 19
Figure 3.6: Schematic comparison of directivity noise of straight and swept propeller blades [40] (modified) 20
Figure 3.7: Different trailing edge serration shapes and arrangements [41].....21
Figure 3.8: Propeller geometry with detailed view of serrated trailing edge [35].....22
Figure 3.9: Propeller blade tip modifications: 60° dihedral winglet (a), Ogee tip (b), Oval tip (c), TE notch (d) and vortex generators (e) (a-c [12], d-e [44]).....23
Figure 3.10: Propeller leading edge tubercles at different radial positions (left) and the tubercle control parameters: wavelength λ, amplitude A and local chord length c (right) [45] 24
Figure 4.1: Directory and file structure of a OpenFOAM case (directories in dark grey, files in bright grey).....25
Figure 4.2: Geometric measurements of the FWH analogy control surface (light blue) and the rotating cylinder (red) in relation to the radius R of the propeller.....30
Figure 5.1: Airfoil sections along the propeller geometry modelled in CATIA V5.....32
Figure 5.2: Schematic representation of the simulation setup in OpenFOAM: cylinder with cut out propeller geometry (red), simulation domain (grey) and additional cylinder for refinement (dark blue).....33

Figure 5.3: Visualisation of the mesh density in different sections of the simulation setup 34
Figure 5.4: Mesh at the boundary zones between the rotating cylinder in red and the stationary region in blue(left), the first mesh layers on the propeller surface according to the y^+ value (right).....34
Figure 5.5: Mesh quality on the propeller surface created by using the “snappyHexMesh” tool 35
Figure 6.1: Pitch angle and chord length at multiple radial positions for validation case 1 [54].....37
Figure 6.2: Top view (left) and front view (right) of recreated validation case 1 propeller geometry 38
Figure 6.3: Schematic representation of observer positions for validation case 1 [54] 38
Figure 6.4: SPL results of the reference computational and experimental simulations as well as the OpenFOAM simulation plotted over the frequency for an observer at θ = 90° 39
Figure 6.5: SPL plotted over frequency for observers at θ = 56° (top left), θ = 75° (top right), θ = 105° (bottom left) and θ = 118° (bottom right).....40
Figure 6.6: Pitch angle and chord length at multiple radial positions for validation case 2 [35].....41
Figure 6.7: Top view (left) and front view (right) of validation case 2 propeller geometry: normal TE (top) and serrated TE (bottom).....42
Figure 6.8: Schematic representation of observer positions for validation case 2 [35] 42
Figure 6.9: Generated thrust of the different propellers of validation case 2 plotted over time 43
Figure 6.10: SPL plotted over frequency for an observer at θ = 90°: reference normal TE and reference serrated TE simulation (top) and OpenFOAM normal TE and OpenFOAM serrated TE simulations (bottom) [35].....44
Figure 6.11: SPL directivity pattern for the first four blade passing frequencies, shown for normal and serrated trailing edges of reference experiments and OpenFOAM simulations [35].....45
Figure 6.12: Pitch angle and chord length at multiple radial positions for validation case 3 [12].....46
Figure 6.13: Unmodified propeller blade tip (left) and tapered blade tip (right) of validation case 3: first line shows geometry from [12], second line represents recreation in CATIA V5.....47
Figure 6.14: Schematic representation of the observer positions for validation case 3. 47
Figure 6.15: SPL plotted over frequency for observer at θ = 90° (left) and θ = 180° (right) for OpenFOAM simulation and reference experiment as well as simulation.....48

Figure 6.16: SPL plotted over frequency for an observer at θ = 90° (left) and θ = 180° (right) for OpenFOAM simulations (blue) and reference simulations (black) showing normal and tapered tip results at third octave band frequencies 48
Figure 7.1: APC 27x13E in reality (left) and reengineered propeller in CATIA [52] (modified) 50
Figure 7.2: Pitch angle and chord length at multiple radial positions of the reference propeller APC 27x13E [52] 51
Figure 7.3: Propeller efficiency η_p plotted against the advance ratio for several rotational velocities [52] 51
Figure 7.4: Thrust (blue) and mechanical power (green) plotted against advance ratio for a rotational velocity of 5000 RPM [52] 52
Figure 7.5: Generated thrust by the propeller of the reference case for different mesh sizes 54
Figure 7.6: Mechanical power required by the propeller of the reference case for different mesh sizes 55
Figure 7.7: Velocity distribution (in m/s) of the propeller and its wake region at 0,15 s for a freestream velocity of 5,75 m/s at 5000 RPM 55
Figure 7.8: Mach number distribution on the surface of the reference propeller 56
Figure 7.9: Thrust coefficients plotted at several radial positions of the propeller blade 56
Figure 7.10: Filtered vorticity distribution (in 1/s) of the propeller and its wake region at 0,15 s for a freestream velocity of 5,75 m/s at 5000 RPM 57
Figure 7.11: Observer positions (black dots) for the advanced simulations in the xz (blue) and yz plane (red) 58
Figure 7.12: SPL plotted over frequency for an observer at θ = 90° for the reference propeller with additional 1/12 octave band SPL output starting at 1000 Hz 59
Figure 7.13: Directivity plots of the yz plane (left) and the xz plane (right) for the first three BPFs of the reference propeller as well as the OASPL values at all defined observer positions 60
Figure 7.14: Case 1 with leading edge tubercles created in CATIA V5 61
Figure 7.15: Comparison of the generated thrust by the propeller of the reference case and the one with tubercles 62
Figure 7.16: Kinematic pressure distribution (in m^2/s^2) on the upper surface of the reference propeller (left) and the propeller with applied tubercles (right) 62
Figure 7.17: SPL plotted over frequency for an observer at θ = 90° for the reference propeller and the propeller with leading edge tubercles with additional 1/12 octave band SPL output starting at 1000 Hz 63

Figure 7.18: Directivity plots of the yz plane (left) and the xz plane (right) for the first three BPFs as well as the OASPL values at all defined observer positions of the reference propeller (dashed lines) and the one with applied tubercles 64
Figure 7.19: Case 2 with trailing edge sawtooth serrations created in CATIA V5 65
Figure 7.20: Comparison of the generated thrust by the propeller of the reference case and by the propeller with trailing edge serration at a rotational velocity of 4820 RPM (orange line) and 5000 RPM (red line) 65
Figure 7.21: Velocity distribution (in m/s) at the minimum (right side) and maximum (left side) amplitude value of the serration 66
Figure 7.22: SPL plotted over frequency for observer at θ = 90° for the reference propeller and the propeller with trailing edge serration at a rotational velocity of 4820 RPM and 5000 RPM 67
Figure 7.23: Directivity plots of the yz plane at 4820 RPM (left) and at 5000 RPM (right) for the first three BPFs and the OASPL of the propeller with a serrated trailing edge in comparison to the reference propeller at 5000 RPM (dashed lines) 67
Figure 7.24: Blade tip sweep angle ΛTip and anhedral angle ΓTip geometry specification ..68
Figure 7.25: Case 3 with blade tip modifications created in CATIA V5: small tip (left), large tip (middle) and small tip with trailing edge notch (right) 69
Figure 7.26: Comparison of the generated thrust by the propeller of the reference case and the propellers with different tip modifications 69
Figure 7.27: Velocity streamlines (in m/s) indicating tip vortices at the small tip (left) and the tip with the notch (right) 70
Figure 7.28: Comparison of the SPL results for the propeller with the small tip modification and the one with the large tip modification plotted over the frequency for an observer at θ = 90° in relation to the reference propeller 70
Figure 7.29: Comparison of the SPL results for the propeller with the small tip modification and the one with the notch plotted over the frequency for an observer at θ = 90° in relation to the reference propeller 71
Figure 7.30: Directivity plots of the yz plane for the propeller with the small tip (left) and the same one with applied notch (right) for the first three BPFs and the OASPL in comparison to the reference propeller (dashed lines) 72
Figure 7.31: Combination of all geometrical modifications created in CATIA V5 72
Figure 7.32: Generated mesh at the outer blade section with increased density sections 73
Figure 7.33: Comparison of the generated thrust by the propeller of the reference case and the one with all modifications combined at a rotational velocity of 5000 RPM 73

Figure 7.34: Mechanical power required by the propeller with all modifications in comparison to the propeller of the reference case at a rotational velocity of 5000 RPM.....74
Figure 7.35 Velocity distribution (in m/s) of the propeller with all modifications combined at 0,15 s (left) and a detailed view of the tip region (right) 74
Figure 7.36: Comparison of the SPL results for the propeller with the combined modifications plotted over the frequency for an observer at θ = 90° in relation to the reference propeller at a rotational velocity of 5000 RPM 75
Figure 7.37: Directivity plots of the yz plane (left) and the xz plane (right) for the first three BPFs and the OASPL of the propeller with all modifications combined in comparison to the reference propeller (dashed lines) 76
Figure 8.1: Comparison of the generated thrust by the propeller of the reference case and the one with all modifications combined for the hovering flight mode at a rotational velocity of 5000 RPM 77
Figure 8.2: Mechanical power required by the propeller with all modifications in comparison to the propeller of the reference case for the hovering flight mode at a rotational velocity of 5000 RPM 78
Figure 8.3: Comparison of the SPL results for the propeller with the combined modifications plotted over the frequency for an observer at θ = 90° in relation to the reference propeller at a rotational velocity of 5000 RPM for the hovering flight mode 79
Figure 8.4: Directivity plots of the yz plane (left) and the xz plane (right) for the first three BPFs and the OASPL of the propeller with all modifications combined in comparison to the reference propeller (dashed lines) for the hovering flight mode at rotational velocity 5000 RPM 80
Figure 8.5: Comparison of the generated thrust by the propeller of the reference case and the one with all modifications combined for the descend flight mode at a rotational velocity of 5000 RPM 80
Figure 8.6: Mechanical power required by the propeller with all modifications in comparison to the propeller of the reference case for the descent flight mode at 5000 RPM 81
Figure 8.7: Comparison of the SPL results for the propeller with the combined modifications plotted over the frequency for an observer at θ = 90° in relation to the reference propeller at a rotational velocity of 5000 RPM for descent flight mode 82
Figure 8.8: Directivity plots of the yz plane (left) and the xz plane (right) for the first three BPFs and the OASPL of the propeller with all modifications combined in comparison to the reference propeller (dashed lines) for the descent flight mode at a rotational velocity of 5000 RPM.....83
Figure 9.1: Comparison of the generated thrust by the propeller of the reference case and the one with all modifications combined at a rotational velocity of 3000 RPM.....85

Figure 9.2: Mechanical power required by the propeller with all modifications in comparison to the propeller of the reference case at a rotational velocity of 4000 RPM 85
Figure 9.3: Comparison of the SPL results for the propeller with the combined modifications plotted over the frequency for an observer at θ = 90° in relation to the reference propeller at a rotational velocity of 6000 RPM 86
Figure 9.4: Directivity plots of the yz plane (left) and the xz plane (right) for the first three BPFs and the OASPL of the propeller with all modifications combined at a rotational velocity of 7000 RPM in comparison to the reference propeller.....87
Figure 9.5: Comparison of the OASPL output at θ = 90° for the climb, hover and descent case at several rotational velocities for the reference geometry and the modified one 88
Figure 9.6: Comparison of the generated thrust (green) and the required mechanical power (blue) for the climb case at several rotational velocities for the reference geometry (dashed line, square data points) and the combination case (solid line, triangle data points) 89
Figure A.1: Comparison of the generated thrust by the propeller of the reference case and the one with all modifications combined at a rotational velocity of 4000 RPM.....105
Figure A.2: Comparison of the generated thrust by the propeller of the reference case and the one with all modifications combined at a rotational velocity of 6000 RPM.....105
Figure A.3: Comparison of the generated thrust by the propeller of the reference case and the one with all modifications combined at a rotational velocity of 7000 RPM.....106
Figure A.4: Mechanical power required by the propeller with all modifications in comparison to the propeller of the reference case at a rotational velocity of 3000 RPM 106
Figure A.5: Mechanical power required by the propeller with all modifications in comparison to the propeller of the reference case at a rotational velocity of 6000 RPM 107
Figure A.6: Mechanical power required by the propeller with all modifications in comparison to the propeller of the reference case at a rotational velocity of 7000 RPM 107
Figure A.7: Comparison of the SPL results for the propeller with the combined modifications plotted over the frequency for an observer at θ = 90° in relation to the reference propeller at a rotational velocity of 3000 RPM 108
Figure A.8: Comparison of the SPL results for the propeller with the combined modifications plotted over the frequency for an observer at θ = 90° in relation to the reference propeller at a rotational velocity of 4000 RPM 108
Figure A.9: Comparison of the SPL results for the propeller with the combined modifications plotted over the frequency for an observer at θ = 90° in relation to the reference propeller at a rotational velocity of 7000 RPM 109

Figure A.10: Directivity plots of the yz plane (left) and the xz plane (right) for the first three BPFs and the OASPL of the propeller with all modifications combined at a rotational velocity of 3000 RPM in comparison to the reference propeller 109
Figure A.11: Directivity plots of the yz plane (left) and the xz plane (right) for the first three BPFs and the OASPL of the propeller with all modifications combined at a rotational velocity of 4000 RPM in comparison to the reference propeller 110
Figure A.12: Directivity plots of the yz plane (left) and the xz plane (right) for the first three BPFs and the OASPL of the propeller with all modifications combined at a rotational velocity of 6000 RPM in comparison to the reference propeller 110

13. List of tables

Table 1: Octave band and corresponding third octave band centre frequency values in the audible range [11] 7
Table 2: Position and unit of each SI base value which is specified in OpenFOAM [31] 26
Table 3: Initial input parameters for the propeller geometry creation using a Python script ...31
Table 4: Overview of some geometry and simulation characteristics of the validation cases 36
Table 5: Overview of the characteristics of validation case 1 37
Table 6: Overview of characteristics of validation case 2 41
Table 7: Overview of the characteristics of validation case 3 46
Table 8: Overview of the characteristics of the APC 27x13E propeller 50
Table 9: Overview of the characteristics of each mesh category in the mesh quality study ...53
Table 10: Overview of the individual geometrical modifications and the radial application range 60
Table 11: Overview of the number of cells and the step size of the individual geometrical..... modification simulation cases 61
Table 12: Overview of the mechanical power differences and tip Mach number values of the defined tip modifications in comparison to the reference blade tip 70
Table 13: Summary of the time averaged generated thrust, time averaged required mechanical power and OASPL results in relation to the unmodified reference propeller at a rotational velocity of 5000 RPM 76
Table 14: Summary of important data of the reference propeller cases at multiple rotational velocities [52] 84

Appendix A

In this appendix, the additional diagrams of the parameter study of chapter 9 are presented. For the four rotational velocities considered, three are displayed here in the appendix for each parameter, in each case the rotational speeds that did not occur in chapter 9.

Thrust:

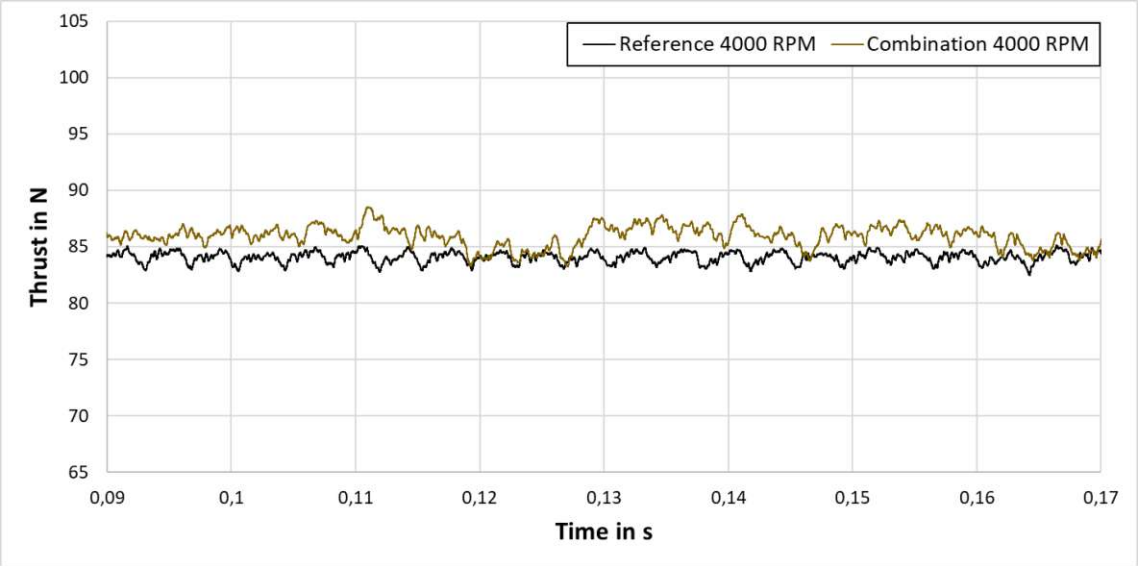

Figure A.1: Comparison of the generated thrust by the propeller of the reference case and the one with all modifications combined at a rotational velocity of 4000 RPM

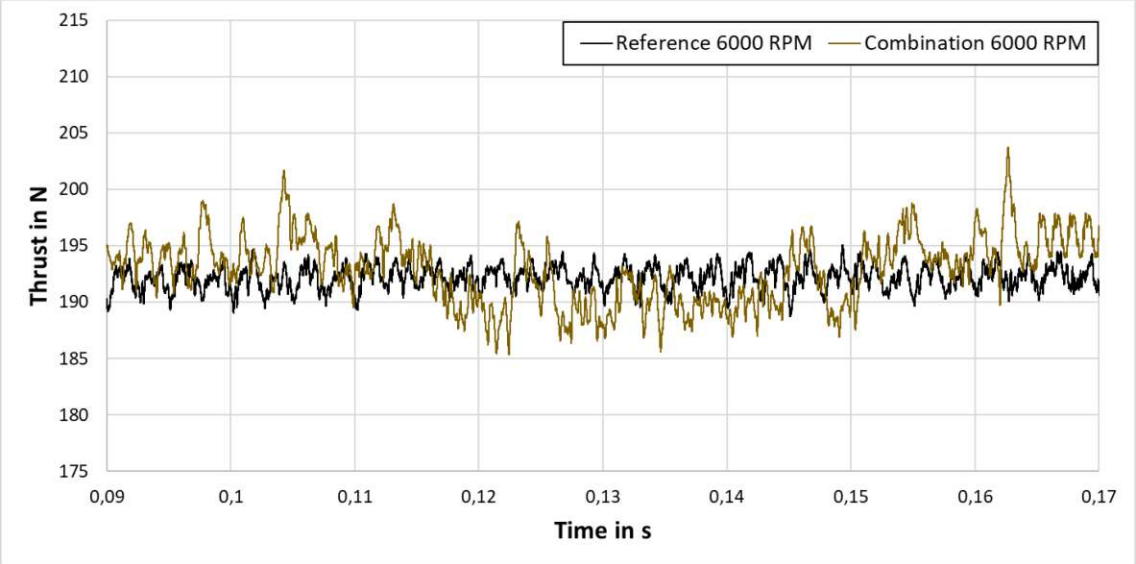

Figure A.2: Comparison of the generated thrust by the propeller of the reference case and the one with all modifications combined at a rotational velocity of 6000 RPM

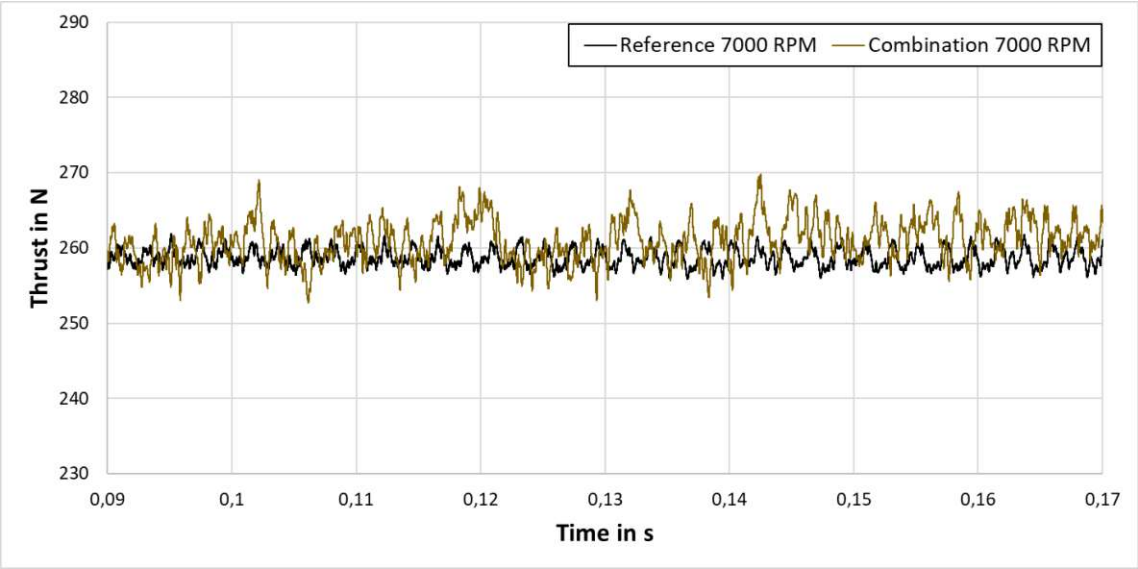

Figure A.3: Comparison of the generated thrust by the propeller of the reference case and the one with all modifications combined at a rotational velocity of 7000 RPM

Mechanical power:

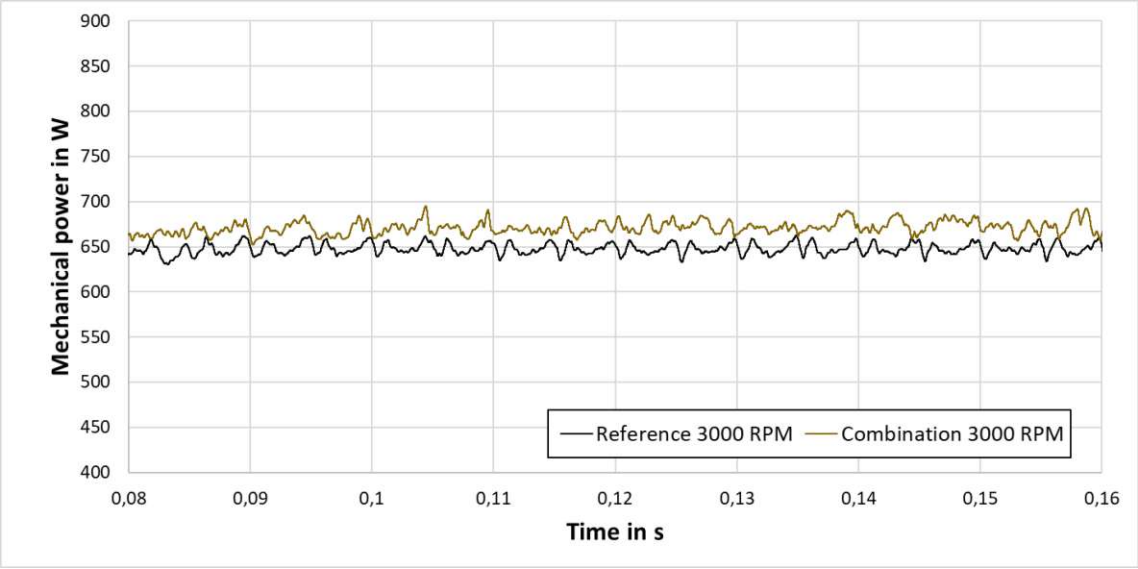

Figure A.4: Mechanical power required by the propeller with all modifications in comparison to the propeller of the reference case at a rotational velocity of 3000 RPM

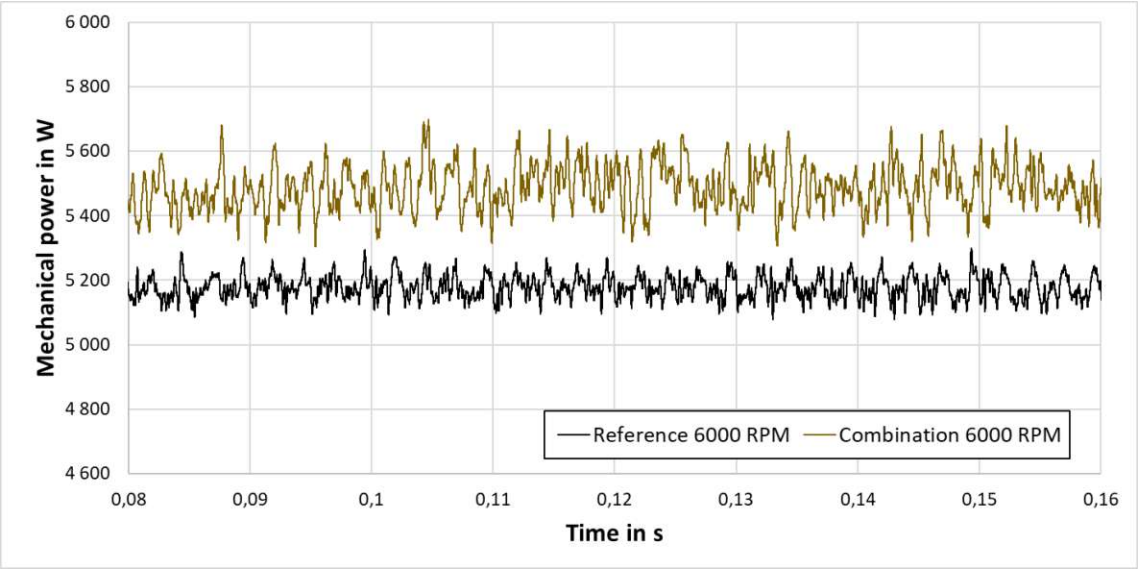

Figure A.5: Mechanical power required by the propeller with all modifications in comparison to the propeller of the reference case at a rotational velocity of 6000 RPM

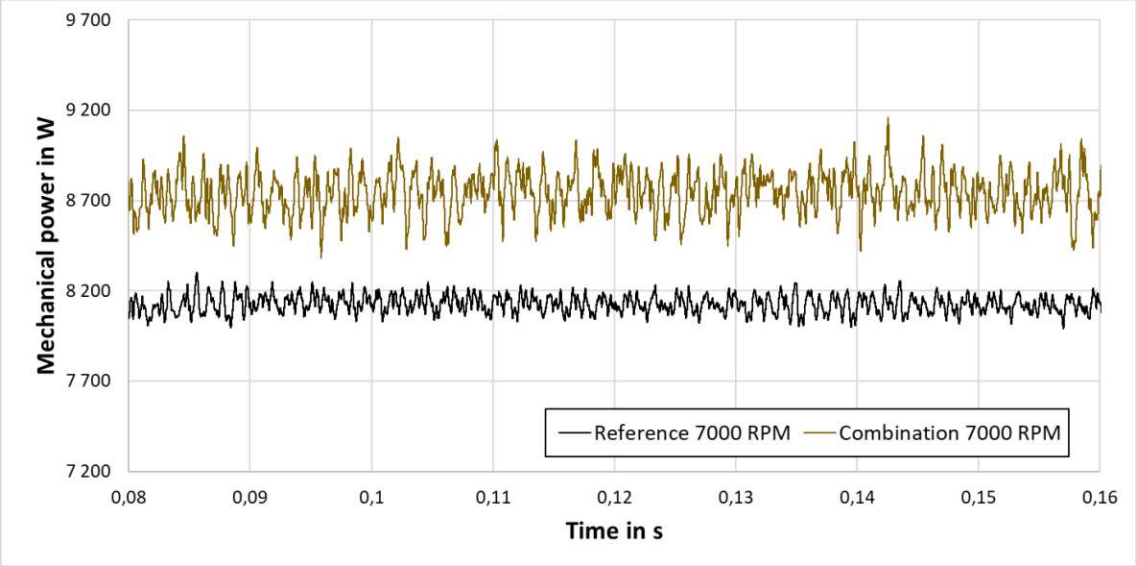

Figure A.6: Mechanical power required by the propeller with all modifications in comparison to the propeller of the reference case at a rotational velocity of 7000 RPM

SPL plotted over frequency:

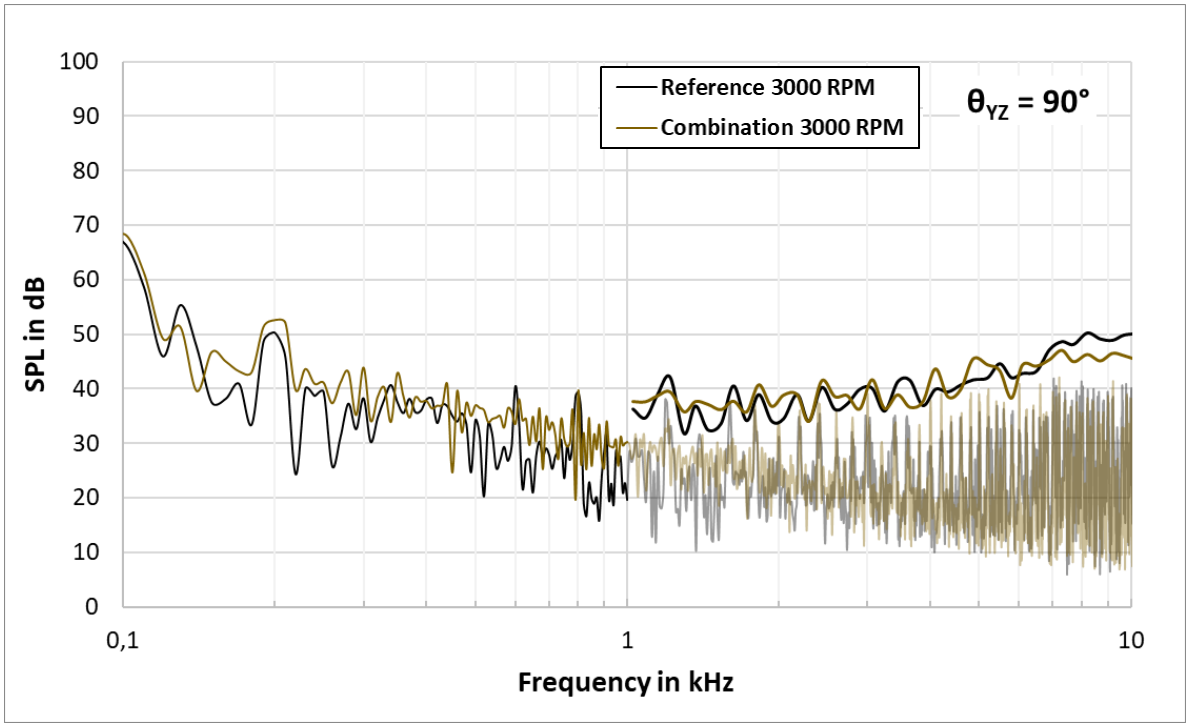

Figure A.7: Comparison of the SPL results for the propeller with the combined modifications plotted over the frequency for an observer at θ = 90° in relation to the reference propeller at a rotational velocity of 3000 RPM

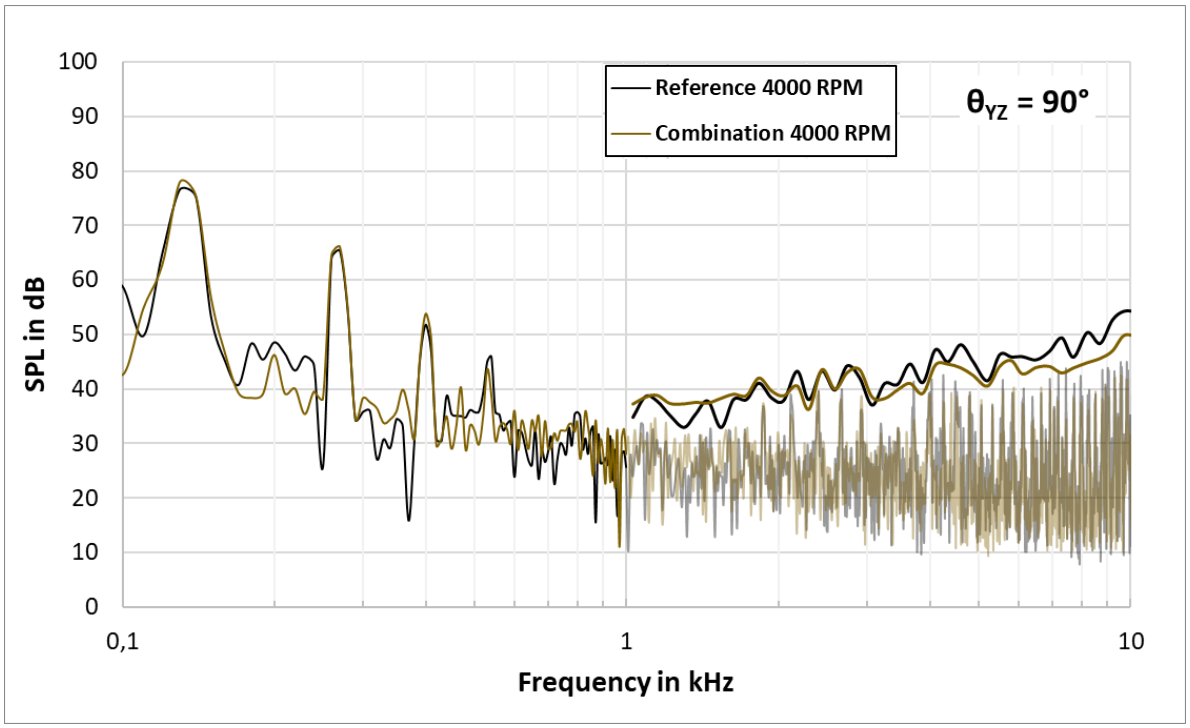

Figure A.8: Comparison of the SPL results for the propeller with the combined modifications plotted over the frequency for an observer at θ = 90° in relation to the reference propeller at a rotational velocity of 4000 RPM

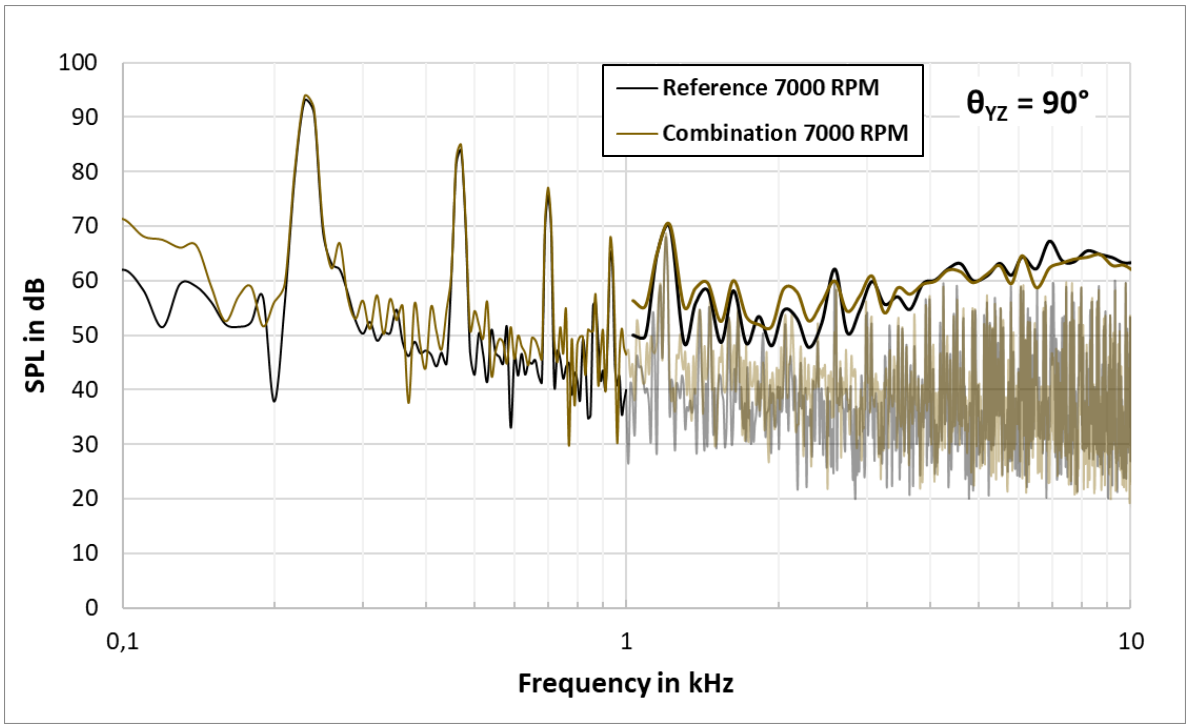

Figure A.9: Comparison of the SPL results for the propeller with the combined modifications plotted over the frequency for an observer at θ = 90° in relation to the reference propeller at a rotational velocity of 7000 RPM

Directivity plots:

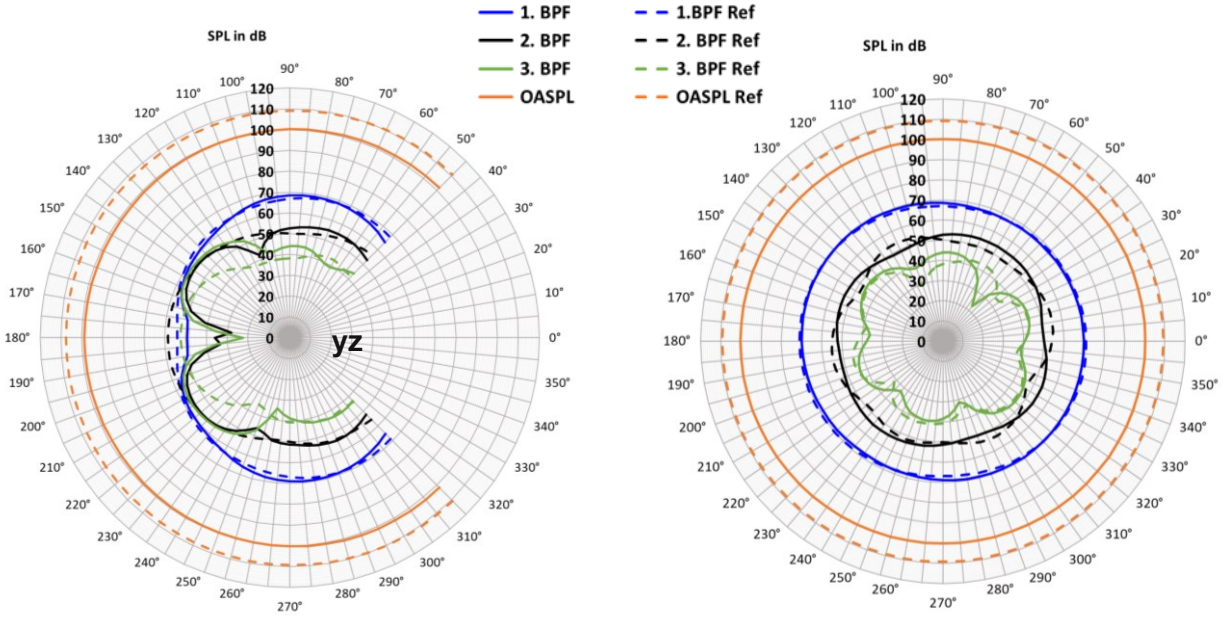

Figure A.10: Directivity plots of the yz plane (left) and the xz plane (right) for the first three BPFs and the OASPL of the propeller with all modifications combined at a rotational velocity of 3000 RPM in comparison to the reference propeller

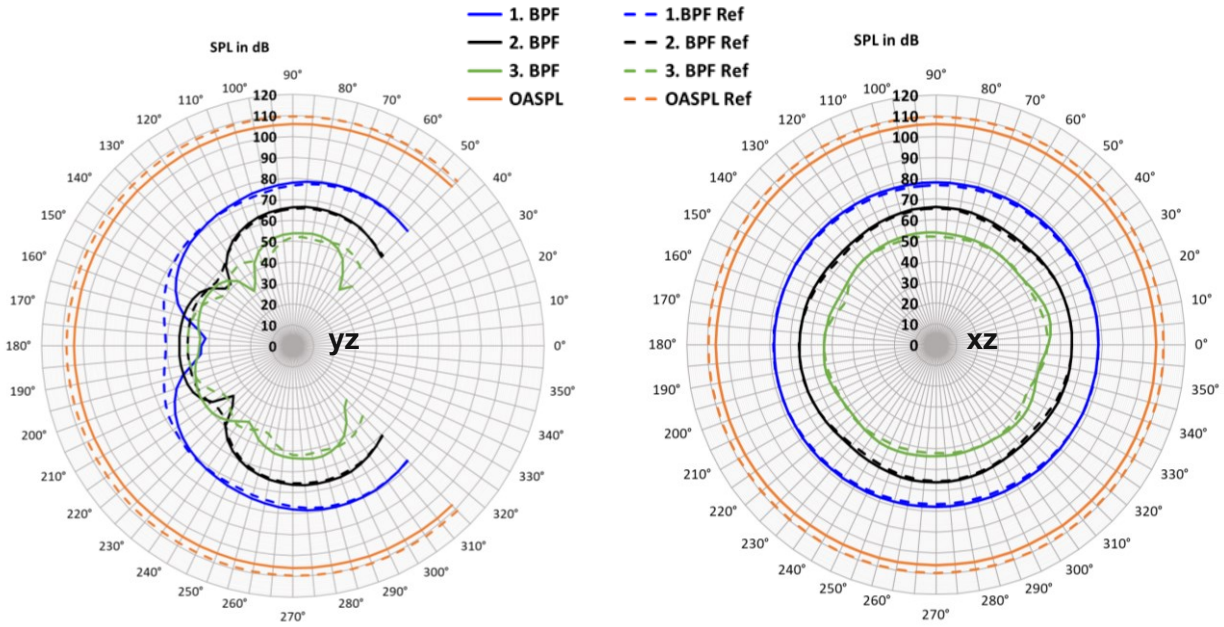

Figure A.11: Directivity plots of the yz plane (left) and the xz plane (right) for the first three BPFs and the OASPL of the propeller with all modifications combined at a rotational velocity of 4000 RPM in comparison to the reference propeller

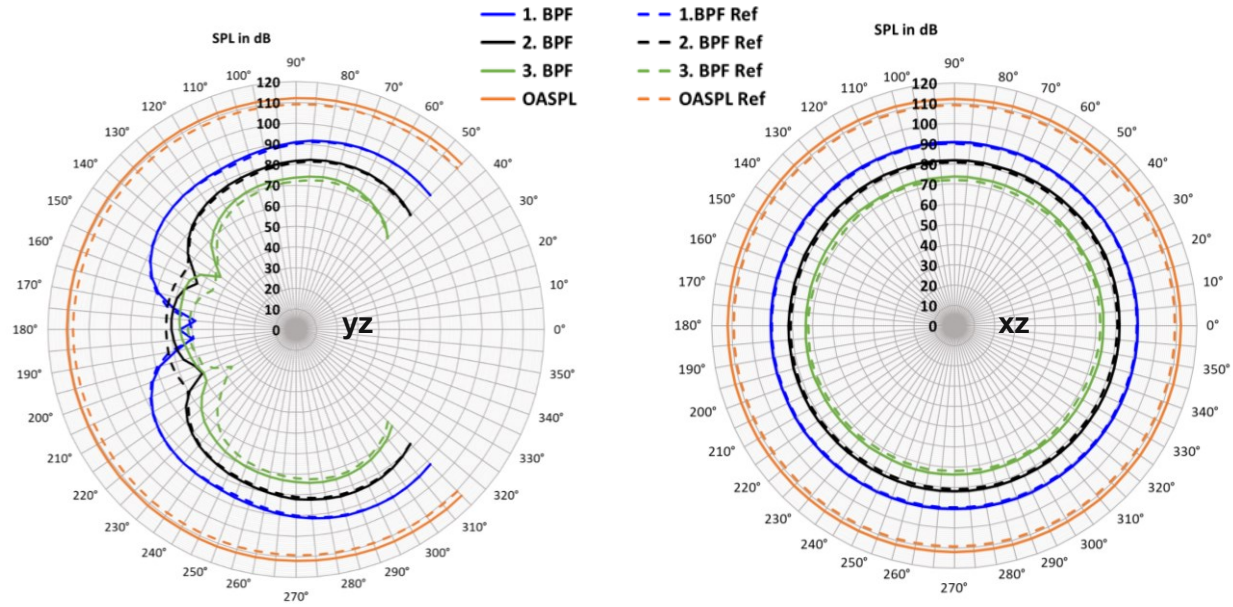

Figure A.12: Directivity plots of the yz plane (left) and the xz plane (right) for the first three BPFs and the OASPL of the propeller with all modifications combined at a rotational velocity of 6000 RPM in comparison to the reference propeller